Stony Brook University

A Solid State NMR and EXAFS Study of Manganese Oxide Minerals

A Dissertation Presented

by

Kellie Ann Aldi

to

The Graduate School

in Partial Fulfillment of the

Requirements

for the Degree of

Doctor of Philosophy

in

Chemistry

Stony Brook University

December 2011

Stony Brook University

The Graduate School

Kellie Ann Aldi

We, the dissertation committee for the above candidate for the

Doctor of Philosophy degree, hereby recommend

acceptance of this dissertation.

Clare P. Grey – Dissertation Advisor
Professor, Department of Chemistry, Stony Brook University

Stephen Koch – Chairperson of Defense
Professor, Department of Chemistry, Stony Brook University

Andreas Mayr – Third Member of Defense
Professor, Department of Chemistry

Luis Smith – Outside Member of Defense
Associate Professor, Department of Chemistry, Clark University

This dissertation is accepted by the Graduate School

Lawrence Martin
Dean of the Graduate School

Abstract of the Dissertation

A Solid State NMR and EXAFS study of manganese oxide minerals

by

Kellie Ann Aldi

Doctor of Philosophy

in

Chemistry

Stony Brook University

2011

Though only a minor component of soils occurring as thin coatings on rocks and sediments, manganese oxide minerals are excellent sorbents of various cations and have a significant impact on the geochemical cycling of environmentally relevant cations such as Pb, Cd, Ni, Cu and Zn. The layered manganese oxide, birnessite, has been found to have the highest sorption capacity of these Mn minerals, attributed to the negative layer charge that arises from structural "defects" such as layer Mn^{3+} ions and Mn^{4+} vacancies, as well as the high interlayer surface area available for the sorption of charge compensating cations. Great interest in understanding the nature of cation adsorption in these materials has resulted in numerous cation sorption studies, utilizing techniques to extract information regarding locations and ordering of sorbed cations and quantifying layer Mn vacancies. However, commonly utilized techniques such as EXAFS and X-ray diffraction have high errors associated with the refinement of cation coordination and quantification of layer vacancies, and require correlation of results from other techniques to support these refinements. Application of solid state NMR to these materials has not been extensively explored due to difficulties associated with the paramagnetic manganese ions. This dissertation aims at illustrating the utility of this technique in these paramagnetic materials. NMR is sensitive to the local environment, including the types and oxidation states of coordinated metals, coordination geometry and bonding distances surrounding the observed nucleus. ^{23}Na

NMR is used to determine sodium locations with respect to the ordering of Mn^{3+} and Mn^{4+} in the triclinic form of birnessite and other layered sodium manganese oxides, indicating layer charge distribution drives cation ordering. ^{2}H NMR is used to understand the interactions of crystalline interlayer water with that of layer vacancies in hexagonal birnessite, and to quantify layer vacancies that are charge compensated by deuterons in these materials. Development of a special tailored structural model of Mn K-edge EXAFS data for these hexagonal birnessites support the trends observed in the ^{2}H NMR. The use of solid state NMR in these paramagnetic systems enriches our understanding of the complex interactions between the Mn layers and interlayer species in these important manganese oxide minerals.

Dedication Page

When asked what I wanted to be when I grew up as a 5 year old, just beginning my journey in education, I happily replied, “I want to be a grandma!”

To my Grandma Reisinger, who started me off on my A, B, C’s and 1, 2, 3’s; who knew her encouragement, support and love would take me far.

I’ve since added other life goals, but that first one still has not changed.

Table of Contents

List of Figures

List of Tables

List of Abbreviations

CSA	Chemical Shift Anisotropy
EDS	Energy Dispersive X-ray Spectroscopy
EXAFS	Extended X-ray Absorption Fine Structure
MAS	Magic Angle Spinning
NMR	Nuclear Magnetic Resonance
SAED	Selected Area Electron Diffraction
SEM	Scanning Electron Microscopy
TEM	Transmission Electron Microscopy
TGA	Thermogravimetric Analysis
XAFS	X-ray Absorption Fine Structure
XANES	X-ray Absorption Near Edge Structure
XRD	X-ray Diffraction

Acknowledgments

First and foremost, I would like to thank Professor Clare Grey. She has had the greatest patience and provided guidance throughout my Ph.D. experience that has allowed me the freedom to explore where my own interests would lead my research, and provided countless opportunities to expand as a scientist. Two nations divided by a common language, I've often struggled to properly convey my gratitude. I consider myself lucky to have learned so much from such an amazing woman.

I would like to thank all past and present Grey Group members. The overwhelming kindness and generosity of my fellow labmates, in my experience, is unparalleled anywhere else, both academia and industry. It has been a true pleasure working with them. A special thanks to Dr. Jordi Cabana, Dr. Jongsik Kim and Dr. Paul Sideris. They are all far too kind and modest to make much of a "big deal" of it, but the time, patience and helpful scientific discourse they gave me while teaching me the ropes of solid state NMR became a solid foundation for which I am forever grateful. I would also like to thank Dr. James Marecek. I know he's not a Grey Group member, but he is the unsung hero and savior of every one of our magnets, and his help and careful maintenance of the magnets, so central to this work, did not go unnoticed or unappreciated.

I would like to thank Dr. John Bargar (Stanford Synchrotron Radiation Lightsource in Palo Alto, CA) and Dr. Jasquelin Pena (Berkeley National Laboratory in Berkeley, CA) for sharing their expertise in X-ray Absorption Spectroscopy. Many thanks also to Professor Rich Reeder (Dept. of Geosciences, Stony Brook University) for helpful discussions and advice regarding data processing and EXAFS modeling.

I am indebted to the kindness, patience and support of my friends here at Stony Brook, without whom I would not have ever finished all this. A special thanks to Nicole Trease, Andy Ilott and Laura Kubista who made me laugh, cry and get annoyed or motivated at all the right times. Thanks to Allison Haigney, Andrew Malingowski, Allie Reinert who made me smile whenever I ran into them.

I would like to thank all my family. My parents, grandparents, brothers, sisters, aunts and uncles and cousins, and those who have become my family: Lucienne Buannic and Kanishk Kapilashirami. Special thanks to Maryann Jones and Pauline Breeden, two amazingly strong

women who have given me love and support as their own daughter. I could not have done this without their endless love and support.

And finally, I would like thank my husband, Marco Aldi. I don't really have words to say all the gratitude and love I feel in my heart, but I think he knows already anyway.

Chapter 1

Introduction

I. Motivation

Manganese oxides occur in nature as more than 30 varieties of Mn oxide/hydroxide minerals.[1] These minerals are ubiquitous in the environment in soils and sediments, found as coatings on other mineral particles and rocks, and as significant components of deep sea nodules covering large expanses of the ocean floors.[2] The majority of manganese oxides occurring in nature are produced by microbial and fungal oxidation of soluble Mn^{2+} present in soils and water,[3-6] though some formation of manganese oxides does occur through direct oxidation of Mn^{2+} as well.[7] Many studies have demonstrated the high adsorption capacity of manganese oxides for a variety of cations, notably ions commonly occurring as anthropogenic pollutants (*i.e.* Pb, Zn, Cd, Cu, and Ni).[8-13] Due to the common occurrence of these minerals in nature, as well as the characteristic affinity for cation adsorption, manganese oxides play an important role in the geochemical cycling and thus, bioavailability, of these ions. Manganese oxides are readily synthesized in the laboratory, and comparisons of synthetic manganese oxides, both inorganic and biogenic preparations, with that of naturally occurring forms have shown that the synthetic analogues provide a useful model to study these materials.[14, 15] In addition to the vital role manganese oxides play in the environment as regulators of the geochemical cycling of various cations, there is a growing interest in these compounds in the field of energy storage as battery cathode materials. [16-21] Therefore there is great interest in understanding the structure of these compounds, as well as the nature of cation adsorption in these materials. We first review the important manganese oxide structures investigated in this thesis. Many of these compounds are highly disordered, making them difficult to characterize with any single analytical technique. Following the introduction of the compounds investigated in this thesis, the techniques and the theory behind the experimental approaches will be described.

A. Birnessite

Birnessite is the most common form of naturally occurring layered manganese oxides.[1] While birnessite is essentially a general term for a relative structural continuum of mixed-

valence layered manganese oxides characterized by a 7Å interlayer spacing (and sometimes a 10Å interlayer spacing), there are two readily identifiable structural extremes; these two birnessite phases are referred to as triclinic birnessite and hexagonal acid birnessite.

a. Triclinic Birnessite

Octahedral Layer

Vacancy free manganate layers are associated with the triclinic form of birnessite.[22] During synthesis at high pH, the initial precipitate formed is a metastable intermediate referred to as buserite, which is characterized by a 10Å interlayer spacing. Upon air drying of the buserite phase, the layers typically collapse to an interlayer spacing of about 7Å, which is characteristic of the birnessite phase.[23] A negative layer charge arises from the presence of Mn^{3+} ions, which are thought to be ordered into rows parallel to the *b* axis and separated by two rows rich in Mn^{4+} ions along the *a* axis (Figure 1.1).[24, 25] The coordinated ordering of Mn^{3+} ions within the layers is attributed to minimization of steric strain introduced by Jahn-Teller distortions that have been observed to occur in birnessite and other manganese oxides of mixed valence containing 25-30% Mn^{3+}.[26] The relative amounts of Mn^{3+} and Mn^{4+} in the manganate layers of synthetic birnessite is sensitive to the conditions under which it is formed, both synthetic and natural,[27-30] and is often inferred by the interlayer cation content, particularly when X-ray diffraction Rietveld refinements indicate the occupancy of layer Mn to be close or equal to 1.[29, 31] Kuma *et. al* noted changes in the β (β = 103.18, 96.65, and 100.76°) , *a* (*a* = 5.175, 5.049, and 5.149Å) and *c* (*c* = 7.337, 7.051, and 7.176Å) of cell parameters for Na^{+}, Mg^{2+} and K^{+} exchanged birnessite, respectively, while the *b* cell parameter remained relatively constant.[15] Studies refining the structure of triclinic birnessite via Rietveld refinement of X-ray diffraction and model fitting of EXAFS report differences in Jahn-Teller distorted Mn-O octahedral bonds ranging from 1.88 to 1.945Å for the shortened equatorial Mn-O distances compared to 1.90 to 2.003Å for elongated equatorial Mn-O distances.[25, 29, 32, 33] Changes in the *a* lattice parameter are typically attributed to changes in layer Mn^{3+}/Mn^{4+} ratio, which affects the extent of the azimuthal oriented Jahn-Teller elongation of the Mn^{3+} axial Mn-O bonds along *a*.[10] Investigations of interlayer cation exchange in birnessites show differing cation ordering within the interlayer of exchanged birnessites; following from the logic that cation ordering is driven by offsetting negative layer charge, these

studies indicate that there may be some variation in the relative amounts of layer Mn^{3+} and Mn^{4+} ions, as well as differences in their ordering in the manganate layer upon cation exchange.[34, 35]

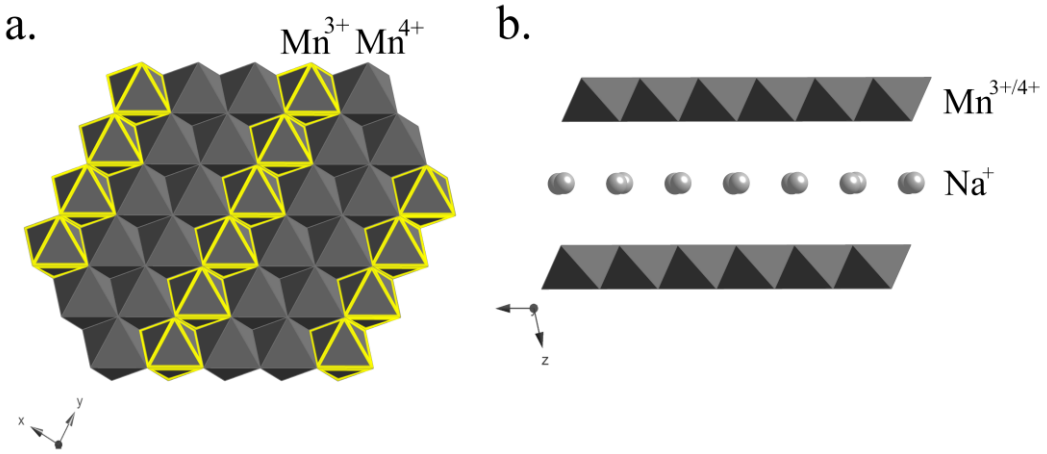

Figure 1.1 The idealized structure of triclinc birnessite. (a) Mn^{3+} ions order into Mn^{3+}-rich rows separated by Mn^{4+}-rich rows along the b axis. (b) The manganese oxide layers stack, sandwiching interlayer water and cations that offset the negative layer charge.

Interlayer Species

Interlayer cations in birnessite are readily exchanged and the impacts on the crystal structure *c* lattice parameter have been studied extensively.[15, 34, 36, 37] The dominant influence of interlayer spacing, the *c* cell parameter, has been attributed to the strength of the water complex between interlayer waters and the charge compensating cation.[15] While all exchanges involving monovalent interlayer cations have been reported to produce the 7Å birnessite phase (Figure 1.1 b),[37] most divalent cation exchanges stabilize the interlayer spacing at ~10Å.[38] The collapse of the manganate layers to an 7Å spacing has been determined to be due only to the loss of interlayer water and not from any structural rearrangement of the manganate layers.[27] Infrared spectroscopy studies of various cation exchanged birnessites by Johnson and Post indicate the presence of two or three different types of interlayer water, also noting that the degree of hydrogen bonding between interlayer water and layer oxygen atoms was similar for all the birnessites investigated.[39]

b. Hexagonal Birnessite

Octahedral Layer

Synthesis of hexagonal birnessite is most often carried out by acidifying a suspension of triclinic sodium birnessite.[24, 40] The conversion of the vacancy-free layers of triclinic birnessite to hexagonal birnessite is believed to be the result of disproportionation of layer Mn^{3+} ions:

$$Mn_{layer}^{3+} + Mn_{layer}^{3+} \rightarrow Mn_{layer}^{4+} + Mn_{aq}^{2+}$$

leaving behind Mn^{4+} in the layer and producing a layer vacancy and aqueous Mn^{2+} (Figure 1.2 a).[40] The disproportionation of layer Mn^{3+} also results in the disappearance of Jahn-Teller distortions characteristic of triclinic birnessite.[24] It has been suggested that the optimal ordering of layer vacancies in hexagonal birnessite is a linear ordering, which follows from the ordering of Mn^{3+} in the triclinic precursor.[15] Hexagonal birnessites are also produced by a variety of microorganisms in which XANES and EXAFS analysis indicate minimal presence of structural Mn^{3+} and notable amounts of Mn^{2+}, presumably offsetting layer charge in a predominately hexagonal layer birnessite.[6, 41]

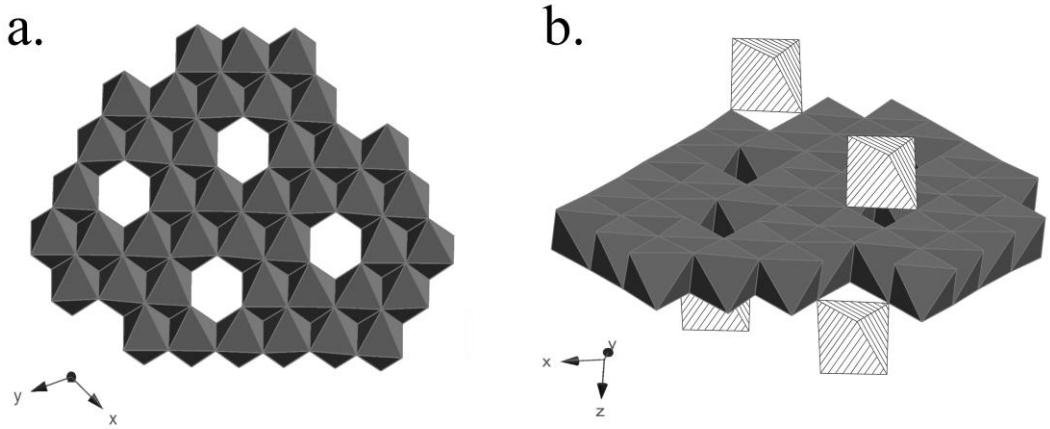

Figure 1.2 The idealized structure of hexagonal acid birnessite. (a) Layer vacancies give rise to the negative layer charge. (b) The layer charge is offset by protons and interlayer cations. A single layer is depicted to show the coordination of cations (striped octahedra) over the vacancies present in the layer.

Interlayer Species

Lanson *et. al* indicated that hydrogen bonding between interlayer waters and layer oxygen plays a crucial role in layer registry of layer stacking in the transformation of sodium buserite to hexagonal birnessite.[24] Webb et al. have found the cation species present in solution during formation of biogenic birnessite phases by the Marine *Bacillus Sp*. strain SG-1 bacteria influences the layer structure; Ca^{2+} ions were found to influence the production of a triclinic phase of birnessite, while Na^{+} ions resulted in the production of a birnessite phase with hexagonal layer symmetry.[33] Interlayer cations have been determined to complex over vacancies to offset the negative layer charge,[12, 25, 42] and in some cases, such as Cu, incorporate into the layer structure at vacancy sites.[13]

B. Tunnel Structure Manganese Oxides

There are a number of naturally occurring tunnel structured manganese oxides as well. Syntheses of these materials usually require a buserite/birnessite precursor material, whereby a template cation is exchanged into the interlayers, followed by a synthetic step in which the layers collapse into different sized tunnels determined by the template cation.

a. Todorokite

Todorokite is a naturally occurring tunnel structured manganese oxide, composed of triple chains of MnO_6 octahedra.[1] Post and Bish performed Rietveld refinement of todorokite, providing significant insight into the tunnel structure and ordering of tunnel waters and cations, postulating that most todorokite likely forms through the transformation of the layer manganese in the birnessite phase.[43] The ordering of the mixed valence manganese in the tunnel structure could not be definitively assigned, but the refined Mn-O distances of octahedra forming the corners of the tunnels were elongated compared to the refined Mn-O distances of the center octahedra, indicating that lower valence Mn are preferentially located at these corner sites.

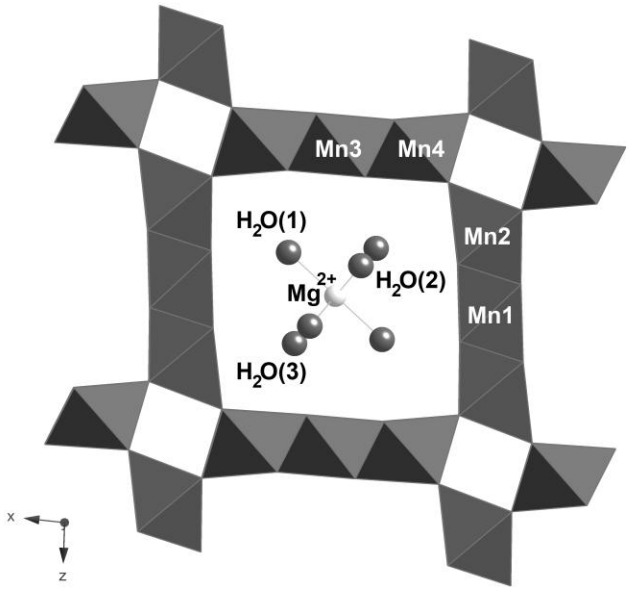

Figure 1.3 Todorokite structure shown with Mg^{2+} tunnel cations. There is considerable disorder over the water and cation sites, the H_2O (1) site is preferred by waters and is approximately fully occupied. The $H_2O(2)$ site is often displaced by larger cations when mixed counter ions are present. The $H_2O(3)$ site is partially occupied, as well as a partial occupancy at the tunnel center site (labeled Mg^{2+}) in the structure illustrated. Mn2 and Mn4 are preferentially occupied by lower valence Mn, and Mn1 and Mn3 are preferentially occupied by Mn^{4+} ions. Structure taken from Post et al (2003).[44]

Their analysis of the tunnel species positions was hindered in the structural refinement by Post and Bish due to considerable disorder present in the natural samples used in their study.[43] With an approximated 4 water molecules per unit cell, the crystalline waters in the tunnels of todorokite are believed to occupy well defined crystallographic sites, with some component of this water positionally disordered over a number of other sites depending on the composition of cations present as well. For example, cations such as Ca and Na may sit at the octahedral site at the center of the tunnel or at different water sites, depending on the number of surrounding water molecules within the tunnel. However, based on smaller than expected difference-Fourier mapped peaks for some water positions within the tunnels suggests that the larger cations, K and Ba, may move off center towards the tunnel walls due to their larger ionic radius. Calculations refining the positions of tunnel waters indicate they are displaced slightly from tunnel walls, resulting in elongated H_2O-O distances. An IR spectroscopy study by Potter and Rossman reported varying amounts of hydrogen bonding in todorokite, presumably from waters, with

stronger hydrogen bonding in more ordered samples and less hydrogen bonding in disordered todorokite.[27]

b. Cryptomelane

The general term, hollandite group, is used to describe a tunnel structure manganese oxide composed of double chains of edge sharing manganese octahedra that corner share with other double chains. The term cryptomelane specifies that the major tunnel cation present in this 2x2 tunnel structure is K^+. Post et al. suggest the presence of a distortion of the tunnel structure which is believed to originate from the twisting of tunnel Mn octahedra.[45] This distortion is linked to the presence of smaller tunnel cations (such as Na^+ with a non-ideal ionic radii, as compared to K^+ in the cryptomelane structure) in which the twisting aids in the adjustment of the tunnel volume to allow for contacts to be formed between tunnel oxygen and the smaller ionic radius of the cation present. (Figure 1.3).

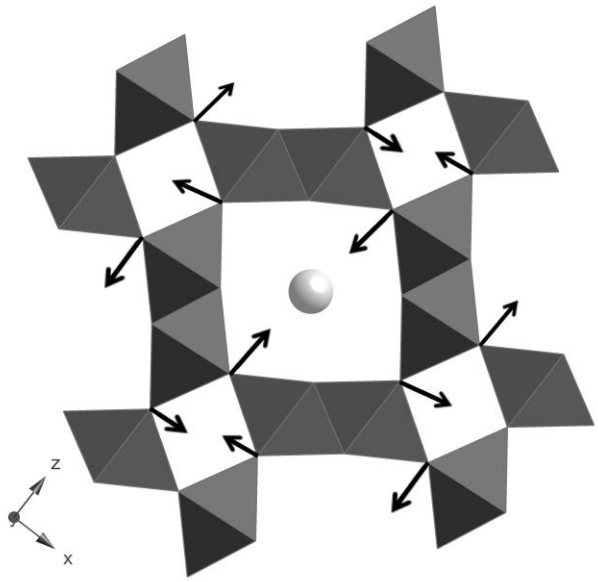

Figure 1.4 The idealized structure of cryptomelane. The K^+ ion has an ideal ionic radius to sit in the tunnel center and satisfy ionic contact distances. The arrows show the general distortion of the tunnel volume that occurs to accommodate smaller cations.

The IR study by Potter and Rossman included a number of hollandites containing either K, Pb, or Na as the major cation species present in the tunnel structures, but found no notable difference between the samples.[27] A low intensity water bending band was observed at 1600 cm^{-1}

indicating the presence of some minor amounts of water molecules that are unlikely to occupy a well defined crystallographic site. The refinements of Post *et al.* indicate the presence of some water and estimate it to be about 0.5 water molecules per unit cell.[45]

I. Analytical Techniques

The work presented in this thesis utilizes a variety of techniques for characterization and interpretation of the compounds investigated. These techniques are introduced, and important aspects of each are discussed.

A. Solid State Nuclear Magnetic Resonance Spectroscopy (NMR)

Solid state NMR is a useful technique for obtaining information regarding the local structure of an observed nucleus due to its sensitivity to such structural features as bonding distances and angles, oxidation states of surrounding coordinated atoms, and motional dynamics. However, the proper NMR techniques (*i.e.* magnetic field strength, pulse sequences, and experimental temperature) must be determined and optimized for the particular system under investigation. For the systems described in this work, interactions such as dipolar coupling, quadrupolar coupling and the Fermi-contact interaction must be considered. Here, the basic interactions and experimental considerations for the study of these materials will be introduced.

a. Chemical Shielding

When an NMR active nucleus in an external magnetic field, B_o, is irradiated by an appropriately tuned radio frequency pulse, the manipulated net magnetization precesses at the Larmor frequency, ω_o, around the external field (taken to be the *z*-axis). While the standard Larmor frequency of any nucleus can be obtained from many reference books on NMR or papers in the literature, the actual precession frequency of the nuclear spin is altered by the chemical shielding produced by the local environment of the observed nucleus. The external magnetic field induces a secondary field due to the electronic density of the atoms surrounding the observed nucleus. However, since the electron distribution about the observed nucleus is typically non-spherical, the induced local magnetic field is orientation dependent, which is an important consideration in a powder sample composed of many crystals with all different orientations (Figure 1.5)

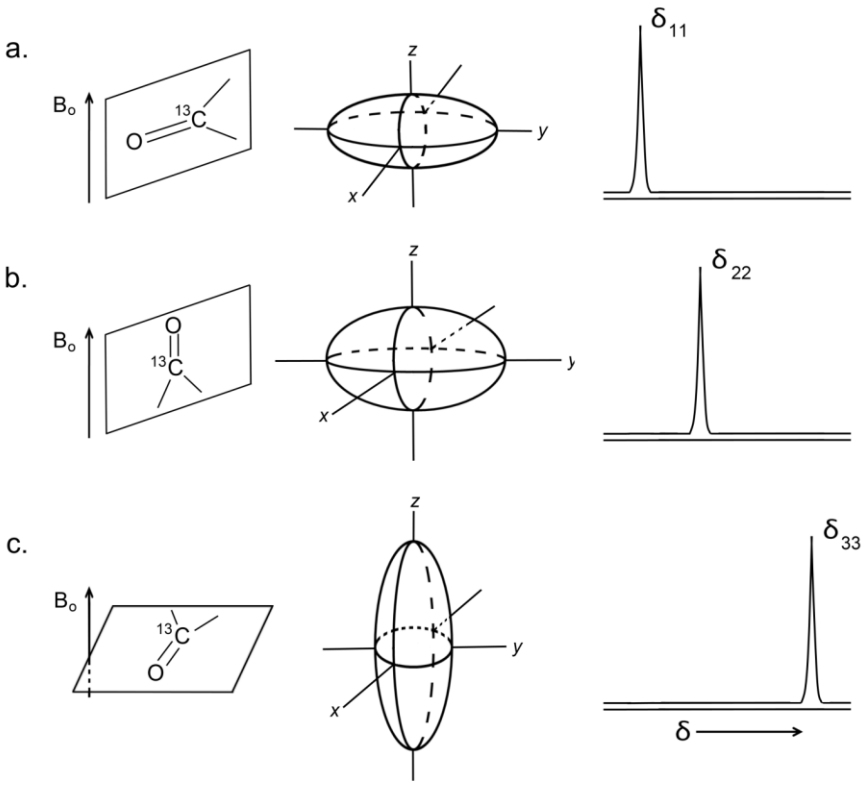

Figure 1.5 The principal components of the chemical shift anisotropy (CSA): (a) δ_{11}, (b) δ_{22}, and (c) δ_{33} arising from the orientation dependence of induced local magnetic field experienced by the molecule or crystal in the external magnetic field, B_o. Figure reproduced from Laws et al. 2002.[46]

The orientation dependence of the strength of the induced localized magnetic field surrounding an observed nucleus is called the chemical shift anisotropy (CSA). In a powder, all possible molecular orientations are present in a random distribution, giving rise to different, typically broad, spectral lines for each orientation. These lines for different orientations overlap, producing the observed powder pattern (Figure 1.6).[47]

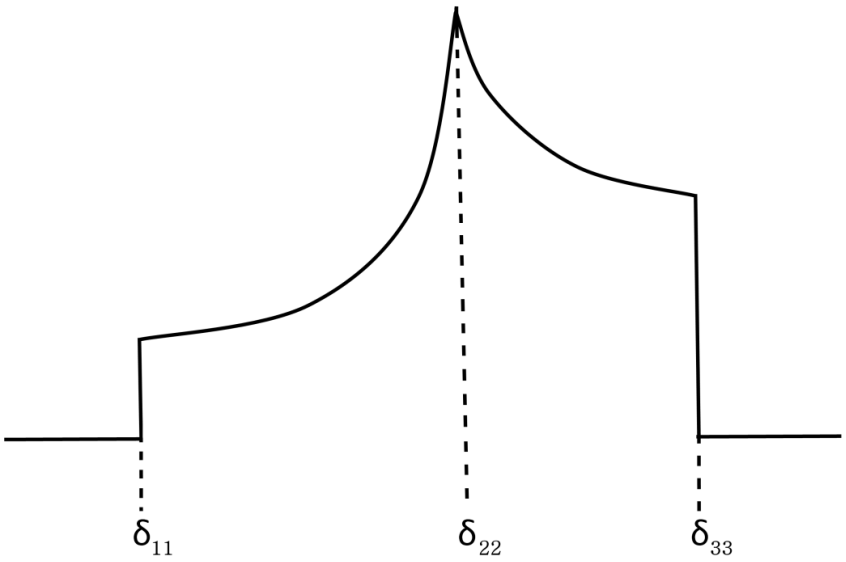

Figure 1.6 The CSA powder pattern lineshape resulting from the continuous overlap of each spectral line that arise from the presence of a random distribution of all molecule (or crystal) orientations. Figure reproduced from reference 46.

The chemical shielding Hamiltonian for a spin I is:

$$\hat{H}_{cs} = -\gamma\hbar\,\hat{I}\cdot\boldsymbol{\sigma}\cdot B_o$$

where γ is the gyromagnetic ratio and σ is the chemical shielding tensor, a second rank tensor. If the axis frame for this tensor is chosen such that σ is diagonalized, then the values along the resulting diagonal of the tensor are the principal values of the shielding tensor (δ_{11}, δ_{22}, δ_{33}) from which the values of the isotropic shift, δ_{iso}, the anisotropy, Δ, and the asymmetry, η, can be calculated. These values give information regarding the symmetry of the local environment of the observed nucleus and are defined by the principal components of the CSA:

$$\delta_{iso} = \frac{1}{3}(\delta_{11} + \delta_{22} + \delta_{33})$$

$$\Delta = \delta_{11} - \delta_{iso}$$

$$\eta = \frac{\delta_{33} - \delta_{22}}{\delta_{11}}$$

b. Dipolar Coupling

Yet another interaction with an observed nucleus is that of dipolar coupling, a through-space interaction between nuclear spins. A magnetic field at the observed nucleus, labeled spin I, is induced when placed in the external magnetic field, B_o. The same will occur to a second nucleus placed in the field, labeled spin S. If spin I and spin S are spatially close, they can interact with one another, modulating the magnetic field of both nuclei. This dipolar interaction between nuclei can be *homonuclear* if spin I and spin S are the same or *heteronuclear* if spin I and spin S are different nuclei. The strength of dipolar coupling is given by:

$$d = \hbar\left(\frac{\mu_o}{4\pi}\right)\frac{1}{r^3}\gamma_I\gamma_S$$

Where μ_o is the permeability of free space, r is the distance between the spins I and S, and γ_I and γ_S are the gyromagnetic ratios of spin I and S, respectively. From this definition, it is clear that the strength of the dipolar coupling is inversely proportional to the cube of distance between the interacting spins, r, and directly proportional to the gyromagnetic ratios of both spins. The dipolar interaction is also dependent on the orientation, of the vector between spin I and spin S, relative to B_o, related in the dipolar Hamiltonian by a $(3\cos^2\theta - 1)$ term (Figure 1.7). As a result, the magnitude of the dipolar coupling will be greater for certain orientations of this vector with the B_o field than for other orientations.

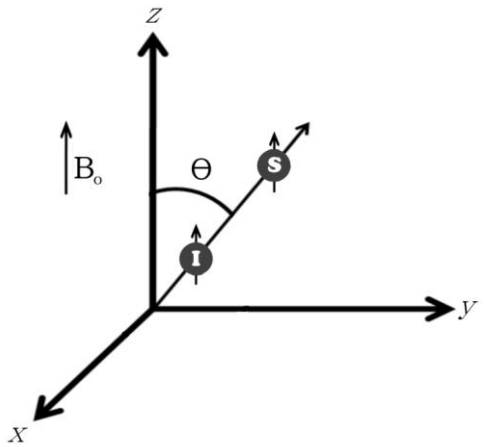

Figure 1.7 Illustration of the vector between spins I and S relative to the B_o field. Reproduced from Laws et al. 2002.[46]

For a static powder sample in the B_o field, the random orientation of crystallites in the dipolar coupling in the sample would produce a spectrum similar to the one shown in Figure 1.8, provided there are no other orientation-dependent interactions. This lineshape is referred to as a Pake doublet and arises from energy differences in the different orientations of the internuclear I spin – S spin vector relative to the B_o field. The differences in the intensities represent the distribution of the various crystallite orientations. An orientation of the internuclear I spin – S spin vector at an angle of $\theta = 54.7°$ relative to B_o has no effect on the resonance frequency of the observed nucleus. A commonly used technique in solid state NMR called "magic angle spinning," or MAS, takes advantage of this "magic angle" at 54.7°. Magic angle spinning will be discussed in more detail in the section entitled "Magic Angle Spinning (MAS) NMR".

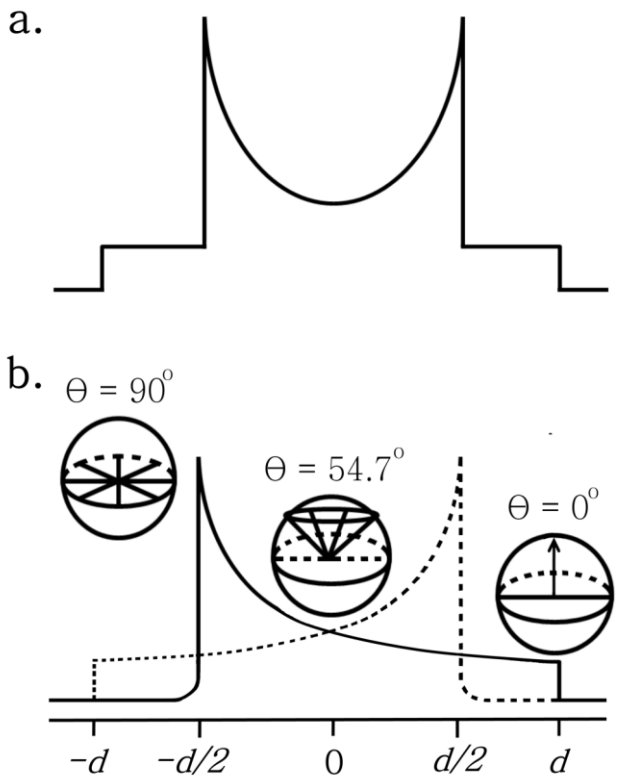

Figure 1.8 The dipolar Pake doublet lineshape for two coupled spins in a powder sample. (a) the resulting lineshape due to the orientation dependence of the coupled spins (when no other orientation dependent interactions are present) (b) contributions from the different orientations. The orientation of the coupled spin vector (relative to the B_o field) at 90°, 54.7° and 0° are represented to show the major features of the Pake doublet lineshape. Figure reproduced from Laws et al. 2002.[46]

c. Quadrupolar Coupling

NMR active nuclei with a spin > 1/2 are quadrupolar nuclei and contain a non spherical charge distribution at the nucleus. This asymmetric charge distribution at the nucleus is described by the nuclear electric quadrupole moment $e\boldsymbol{Q}$, an intrinsic property of the nucleus that is unaffected by local environment. The nuclear quadrupole moment couples with the electric field gradient (EFG) that is generated by electron density of the atoms surrounding the observed nucleus in the molecule or crystallite. The magnitude of the quadrupolar coupling is given by the equation:

$$\chi = \frac{e^2 q_{zz}\, Q}{\hbar}$$

where eq_{zz} is the tensor describing the EFG at the nucleus. The asymmetry parameter describing the symmetry of the EFG at the nucleus is defined as:

$$\eta_Q = \frac{q_{xx} - q_{yy}}{q_{zz}}$$

Quadrupolar coupling affects the energies of the transition states of the quadrupolar nucleus, (referred to as the Zeeman levels) that are corrected in the quadrupolar hamiltonian. Figure 1.9 depicts the Zeeman levels and the changes in energies of the transitions for the first and second order quadrupolar coupling for S = 1 and S = 3/2 nuclei.

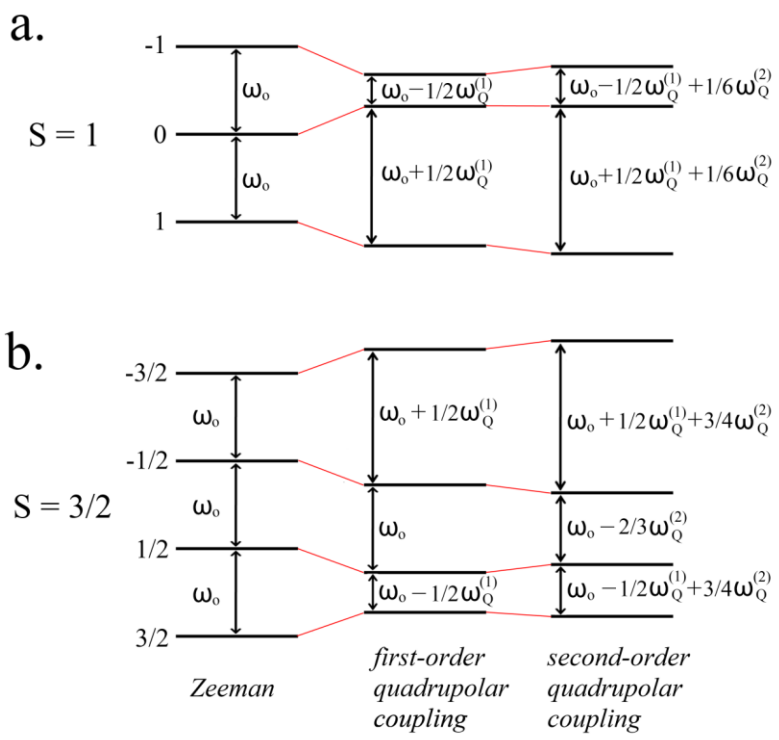

Figure 1.9 The effects of first- and second-order quadrupolar coupling on the Zeeman levels of (a) S = 1 and (b) S = 3/2 nuclei, where $\omega_Q^{(1)}$ is the coupling constant associated with the first order quadrupolar Hamiltonian and $\omega_Q^{(2)}$ is the coupling constant associated with the second order quadrupolar Hamiltonian.

This work uses ^{2}H and ^{23}Na NMR, which are S = 1 and S = 3/2 nuclei, respectively. For S = 1 nuclei, the first order quadrupolar coupling notably changes the energies of the Zeeman levels (Figure 1.9). The alteration of the Zeeman energy levels via quadroplar coupling manifests in the NMR spectrum as significant line broadening that can often result in the spectrum being uninterpretable. Using specific NMR techniques, as will be discussed later, the first order coupling can be effectively removed due to a similar orientation dependence to that mentioned for dipolar coupling. Second-order quadrupolar coupling is more difficult to remove, but for the case of deuterium NMR, the magnitude of the coupling typically involved is small enough that the interpretation of spectra is rarely hindered by second-order spectral broadening. For S = 3/2 nuclei such as ^{23}Na, the effect of quadrupolar coupling on the Zeeman levels is different; under the first-order quadrupolar interaction, the energy levels of the -1/2 → -3/2 and 1/2 → 3/2 satellite transitions are shifted and broadened, often obscuring observation of these transitions spectrally, while the -1/2 → 1/2 central transition remains unaffected. The central transition is,

however, still significantly broadened by second-order quadrupolar interaction. The strength of this coupling is gauged by a coupling constant, $\omega_Q^{(2)}$, given by:

$$\omega_Q^{(2)} = \frac{(\omega_Q^{(1)})^2}{2\omega_o}$$

where ω_o is the Larmor frequency of the observed nucleus, where $\omega_Q^{(1)}$ is the coupling constant associated with the first order quadrupolar Hamiltonian. The inverse dependence of the second-order coupling on ω_o can often make it advantageous to observe these nuclei at higher magnetic fields. Unfortunately the orientation dependence of the second-order quadrupolar coupling is more complicated than the first-order coupling and complete removal requires more complicated methods than are employed in this study.

Motional dynamics within the solid will affect the quadrupolar coupling. Any sort of motion, whether the motion involves the quadrupolar nucleus itself, or nearby surrounding atoms, will alter the electric field gradient (EFG) surrounding the observed nucleus. The alteration of the EFG experienced by the quadrupolar nucleus will affect the linewidths of the isotropic resonances, contributing to further broadening.[48] However, in the case of fast molecular motion (on the order of 10^{-12} s), the quadrupolar tensor may be completely averaged out and linewidths are narrowed.[49] Variable temperature experiments can be performed in order to analyze these linebroadening or narrowing effects in order to extract information regarding the timescales of the motions responsible for the broadening.[50, 51] This is particularly useful in the case of ^{2}H NMR where the quadrupolar coupling is considerably smaller (between 100 and 250kHz) compared to other quadrupolar nuclei (on the order of MHz) and therefore powder lineshapes can typically be observed for static spectra. The use of magic angle spinning (MAS), an NMR technique introduced after explanation of all the interactions relevant to the materials discussed in this thesis, to resolve distinct environments can be complicated by the presence of reorientational dynamics, (particularly when the rate of MAS rotation is on the order of the motion) effectively preventing the averaging of anisotropic interactions and resulting in considerable broadening of the MAS spinning sidebands.

d. Paramagnetic Coupling

Fermi-Contact Interaction

The Fermi-contact interaction is present in materials with localized unpaired electrons that create an additional magnetic field at the nucleus in the presence of B_o, causing coupling between the electron and the nucleus. Unpaired spin polarization is induced in the s orbitals of the nucleus, which in turn interacts with the nuclear magnetic moment, producing a frequency shift which is given by:

$$\Delta\omega_c = (A/\hbar)\gamma B_o\langle S_z\rangle$$

where $(A/\hbar)$ is the electron-nucleus hyperfine-coupling in Hz, and $\langle S_z\rangle$ is the expectation value of S_z, the time average of the local field that the nuclear spin couples to due to the rapid thermal flipping of the electron spin. The strength of this interaction is greatly attenuated when the observed nucleus is not the ion with the unpaired electrons. However, when this is the case, the Fermi-contact interaction still imparts a hyperfine shift via transfer of the spin polarization on the s orbital via chemical bonds to the observed nucleus. This effect can still be strong, but decreases rapidly as the number of intermediate bonds increases. For the observed nuclei in the systems discussed in this thesis, the Mn(III) and Mn(IV) paramagnetic ions produce a through-bond Fermi-contact interaction via an intervening oxygen anion. The sign and magnitude of the imparted hyperfine shift is strongly dependent on the M-O-X bonding angles and distances. Previous studies have determined Mn-O-X bonding angles close to 90° impart a positive shift (Figure 1.10 a.) and Mn-O-X bonding angles close to 180° impart a negative shift (Figure 1.10 b.).[52]

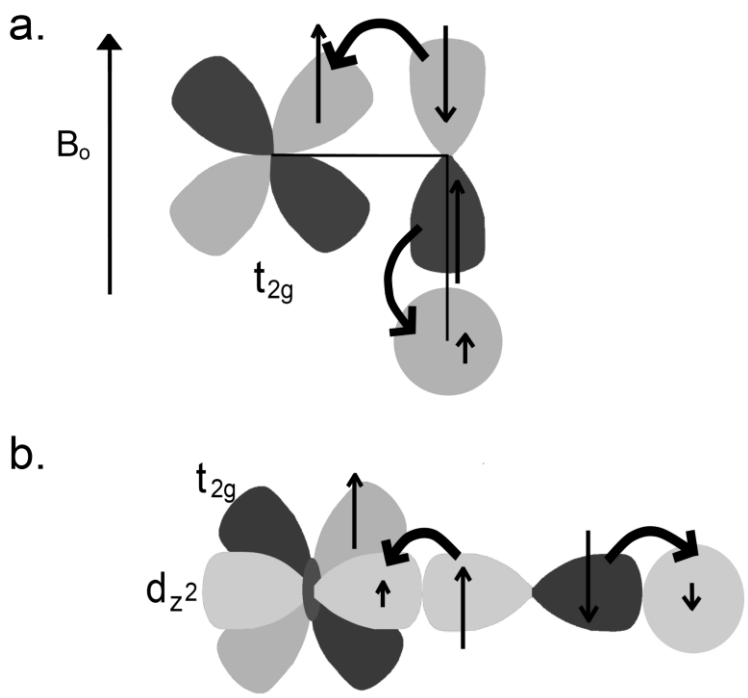

Figure 1.10 (a) transfer of polarized spin density of unpaired electrons in a partially filled t_{2g} orbital via a 90° M-O-X bond angle (where M = Mn and X = observed nucleus) involving the 2p oxygen orbital and the s orbital of the observed nucleus. (b) polarized spin density of unpaired electrons via transfer through a 180° M-O-X bond angle involving an empty d_z^2 manganese orbital, 2p oxygen orbital and the s orbital of the observed nucleus.

This interaction is generally accepted as additive, such that each contact the observed nucleus has to a paramagnet contributes some magnitude to the overall observed hyperfine shift.[52] The combination of the additive nature of the interaction, as well as its sensitivity to oxidation state, bonding angles and bonding distances, makes it a valuable interaction for the interpretation of the NMR spectra presented in this work and will be discussed in detail in subsequent chapters.

e. Pseudocontact Shift

While the Fermi-contact interaction is typically the dominant interaction, there is also the possibility of through-space dipolar coupling of the nucleus with the unpaired electrons of the paramagnet, referred to as the pseudocontact shift. This interaction is particularly important for the deuterium NMR of manganese oxides, where the dipolar coupling between electronic and

nuclear moments introduces anisotropy into the spinning sideband manifold lineshapes, and is also typically responsible for the large width of the resulting spinning sideband manifolds.

f. Magic Angle Spinning (MAS) NMR

There are a variety of interactions in solid state NMR spectroscopy that contribute to significant line broadening that complicate interpretation of spectra. Conversely in liquid NMR, many of these discussed complications are not observed due to fast molecular motion which averages anisotropic interactions present in the molecule and give rise to sharp spectral resonances.[53] The technique of magic angle spinning has been developed for solid state NMR, essentially simulating the molecular motion of liquid samples by rotation of the powder sample.

Briefly, MAS involves spinning a cylindrical rotor containing the solid sample at high speeds at the "magic angle" of θ = 54.7° (Figure 1.11) This technique aids in the elimination of anisotropic interactions such as the CSA (with sufficient spinning speeds) heteronuclear dipolar coupling and first-order quadrupolar coupling. A more detailed discussion of how these interactions are eliminated by the MAS technique can be found elsewhere.[46, 54]

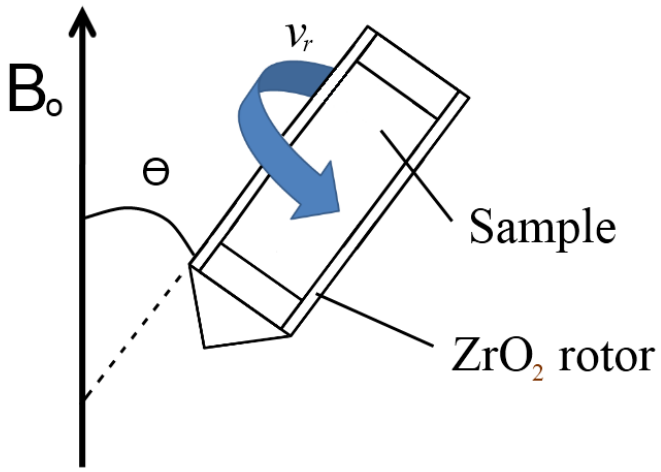

Figure 1.11 Schematic representation of magic angle spinning. Sample is rotated at high speeds, vr, at an angle, θ = 54.7° relative to the external magnetic field, B_o.

In order to completely eliminate the powder line shape of the chemical shift anisotropy that is observed in static samples, one must spin the sample at a frequency, ν_r, greater than that of the anisotropic interaction - particularly in this work, the first order quadrupolar interactions and

dipolar coupling to unpaired electrons; under these conditions, a single resonance is observed. However, this condition can often not be met and the resulting NMR spectrum exhibits a series of narrowed peaks spaced at integer multiples of the rotor spinning frequency, relative to the isotropic resonance. This series of peaks is referred to as "spinning sidebands." The spinning speeds used in this work range from 12kHz to 40kHz and are insufficient to eliminate the presence of all spinning sidebands.

g. Spin-Echo

One of the most basic pulse sequences used in solid state NMR, and the sequence used in this study, is the Spin-Echo.[55] Systems under investigation often have rapidly decaying free induction decays (FID) due to any number of interactions causing line broadening, such as chemical shift anisotropy and dipolar coupling. The Spin Echo pulse sequence enables the refocusing of dephasing due to these interactions, and allows the collection of the top of the echo, which corresponds to the start of the spectral FID. The Spin Echo also helps to reduce spectral artifacts introduced by probe and spectrometer hardware such as probe ringing. The pulse sequence consists of a $\pi/2$ pulse to rotate the magnetization from the z-axis into the xy plane, followed by a time delay that is an integer multiple of the rotor spinning speed, τ. Following τ, a π pulse is applied, inverting the magnetization in the xy plane. After a second delay, τ_1, the magnetization is refocused and the FID can be collected (Figure 1.12)

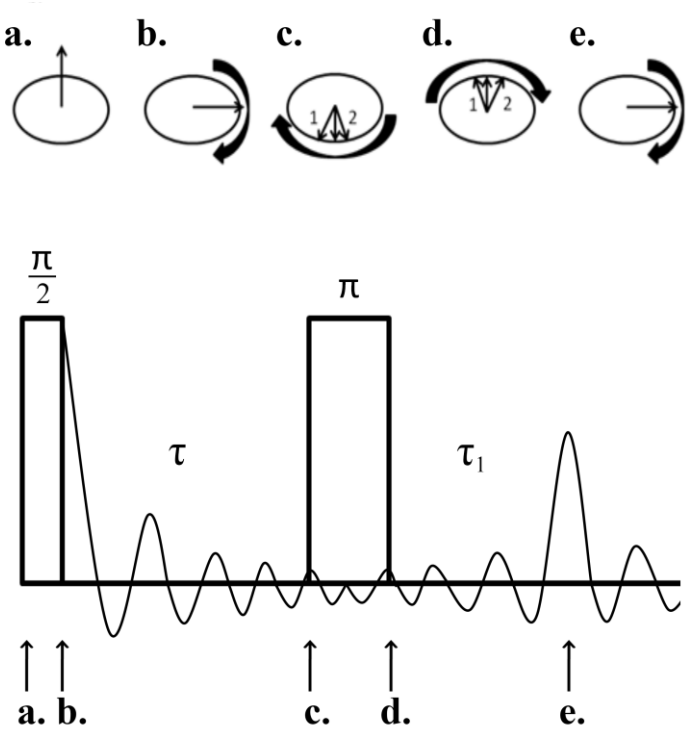

Figure 1.12 The Spin-Echo pulse sequence is shown. (a) Net magnetization builds up along the external magnetic field, taken to be the z-axis. (b) a 90° is applied to the net magnetization, rotating it into the xy plane. (c) once the pulse is stopped, the net magnetization vector precesses in the *xy* plane. Individual magnetization vectors precess at slightly varying Larmor frequencies, due to the inhomogeneities experienced in the external magnetic field, causing dephasing. (d) after the τ delay, a 180° pulse is applied, inverting the magnetization that has begun to dephase in the *xy* plane. (e) A second delay, τ_1 allows for the magnetization to rephase, at which time data collection is begun in order to catch the top of the echo of the FID.

B. Extended X-ray Absorption Fine Structure (EXAFS)

X-ray absorption fine structure (XAFS) is an element specific technique that probes the local environment of the target nucleus using a focused monochromatic beam of X-rays that is incident on the sample. The property measured by XAFS is the X-ray absorption coefficient μ(*E*), which is a measure of how strongly X-rays are absorbed by a sample as a function of the X-ray energy, *E*.[56] The energy of the incident monochromatic X-rays is varied, scanning through a specific range characteristic of the ionization energy of a core electron from the observed nucleus. At the X-ray energy equal to that of the ionization energy of the observed nucleus, a sudden increase in the absorption is observed. This increase in absorption is referred to as the "white line" and corresponds to transitions of the initial s and p electrons to a higher density of

final states due to electronic band-structure and is the X-ray absorption near edge structure (XANES) region of the XAFS spectrum (Figure 1.12). The XANES region ranges approximately from -50 to +200eV relative to the edge energy. The resulting ejected photoelectron from the absorption edge, treated as a propagating wave, is backscattered by the surrounding nuclei, creating what is referred to as the extended X-ray absorption fine structure (EXAFS) portion of the XAFS spectrum. (Figure 1.12)

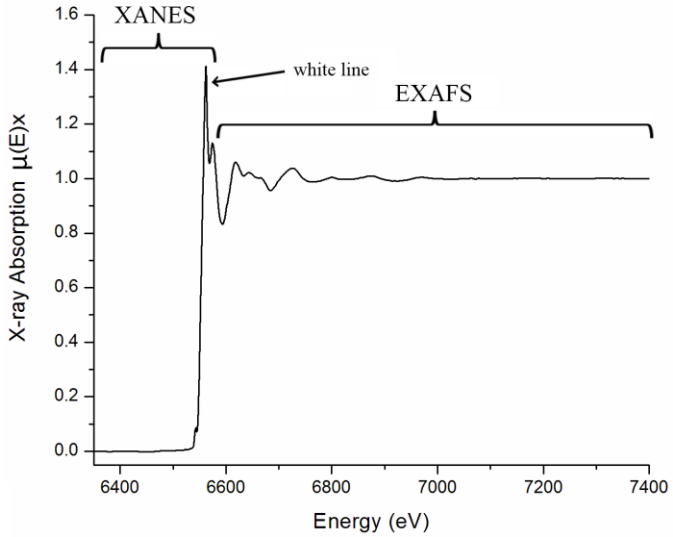

Figure 1.13 Representative normalized XAFS spectrum. The XANES region corresponds to the region directly before and after the absorption edge in which the X-rays are absorbed and thus, eject a core electron in the observed nucleus. The EXAFS region corresponds to the surrounding atoms backscattering the ejected photoelectron giving rise to oscillations in this region of the spectrum.

a. Preparation for Data Collection

XAFS spectra can be measured in several modes including transmission, fluorescence and electron yield. The choice of which mode is needed for data collection is dependent on a number of factors regarding the nature of the sample. For the work described in this thesis, transmission mode was used for the collection of all XAFS spectra presented and therefore, only the process of transmission data collection will be introduced.

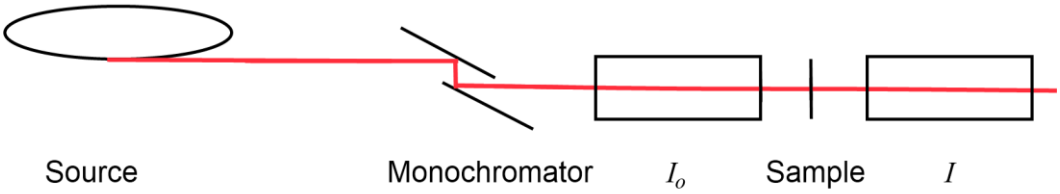

Figure 1.14 The experimental setup for transmission collection of XAFS spectra. Figure reproduced from reference 51.

Transmission mode simply compares the incident X-ray flux before, I_o, and after, I, the beam passes through a uniform sample (Figure 1.13).[56] The values of I_o and I correspond to the X-ray absorption coefficient μ(E) through the equation:

$$\mu(\mathrm{E})x = \ln (I_o/I)$$

Sample preparation for transmission data collection requires dilution of the sample to optimize the amount of the incident beam absorbed by the sample.[57] The diluent used must have a low absorption coefficient, μ, at the energy range being used, be chemically stable and not reactive with the sample. Boron nitride is typically used, however, the samples prepared for XAFS data collection in this thesis have been diluted with sucrose.

b. Data Processing

The EXAFS spectra, $\chi(k)k$, contains information pertaining to the structure surrounding the absorbing atom, and can be described as a sum of sine waves, the phase and amplitude of which, depend on the distance between the absorber atoms and the coordinating atoms as well as the type of coordinating atoms.[57] This signal can be Fourier transformed, $|\chi(R)|$, separating out each frequency component in distance R. Each of these Fourier components is defined by a phase and amplitude for which modeling software is readily available for structural analysis. However, before the experimental data can be Fourier transformed for such analyses, processing is required. A number of spectra are typically collected per sample so that the spectra can be summed and the signal to noise in the spectrum can be improved. In order to do this, energy calibration and "deglitching" often need to be addressed first.

Spectra can be calibrated after data collection, but it is easiest to correct for calibration errors during data collection. This can be done by measuring the absorption edge of a standard compound, such as potassium permanganate, which has a sharp pre-edge feature at 6543.34eV.

Monochromator and/or source instabilities, sample inhomogeneities and a number of other problems can lead to spectral artifacts, referred to as "glitches." If the glitch is only a single energy point in the spectrum, it can usually be removed without concern, however, removal of glitches spread over a number of energy points may risk altering the data. Therefore, it is often best to address significant glitches in a spectrum during data collection by optimizing the experiment and recollecting data.

In order to compare the spectra of different samples, normalization of the spectra is required. This process scales data so that the intensity of the absorption edge jump is set to one. The pre- and post-edge regions of a spectrum are fit using low order polynomial functions. The regions chosen for fitting the pre- and post-edge must exclude the XAFS right at the edge. This region is highly dependent on local structure and therefore, it is undesirable to include this in the normalization.[57]

After normalization, a background subtraction is usually performed on the EXAFS region of the spectrum. This separates the EXAFS oscillations from the slowly varying background frequencies by fitting the general curve of the data using a spline in which the number of knots (controlling the flexibility of the spline) can be varied. Care must be taken to include as few knots in the spline as possible since, as the flexibility of the spline increases, subtraction of the EXAFS data along with the background becomes problematic.

Finally, the range of the EXAFS data to be Fourier transformed must be chosen. While the greater the range of data, the greater the resolution of the corresponding interatomic distances in the Fourier transformed spectrum, poor signal to noise in the higher range of data may require exclusion. A window function may be applied to the Fourier transform window to reduce what is known as a Fourier transform ripples that occurs due to the Fourier transform of a finite range of EXAFS data. The window chosen is usually very mild to avoid altering the data, gradually bringing the edges of the data to zero rather than the abrupt steps to zero at the beginning and ends of the zero filled EXAFS data set. The amplitudes of the oscillations in the EXAFS data diminish with increasing energy, so it is often necessary, for the sake of structural analysis peak fitting, to apply a *k* weight factor that will emphasize these higher energy oscillations.

c. Structural Modeling

While model development specifically regarding layered manganese oxides is thoroughly detailed in Chapter 5, it is briefly introduced now. A starting model structure, similar to what is expected for the compound being modeled, must be used to generate a file containing the coordinates for all atoms in a cluster of a defined size. Depending on the intended fitting requirements, the size of the cluster can be chosen accordingly, though backscattering is minimally important beyond 8 or 9Å. A program is then used to generate all possible scattering paths from the file containing the coordinates of all atoms in the defined cluster. Constraints such as backscattering paths composed of no greater than 4 single scattering path legs are typically used for calculating multiple scattering paths, otherwise an unmanageable number of paths are generated. The relevant scattering paths must then be selected and parameterized in a modeling software program, simulating the EXAFS spectrum (and Fourier transformed spectrum) and optimizing the parameters so that a good fit can be obtained.

C. Powder X-ray Diffraction (XRD)

Powder XRD utilizes the diffraction of X-rays incident on a crystalline sample. The X-rays cause the orbital electrons of atoms in a crystallite to oscillate and emit X-rays of the same frequency as the incident X-rays in all directions.[58] The atoms involved in this process are said to *scatter* the primary beam, and this scattering produces a pattern of diffracted X-rays. Figure 1.15 shows a simplified schematic to illustrate the relatively complex phenomenon of this scattering.

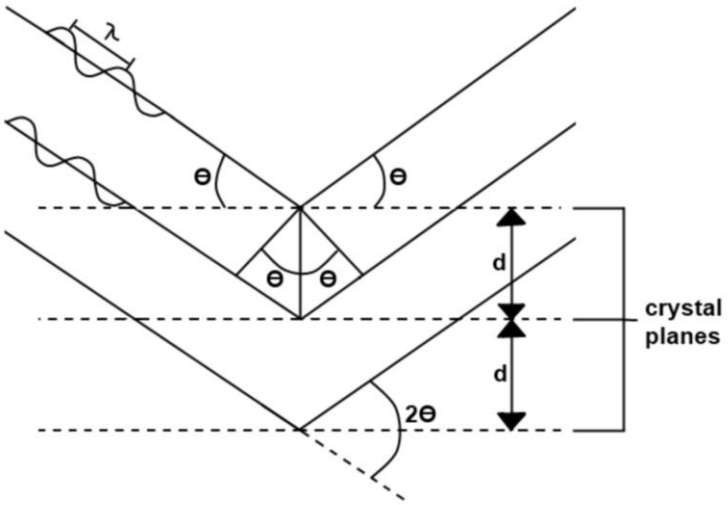

Figure 1.15 Schematic representation of the scattering, or diffraction, of incident x-rays off of atoms in evenly spaced planes in a crystal structure. Theta (θ) is the angle of the incident x-ray beam with respect to the atomic planes; d is the spacing between the equivalent atomic planes; two theta (2θ) is the angle that the diffracted beam deviates from the incident beam. Lambda (λ) is the wavelength of the radiation. When incident x-rays diffract off multiple atomic planes such that the sum of the angles of the incident and diffracted beams are equal to an integer (*n*) multiple of λ, the diffracted beams will be in phase, producing constructive interference that will give rise to the XRD reflections in the powder pattern.

Envisioning a series of evenly spaced planes of atoms in a crystal structure, the distance between a given set of planes is called the *d-spacing*, and can be determined quite accurately with XRD. The principles underlying this determination are given by the Bragg equation:

$$n\lambda = 2d \sin\theta$$

Different symmetries of various crystalline structures will produce different *diffraction patterns* that can be used to determine where the atoms are located within a crystal lattice. As a result, X-ray diffraction powder patterns have reflections that are compound specific, as a sort of "fingerprint" for powdered samples While XRD can be used for extensive crystallographic structural analyses of materials by Rietveld refinement, this work uses powder XRD mainly for phase identification.

D. Transmission Electron Microscopy (TEM)

TEM is a microscopy technique used to image materials via the transmission of monochromatic electrons through the sample. The amount of transmission through the sample depends on the thickness and/or density at each point in the area being imaged, producing an image that gives information regarding particle size and morphology.

E. Scanning Electron Microscopy (SEM)

SEM is another form of microscopy that images materials using a high energy beam of electrons. Different SEM signals, generated by the electrons interacting with the atoms in the sample, can be detected by various types of SEM microscopes, such as secondary electrons (ionization products such as photoelectrons), back-scattered electrons or characteristic X-rays. In this work, a back-scatter electron (BSE) detector is used for image collection. The signal of the BSE is determined by the atomic number (Z), and can therefore provide information on the distribution of specific elements within a sample.

II. Research Strategy

In this report, ^{23}Na state NMR spectroscopy is used to interpret individual contributions of $Mn^{3+/4+}$-O-Na^{+} to the overall observed Fermi-contact hyperfine shift in a variety of mixed valence sodium manganese oxides. The trends observed in these model compounds are then used to investigate the interlayer cation order and possible layer Mn^{3+}/Mn^{4+} ion ordering in triclinic forms of birnessite. ^{2}H solid state MAS NMR is used to investigate layer vacancies in hexagonal acid birnessites, and low temperature experiments are explored to understand the dynamics of exchange between layer deuterons and interlayer crystalline waters. Construction and parameterization of a model birnessite structure is performed to refine Mn k-edge EXAFS data of these hexagonal acid birnessites. Simplification of the currently complex structural models available for these materials is explored as a way to make the use of such a model, more "general-user friendly."

III. References

1. Post, J. E., *P Natl Acad Sci USA* **96**, 3447-3454 (1999).

2. Vodyanitskii, Y. N., *Eurasian Soil Sci+* **42**, 1170-1178 (2009).

3. Grangeon, S., Lanson, B., Miyata, N., Tani, Y., Manceau, A., *Am. Mineral.* **95**, 1608-1616 (2010).

4. Leeper, G. W., Uren, N.C. , *Soil Science, An Introduction*. (Overseas Press India Private Limited, New Delhi, ed. Fifth, 2006), pp. 300.

5. Tebo, B. M., *Deep-Sea Research Part a-Oceanographic Research Papers* **38**, S883-S905 (1991).

6. Bargar, J. R., Tebo, B. M., Villinski, J. E., *Geochim. Cosmochim. Acta* **64**, 2775-2778 (2000).

7. Bricker, O., *Am. Mineral.* **50**, 1296-& (1965).

8. Mckenzie, R. M., *Geochim. Cosmochim. Acta* **43**, 1855-1857 (1979).

9. O'Reilly, S. E., Hochella, M. F., *Geochim. Cosmochim. Acta* **67**, 4471-4487 (2003).

10. Lanson, B., Drits, V. A., Gaillot, A. C., Silvester, E., Plancon, A., Manceau, A., *Am. Mineral.* **87**, 1631-1645 (2002).

11. Toner, B., Manceau, A., Webb, S. M., Sposito, G., *Geochim. Cosmochim. Acta* **70**, 27-43 (2006).

12. Sherman, D. M., Peacock, C. L., *Geochem. Cosmochim. Ac.* **74**, 6721-6730 (2010).

13. Pena, J., Kwon, K. D., Refson, K., Bargar, J. R., Sposito, G., *Geochim. Cosmochim. Acta* **74**, 3076-3089 (2010).

14. Bargar, J. R., Fuller, C. C. , Marcus, M. A., Brearley, A. J., De la Rosa, M. P., Webb, S. M., Caldwell, W. A. , *Geochim. Cosmochim. Acta* **73**, 889-910 (2009).

15. Kuma, K., Usui, A., Paplawsky, W., Gedulin, B., Arrhenius, G., *Mineral Mag* **58**, 425-447 (1994).

16. Tevar, A. D., Whitacre, J. F., *J. Electrochem. Soc.* **157**, A870-A875 (2010).

17. Whitacre, J. F., Tevar, A., Sharma, S., *Electrochem. Commun.* **12**, 463-466 (2010).

18. Caballero, A., Hernan, L., Morales, J., Sanchez, L., Santos Pena, J., Aranda, M. A. G., *J. Mater. Chem.* **12**, 1142-1147 (2002).

19. Tsuda, M., Arai, H. Sakurai, Y., *J. Power Sources* **110**, 52-56 (2002).

20. Bach, S., Pereira-Ramos, J. P., Cachet, C., Bode, M., Tse Yu, L. , *Electrochim. Acta* **40**, 785-789 (1995).

21. Bach, S., Pereira-Ramos, J. P., Baffier, N., *J. Electrochem. Soc.* **143**, 3429-3434 (1996).

22. Post, J. E., Heaney, P. J. , Hanson, J., *Powder Diffr.* **17**, 218-221 (2002).

23. Giovanoli, R., Stahli, E., Feitknecht, W., *Helv. Chim. Acta* **53**, 209-220 (1970a).

24. Lanson, B., Drits, V. A., Silvester, E., Manceau, A., *Am. Mineral.* **85**, 826-838 (2000).

25. Lanson, B., Drits, V. A., Feng, Q., Manceau, A., *Am. Mineral.* **87**, 1662-1671 (2002).

26. Rogers, D. B., Germann, R. W., Arnott, R. J., *J. Appl. Phys.* **36**, 2338-2343 (1965).

27. Potter, R. M., Rossman, G. R., *Am. Mineral.* **64**, 1199-1218 (1979).

28. Giovanol.R, *Chimia* **23**, 470-& (1969).

29. Post, J. E., Veblen, D. R., *Am. Mineral.* **75**, 477-489 (1990).

30. Cui, H. J., Qiu, G. H., Feng, X. H., Tan, W. F., Liu, F., *Clays Clay Miner.* **57**, 715-724 (2009).

31. Feng, X. H., Liu, F., Tan, W. F., Liu, X. W., *Clays Clay Miner.* **52**, 240-250 (2004).

32. Post, J. E., Heaney, P. J., Hanson, J., *Powder Diffr.* **17**, 218-221 (2002).

33. Webb, S. M., Tebo, B. M., Bargar, J. R., *Geomicrobiol. J.* **22**, 181-193 (2005).

34. Drits, V. A., Silvester, E., Gorshkov, A. I., Manceau, A., *Am. Mineral.* **82**, 946-961 (1997).

35. Drits, V. A., Lanson, B., Gorshkov, A. I., Manceau, A., *Am. Mineral.* **83**, 97-118 (1998).

36. Lopano, C. L., Heaney, P. J., Post, J. E., Hanson, J., Komarneni, S., *Geochim. Cosmochim. Acta* **68**, A86-A86 (2004).

37. Lopano, C. L., Heaney, P. J., Post, J. E., Hanson, J., Komarneni, S., *Am. Mineral.* **92**, 380-387 (2007).

38. Giovanoli, R., Burki, P., Giuffredi, M., Stumm, W., *Chimia* **29**, 517-520 (1975).

39. Johnson, E. A., Post, J. E., *Am. Mineral.* **91**, 609-618 (2006).

40. Silvester, E., Manceau, A., Drits, V. A., *Am. Mineral.* **82**, 962-978 (1997).

41. Villalobos, M., Toner, B., Bargar, J., Sposito, G., *Geochim. Cosmochim. Acta* **67**, 2649-2662 (2003).

42. Villalobos, M., Lanson, B., Manceau, A., Toner, B., Sposito, G., *Am. Mineral.* **91**, 489-502 (2006).

43. Post, J. E., Bish, D. L., *Am. Mineral.* **73**, 861-869 (1988).

44. Post, J. E., Heaney, P. J., Hanson, J., *Am. Mineral.* **88**, 142-150 (2003).

45. Post, J. E., Vondreele, R. B., Buseck, P. R., *Acta Crystallogr. Sect. B-Struct. Commun.* **38**, 1056-1065 (1982).

46. Laws, D. D., Bitter, H. M. L., Jerschow, A., *Angew Chem Int Edit* **41**, 3096-3129 (2002).

47. Duer, M. J., Ed., *Solid-State NMR Spectroscopy: Principles and Applications*, (Wiley-Blackwell, Oxford, ed. 1st, 2001), 1st, pp. 592.

48. Ashbrook, S. E., *PCCP* **11**, 6892-6905 (2009).

49. Ilott, A. J., Palucha, S., Batsanov, A. S., Wilson, M. R., Hodgkinson, P., *J. Am. Chem. Soc.* **132**, 5179-5185 (2010).

50. Nielsen, U. G., Heinmaa, I., Samoson, A., Majzlan, J., Grey, C. P., *Chem. Mater.* **23**, 3176-3187 (2011).

51. Griffin, J. M., Miller, A. J., Berry, A. J., Wimperis, S., Ashbrook, S. E., *PCCP* **12**, 2989-2998 (2010).

52. Grey, C. P., Dupre, N., *Chem. Rev.* **104**, 4493-4512 (2004).

53. Duer, M. J., *Introduction to Soild-State NMR Spectroscopy*. (Blackwell Publishing Ltd, ed. First, 2004), pp. 349.

54. Mackenzie, K. J. D., Smith, M. E., *Multinuclear Solid-State NMR of Inorganic Materials*. R. W. Cahn, Ed., Pergamon Materials Series (Elsevier Science Ltd., ed. 1st, 2002), vol. 6, pp. 727.

55. Fukushima, E., Roeder, S. B. W. , *Experimental Pulse NMR: A Nuts and Bolts Approach*. (Addison-Wesley Publishing Company, Inc, Reading, ed. First, 1981), pp. 539.

56. Bunker, G., *Introduction to XAFS: A Practical Guide to X-ray Absorption Find Structure Spectroscopy*. (Cambridge University Press, Cambridge, 2010), pp. 268.

57. Ulery, A. L., Drees, L. R., Eds., *Methods of Soil Analysis. Part 5. Mineralogical Methods*, vol. 5 (American Society of Agronomy, Madison, 2008), vol. 5, pp. 544.

58. Bloss, F. D., *Crystallography and Crystal Chemistry: An Introduction*. (The Mineralogical Society of America, Washington, D. C., ed. 2nd, 1994).

Chapter 2

^{23}Na NMR Study of Layered Sodium Manganese Oxides

Manganese oxides, in their various forms, have garnered great interest due to their prevalence in the environment, playing important roles as regulators in the geochemical cycling of cations of interest, and their utility as batter cathode materials. ^{23}Na NMR was applied to the study of a variety of layered sodium manganese oxides of varied Mn^{3+}:Mn^{4+} ratios. The use of ultra fast MAS techniques, as well as increasing magnet field strengths resolves the local sodium environments in these compounds. Using available crystallographic information from the literature, the magnitude and direction of hyperfine shift contributions Na^{+}-O-Mn^{3+} and Na^{+}-O-Mn^{4+} contact were reasoned. Overall, Na^{+}-O-Mn^{4+} contacts produce larger positive hyperfine contributions to the overall observed shifts than Na^{+}-O-Mn^{3+} contacts.

This chapter is adapted from a paper that has been prepared for publication.

I. Introduction

Manganese oxides are abundant and naturally occurring materials that have been shown to be excellent sorbents of cations.[1-4] With the prevalence of these materials occurring in nature as surface coatings on rocks and sediments, they exert significant influence on the geochemical cycling of various ions, of particular note, of those occurring as anthropogenic heavy metal pollutants. There are innumerable studies to elucidate the structure of various forms of manganese oxides, the ordering of sorbed counter ions, as well as many studies looking at the nature of adsorption of cations onto the surface and into the interlayers and tunnels of these materials via techniques such as Rietveld refinement of X-ray Diffraction (XRD) data, selected area electron diffraction (SAED) data, and fitting of Extended X-ray Absorption Fine Structure (EXAFS) spectra.[5-11] Synthetic forms of manganese oxides have been shown to be fair representatives of their naturally occurring counterparts, and are often used in these investigations due to the relative ease of characterization since more crystalline and ordered forms can be prepared.[2, 12]

There are also innumerable studies investigating and developing new, more efficient, less toxic and less costly battery materials, of which manganese oxides show substantial promise.[13-15] Various lithium manganese oxides have been studied via many techniques, including solid state NMR which has provided insight into the local environment of the lithium ions as they are charged and discharged in the battery.[16, 17] In an attempt to find more abundant, and therefore less expensive, battery materials, there are an increasing number of studies investigating the electrochemical performance of sodium manganese oxides which indicate these materials show significant potential as less toxic and less costly alternatives for battery cathode materials.[14, 18-22] Previous studies have found structural changes during intercalation and deintercalation of sodium ions consistent with changes in the oxidation state of manganese in layered sodium oxides, and increases in resistance to Na^+ removal in tunnel structure sodium manganese oxides when discharged beyond a certain voltage.[23] Having the means to probe the local environment of the sodium ions as they move through these various manganese oxide structures upon charge and discharge could provide invaluable insight for improving and maintaining the capacity of these cathode materials.

The work reported in this chapter, motivated by the growing importance of sodium forms of manganese oxides in several different fields of interest, uses solid state ^{23}Na Magic Angle Spinning Nuclear Magnetic Resonance (MAS NMR) to establish a baseline for interpretation of local environments in sodium manganese oxides. An important interaction to consider in ^{23}Na MAS NMR spectra of sodium manganese oxides is quadrupolar coupling from sodium, a I = 3/2 nucleus. Sodium has a moderately sized quadrupolar moment (0.14×10^{-28} m^2 A), yielding second-order quadrupolar line shapes under MAS at moderate fields. While this can complicate interpretation of NMR spectra, a combination of higher magnetic fields and faster MAS speeds help to reduce the effects of second order lineshapes.[17] These lineshapes can also be used to extract further information regarding the local environment of sodium via simulation of experimental NMR spectra.

Another important interaction, the Fermi-contact interaction, arises from the presence of paramagnetic manganese in these materials. Unpaired spin density of a paramagnet can impart a through-bond spin density transfer, producing a Fermi contact interaction which results in significantly larger isotropic resonance frequency shifts than those typically observed in diamagnetic systems.[17] The Fermi-contact shift is generally believed to be an additive interaction,[24] being the result of the summation of individual contributions from each existing M-X-A (M = paramagnet, X = anion, A = observed nucleus) contact. It is important to note however, that the magnitude and direction of the imparted Fermi-contact shift is strongly dependent on bonding angles, distance and oxidation state of the contributing paramagnet.[17] In practice, such values have been obtained through the analysis of model compounds with known structures, although theoretical studies of the shifts are developing useful contributions to this process.[25]

^{23}Na MAS NMR spectroscopy has been successfully used to investigate a number of paramagnetic materials,[26] and is used here, to the study of the local environments in various layered sodium manganese oxides with varied ratios of Mn^{3+}:Mn^{4+} composing the manganate layers. There is little background in ^{23}Na NMR of mixed valence manganese oxide systems and this study aims to develop an understanding of the influence of bonding angles and distortions on the observed hyperfine shifts in NMR spectra of the compounds investigated in this thesis. With a library of model compounds to help interpret spectra, a fundamental understanding of cation

adsorption or ion intercalation in sodium manganese oxides can be developed with this technique.

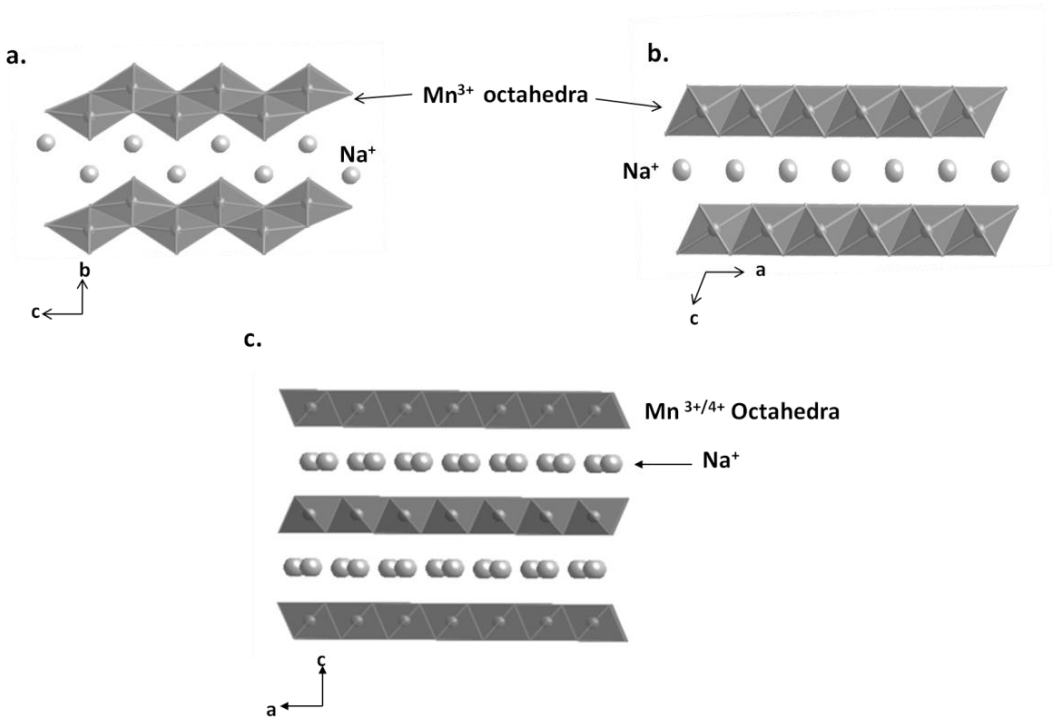

Figure 2.1 (a) β-$NaMnO_2$ structure composed of corrugated layers of Mn^{3+} octahedra sandwiching octahedrally coordinated interlayer sodiums. (b) α-$NaMnO_2$ structure composed of flat layers of Mn^{3+} octahedra. (c) α-$Na_{2/3}MnO2$ structure composed of stacked layers of Mn^{3+} and Mn^{4+} octahedra. Interlayer sodiums are prismatically coordinated by layer oxygens above and below. β-$Na_{2/3}MnO_2$ is an orthorhombic distortion of the layers of α-$Na_{2/3}MnO_2$.

Layered sodium manganese oxide compounds were chosen with varying Mn^{3+}/Mn^{4+} ratios. β-$NaMnO_2$, is a layered manganese oxide composed of corrugated sheets of Mn^{3+} octahedra sandwiching interlayer sodium cations (Figure 2.1 a.).[27] α-$NaMnO_2$, in contrast, is composed of flat sheets of Mn^{3+} octahedra sandwiching interlayer sodium cations (Figure 2.1 b.).[28] These two model compounds were chosen to illustrate the typical shifts associated with a sodium local environment composed entirely of Na^+-O- Mn^{3+} interactions and give some insight into the impact of differing bonding angles and distances on observed shifts in ^{23}Na spectra of these paramagnetic systems. α-$Na_{2/3}MnO_2$ and α-$Na_{2/3}Co_{2/3}Mn_{1/3}O_2$ were chosen as model compounds to observe the effect of an increasing number of Na^+-O-Mn^{4+} interactions in the local environment of sodium on observed ^{23}Na NMR shifts. α-$Na_{2/3}MnO_2$ is a layered manganese

oxide containing sheets composed of 2/3 Mn^{3+} and 1/3 Mn^{4+} ions, sandwiching prismatically coordinated interlayer sodium atoms (Figure 2.1 c.).[29] In contrast, while the structure of α-$Na_{2/3}Co_{2/3}Mn_{1/3}O_2$ is the same as the α-$Na_{2/3}MnO_2$ structure, the presence of Co^{3+} octahedra instead of Mn^{3+} ions in the manganese oxide layer results in only Na^+-O-Mn^{4+} contacts. The Na^+-O-Co^{3+} interactions in the sodium local environment involve diamagnetic Co^{3+} ions and not contribute to the overall hyperfine shift, which helps to provide insight into typical shifts associated with local environments encountering only Na^+-O-Mn^{4+} paramagnetic interactions. The structure of β-$Na_{2/3}MnO_2$ is obtained via an orthorhombic distortion of the ideal α-$Na_{2/3}MnO_2$ structure, the distortion arising from the elongation of axial Mn-O bonds and shortening of the equatorial Mn-O bonds of the Jahn-Teller Mn^{3+} ion within the manganese oxide layers. This model compound was used to examine the effect of the Jahn-Teller distortion on these mixed Mn^{3+}/Mn^{4+} phases.[30]

The ^{23}Na NMR spectra of the model compounds are presented in this work, and correlations are drawn between these spectra and their respective local sodium environment(s) which are taken from structural refinements in the literature. A summary of the results of the density functional theory (DFT) calculations for these compounds is presented in this chapter; more details on these analyses can be obtained from reference 37, cited throughout this chapter. This work gives insight into the effects of bonding angles and distortions on the magnitude of hyperfine shifts, and enables explanation of sodium ordering with respect to layer Mn^{3+} and Mn^{4+}.

II. Experimental

A. Synthetic Methods

β- and α-$NaMnO_2$ and $Na_{2/3}Co_{2/3}Mn_{1/3}O_2$ were synthesized by calcining pelletized powder mixtures at different temperatures, following procedures available in the literature.[28, 30] For α-$NaMnO_2$, the mixture consisted of stoichiometric amounts of Mn_2O_3 and Na_2CO_3, and was fired at 750ºC under flow of O_2 gas for 24 hours. β-$NaMnO_2$ was obtained by firing mechanically milled MnO_2 (Gretch Planetary ball mill, 600rpm for 20 minutes) and Na_2CO_3 at 950ºC under flow of O_2 gas for 24 hours. Finally, a mixture of Mn_2O_3, Co_3O_4 and Na_2CO_3 was calcined at 900ºC in air for 16 hours to prepare $Na_{2/3}Co_{2/3}Mn_{1/3}O_2$. The heating ramps were

5ºC/min in all cases, and the pellets were quenched to room temperature in liquid nitrogen after the treatment.

β-$Na_{2/3}MnO_2$ was synthesized by using a glycine combustion method, described by Dollé et al.[31] Briefly, stochiometric amounts of a 47.5% $Mn(NO_3)_2$ solution in 5% HNO_3 and $NaNO_3$ were mixed with glycine, added in a molar ratio of 1:2 (glycine:nitrate). The solution was then combusted in a stainless steel container on a hot plate by evaporating aliquots of the solution mixture to dryness. The resulting powder was ground, pressed into a pellet and calcined at 800ºC under flow of O_2 gas for 4 hours.

α-$Na_{2/3}MnO_2$ was prepared by following a sol-gel procedure first reported by Bach *et al.*[32] A 0.25M solution of $KMnO_4$ was mixed with fumaric acid in a molar ratio of 3:1, and was allowed to sit for 20 – 30 minutes until a brown gel formed. This gel was spread on a glass plate to dry, and, afterwards, was ground into a fine powder with mortar and pestle and pressed into pellets. The pellets were then calcined at 600ºC with a slow ramp up of 1ºC/min, and annealed for 2 – 3 hours. Finally, the pellets were quenched in liquid nitrogen.

In order to prevent α- and β-$NaMnO_2$ from oxidizing in air, they were stored under argon in a glove box. Similarly, α- and β-$Na_{2/3}MnO_2$ are sensitive to moisture and, hence, were stored in a desiccator.

B. XRD

X-ray diffraction data was collected on a Scintag diffractometer (Cu Kα radiation, λ = 1.54Å) or a Rigaku Miniflex diffractometer (Cr Kα radiation, λ = 2.29Å). A step scan of 0.2°, 2θ, was used for all samples with a scan speed of 1°/min. The α-$NaMnO_2$ and β-$NaMnO_2$ model compounds are air sensitive and were therefore mixed with silicon grease to prevent the breakdown of the compound during data collection. All data was collected with or converted to Cu Kα radition for clarity. Diffraction patterns were matched to the JCPDS pattern cards in the diffraction pattern library. For each sample, major peaks were selected in the XRD pattern for refinement using the cell refinement feature of the JADE XRD 6.5 pattern processing program (Materials Data, Inc.).

C. ^{23}Na MAS NMR

^{23}Na MAS NMR experiments were performed at 52.8MHz on a CMX-200 spectrometer in a field of 4.7T using a 1.8mm MAS probe at rotor spinning speeds (ν_r) of 38-40kHz.

Additional experiments were performed at 95 and 158.4MHz using fields of 8.4 and 14.1T, respectively, using a 1.3mm MAS probe, with spinning speeds of 58-60kHz. Both probes were designed and built by A. Samoson and co-workers (NICFB, Tallinn, Estonia). A rotor synchronized spin-echo pulse sequence (90°-τ-180°-τ_1-acquisition) was used with typical 90° and 180° pulses of 1.3μs and 2.6μs, respectively. Evolution periods were $\tau=n/\nu_r$, where n=2, 3, and $\tau_1=\tau-20\mu s$. A 1M solution of ^{23}NaCl was used as a reference at 0ppm.

D. Density Functional Theory Calculations (DFT)

The hybrid density functional theory (DFT) calculations utilized in the work described in this chapter employ the CRYSTAL09 all-electron linear combination of atomic orbitals code. In a similar manner as the calculations performed for hyperfine shifts in a range of Fe(III) phosphates,[33] the spin moments borne by Mn(III) and Mn(IV) sites are co-aligned in a ferromagnetic (FO) arrangement, and the isotropic ^{23}Na NMR shift, due to the Fermi-contact mechanism, is obtained as

$$\delta_{iso} = \frac{10^6 \mu_0 \mu_B \mu_N g_e g_N}{3h\nu_0} \Phi \left| \psi^{\alpha-\beta}(\mathbf{R}_N) \right|^2 (ppm)$$

where μ_0 is the vacuum permeability; μ_B, the Bohr magneton; μ_N, is the nuclear magneton; g_e, the free electron g-factor (assumed equal to 2 here); g_N, the ^{23}Na nuclear g-factor (taken as 1.478402 from Weil, Bolton and Wertz (1994)[34]); h, the Planck constant; ν_0 the ^{23}Na Larmor frequency; and $|y^{a-b}(\mathbf{R}_N)|^2$, the unpaired electron density at the position $\mathbf{R}_N$ of the nucleus of interest. Finally, Φ denotes the ferromagnetic-to-paramagnetic scaling factor derived

$$\Phi = \frac{B_0 \mu_{eff}^2}{3k_B \mu_B S_{form} (T - \Theta)}$$

where B_0 is the static magnetic induction; μ_{eff} and Θ, the experimentally-derived Curie-Weiss parameters defining the temperature-dependent paramagnetic susceptibility; T, the experimental temperature in degrees Kelvin (set at 320K throughout so as to approximate the effects of frictional heating due to MAS); k_B, the Boltzman constantl and S_{form}, the formal spin of the constituent transition metal cation [equal to 2 for Mn(III) and 3/2 for Mn(IV)].

Two levels of atom-centered Gaussian basis sets (BS) are used: less extended set (denoted BS-I) suitable for structural optimizations requiring numerous electronic minimizations,

and more extended sets (denoted BS-II) suitable for the subsequent, more intensive single point calculations of hyperfine parameters. The Be-I sets comprise (10s4p1d)/[1s2sp1d] for O, (15s7p)/[1s3p] for Na and (20s12p5d)/[1s4sp2d] for Mn and Co, all comparable with the sets used for the previously mentioned study of Fe(III) phosphates,[33] with the exception of the Na basis, which was previously applied in a study of Na_2O.[35] Values in parentheses denote the total number of Gaussian primitives of each angular type, while the values in the square brackets denote the contraction scheme. The BS-II sets comprise the modified (10s6p2d)/[6s5p2d] IGLO-III BS used previously for O,[33] a reasonably flexible and extended (11s7p)/[7s3p] TZP BS for Na (where the 3s shell was de-contracted, the most diffuse s-shell removed, and the exponents of the remaining outermost s- and p-shells increased), and (13s9p5d)/[7s5p3d] modified DZP sets for Mn and Co, similar in provision of functions to the Fe BS used in our previous study of the Fe(III) phosphates.[33]

Calculations of relevant parameters are performed in both fixed experimental (where available, denoted EXP hereafter) and fully optimized (OPT hereafter) structures. The numerical parameters controlling self-consistent field and structural optimization convergence and quality comprise integral series truncation thresholds of 10^{-7}, 10^{-7}, 10^{-7}, 10^{-7} and 10^{-14} for Coulomb overlap and penetration, exchange overlap and **g**- and **n**-series penetration, respectively, and 10-7, 0.0003 and 0.0012 AU for total energy, root mean square (RMS) force and RMS displacement respectively. Tolerances for maximum force and displacement components were set at 1.5 times the respective RMS values. The reciprocal space sampling meshes adopted for each phase vary with supercell size, convergence in magnetic energy differences and hyperfine parameters with respect to mesh density being assured in each case.

E. NMR simulations

^{23}Na NMR spectra were modeled using the program WinSolids1 by Dr. K Eichele. Values for quadrupolar coupling constant (χ), the asymmetry parameter (η), and the isotropic shift (δ_{iso}) were refined. Line broadening was also varied between Gaussian and Lorentzian to achieve the best fit.

III. Results

A. XRD

X-ray diffraction powder patterns of the synthesized model compounds were performed to determine phase purity (Figure 2.2). Basic refinement of cell parameters for each compound was performed for comparison to literature values (Table 2.1).

Table 2.1 Cell parameter refinements for model compounds obtained using JADE 6.5 pattern processing (Materials Data, Inc.).

Refined Cell Parameters for Model Compounds	
β-$NaMnO_2$ Orthorhombic a = 4.78Å b= 2.86Å c = 6.33Å Cell Volume = 86.4Å^3	α-$Na_{2/3}MnO_2$ Hexagonal a = 2.89Å c = 11.1Å Cell Volume = 80.3Å^3
α-$NaMnO_2$ Monoclinic a = 5.63Å b = 2.86Å c = 5.77Å β = 113° Cell Volume = 85.4Å^3	α-$Na_{2/3}Co_{2/3}MnO_2$ Hexagonal a = 2.83Å c = 11.1Å Cell Volume = 76.7Å^3
	β-$Na_{2/3}MnO_2$ Orthorhombic a = 2.83Å b = 5.22Å c = 11.3Å Cell Volume = 166Å^3

The model compounds were found to be phase pure, with the exception of α-$Na_{2/3}MnO_2$. Despite efforts to optimize the synthesis procedure, either small amounts of β-$Na_{2/3}MnO_2$ or an unidentified impurity were consistently found to be present (see broad peaks in the α-$Na_{2/3}MnO_2$ XRD pattern in Figure 2.2). However, the refined cell parameters for all the model compounds were found to be in good agreement with literature values,[27-30] including α-$NaMnO_2$ and β-$NaMnO_2$ in which the peaks at smaller 2θ values are partially obscured by an amorphous background due to the silicone grease used to mount and protect these air sensitive samples.

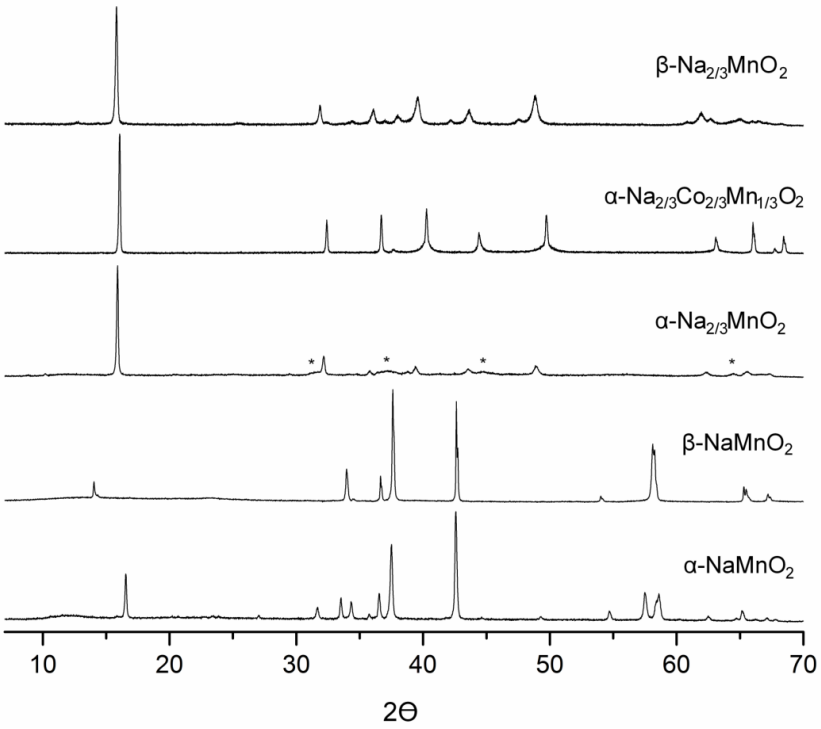

Figure 2.2 XRD patterns of the different sodium manganese oxides prepared in this study. The broad amorphous background in α-$NaMnO_2$ and β-$NaMnO_2$ powder patterns are due to silicone grease, whereas the broad peaks in α-$Na_{2/3}MnO_2$ are from an unidentified impurity (marked with '*').

B. ^{23}Na MAS NMR

Table 2.2 summarizes the ^{23}Na NMR isotropic chemical shifts observed for each model compound, along with the sodium local environments. Larger Fermi-contact shifts were observed in Mn^{4+} rich environments. The spectra for each compound will now be discussed individually for each system.

Table 2.2 Model compounds and relevant information on the local environment of each sodium site and corresponding ^{23}Na NMR isotropic chemical shift(s) observed for each compound at 8.4T.

Compound	# of Na sites		Angle of interaction	# of Na-O-$X^{3+/4+}$ interactions (x = Mn, Co)	$\%Mn^{3+}$, $\%Mn^{4+}$	Observed isotropic shift(s) in PPM
α-$NaMnO_2$	1		168-170° 90°	6 (2 d_z^2) 12 (4 d_z^2, 4 $d_{x^2-y^2}$)	100% Mn^{3+}	725
β-$NaMnO_2$	1		180° 90°	4 12 (4 d_z^2, 4 $d_{x^2-y^2}$)	100% Mn^{3+}	280, 475
α-$Na_{2/3}MnO_2$	2	Na #1	131° 77°	12 6	66.67% Mn^{3+}, 33.33% Mn^{4+}	1521, 1637
		Na #2	161° 94°	6 12		
α-$Na_{2/3}Co_{2/3}Mn_{1/3}O_2$	2	Na #1	131° 77°	12 6	100% Mn^{4+}	695
		Na #2	161° 94°	6 12		
β-$Na_{2/3}MnO_2$	2	Na #1	160-166° 89-97°	6 12	66.67% Mn^{3+}, 33.33% Mn^{4+}	794, 1112
		Na #2	130-140° 70-80°	12 6		

IV. Discussion

A. β-$NaMnO_2$

The ^{23}Na MAS NMR spectra of β-$NaMnO_2$ at 4.7 and 8.4 T show two isotropic resonances, indicating two distinct sodium environments (Figure 2.3 a. and b.). The isotropic resonance, or centerband, is due primarily to the 1/2↔-1/2 transition, which is only affected to second-order by the quadrupolar interaction. The spinning sidebands present in both spectra (marked with asterisks) are primarily due to the ±3/2↔±1/2 satellite transitions, which are affected to first and second order by the quadrupolar interaction. The size of the second-order quadrupolar interaction, reduced at higher field strengths, explains the simpler lineshapes observed in Figure 2.3 b. Integration of the intensity of the isotropic resonances provides an approximate estimate for the relative quantities of the two sodium environments of 1:2. Intensity from the central transition may be present in the spinning sidebands, particularly in paramagnetic systems where the dipolar coupling to the unpaired electrons on the manganese ions can result in large contributions to the spinning sidebands. It is often difficult to separate central transition intensity from satellite transition contributions without a full simulation of the entire spectrum,

especially in systems with moderate quadrupole interactions. However, even the inclusion of the intensities of the +/- 1 and 2 sidebands does not change this intensity ratio noticeably.

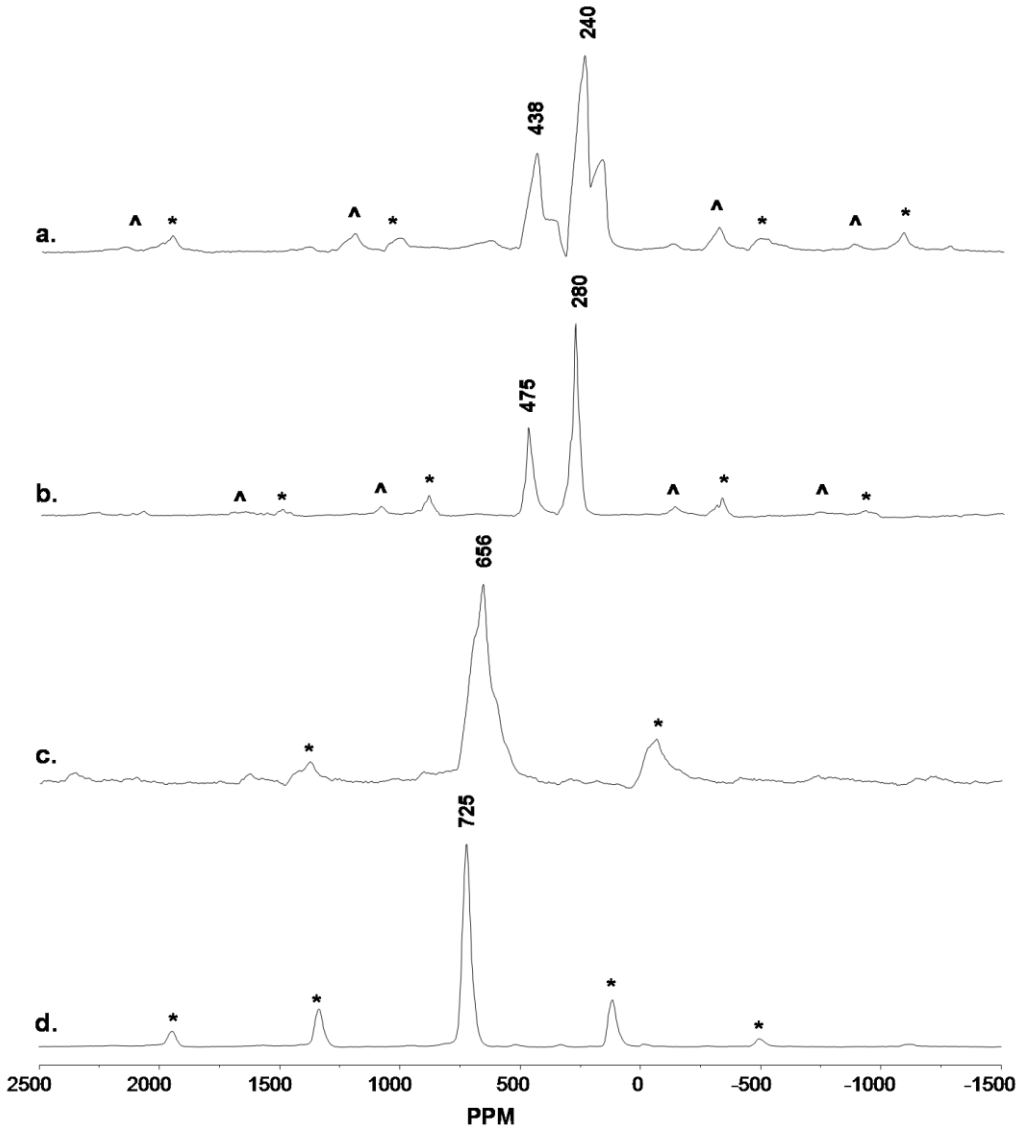

Figure 2.3 ^{23}Na NMR spectra of β-$NaMnO_2$ (a) and (b), and α-$NaMnO_2$ (c) and (d). (a) and (c) acquired at 4.7 T using a spinning speed of 40kHz. (b) and (d) acquired at 8.4 T using a spinning speed of 58kHz. For all spectra, spinning sidebands are marked with '*' and '^'.

The single crystal refinement of β-$NaMnO_2$ indicates that there is a single sodium crystallographic site, in clear contradiction with the ^{23}Na NMR results.[27] The intensity of the weaker peak appears to be too large to originate from the presence of a paramagnetic impurity, the XRD powder pattern showing no clear evidence for the presence of a significant concentration of an impurity phase (β-$NaMnO_2$ in Figure 2.2). The ^{23}Na NMR results, therefore,

suggest that an additional local sodium environment may be present in the structure, possibly due to a distortion of the crystallographic sodium environment to accommodate the larger sodium cation. While previous ^{6}Li NMR studies of the lithium form of this material, β-$LiMnO_2$, reported only a single Li environment,[36] the two observed resonances in the ^{23}Na spectra of the β-$NaMnO_2$ form may reflect possible distortions of the sodium environment to accommodate the larger ionic radius of sodium in comparison to that of lithium. The possible distortion could also be electronic or magnetic in nature. Although the Néel temperature of this material is not known, the sharp ^{23}Na signals strongly suggest that the spectra are acquired in the paramagnetic regime, and thus this does not appear to be source of the additional resonances. Hybrid density functional theory (DFT) calculations were applied to estimate the per Mn^{3+}-O-Na contact contribution to the overall hyperfine shift using an optimized β-$NaMnO_2$ crystal structure; these calculations produced δ_{iso} values of 482.1ppm for the F_o = 20% and 52.1ppm for the F_o = 35% hybrid Hamiltonians.[37] Since the actual δ_{iso} value will fall somewhere in between these two calculations, the intense peak in the experimental spectrum at 280ppm was identified as the environment relevant to the β-$NaMnO_2$ material. However, as of yet, these calculations are unable to provide any further explanation for the presence of the second, less intense sodium environment at 475ppm.

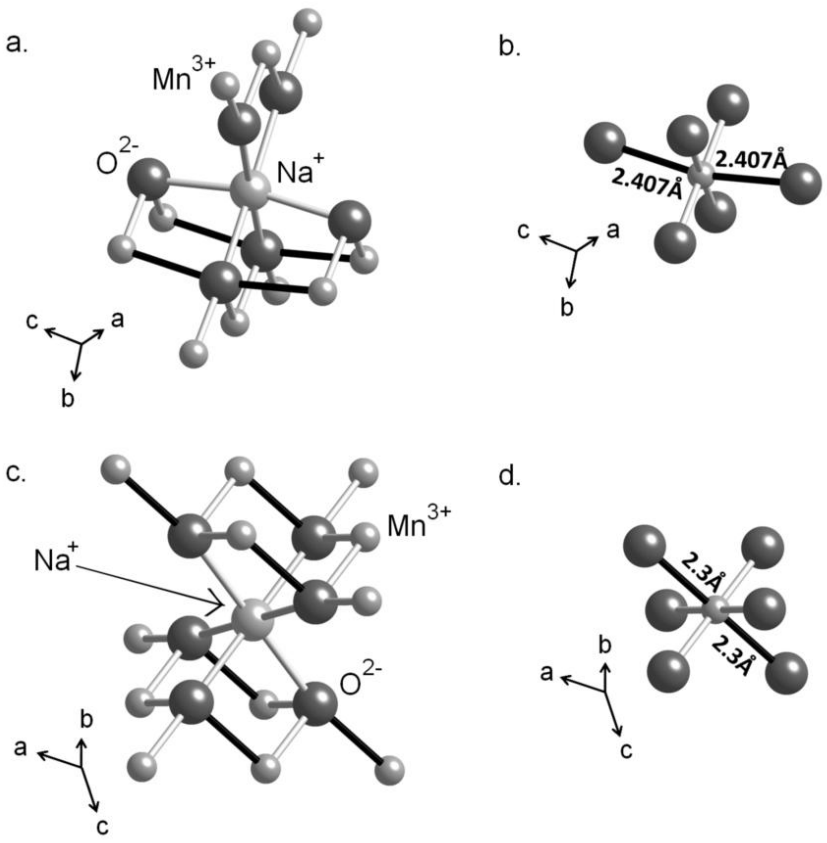

Figure 2.4 The local environments of sodium and manganese in the crystal structure of β-$NaMnO_2$ (5 (a) and (b)) and α-$NaMnO_2$ (5 (c) and (d)). (a) Local coordination environment of Na^+ to six oxygen atoms giving rise to a maximum of sixteen Na^+-O-Mn^{3+} interactions. (b) the local environment of Mn^{3+} illustrating Jahn-Teller distortions present in β-$NaMnO_2$. Black bonds between oxygens and manganese in this and in other relevant structural figures indicate the longer Mn-O bonds caused by the Jahn-Teller distortions. (c) the local coordination environment of Na^+ to six oxygens giving rise to a maximum of eighteen Na^+-O-Mn^{3+} interactions. (d) The local environment of Mn^{3+} illustrating Jahn-Teller distortions present in α-$NaMnO_2$.

The effect of the different types of Na-O-Mn interactions on the overall shift can be analyzed using the reported β-$NaMnO_2$ crystal structure. Na^+ is surrounded by 10 Mn^{3+} ions leading to sixteen Na^+-O-Mn^{3+} interactions, twelve at *ca.* 90º and four at 180º (Table 2.2; Figure 2.4 a.). The nature of the Jahn-Teller distortion indicates that the d_z^2 orbital must be partially occupied and oriented along the direction of the elongated Mn-O bonds, while the unoccupied $d_{x^2-y^2}$ manganese orbitals are oriented along the direction of the four shortened Mn-O bonds. The aforementioned DFT calculations indicate the four 180° Na^+-O-Mn^{3+} interactions involve the $d_{x^2-y^2}$ orbitals produce negative hyperfine shift contributions to the overall shift of this sodium

environment.[37] However, significant positive contributions were determined to result from some of the twelve 90° Na^{+}-O-Mn^{3+} interactions (some interaction pathways were found to give small negative contributions) that produce a small, overall positive hyperfine shift. The dependence of the size and sign of transferred spin density upon the orientation of d_z^2 orbitals of the paramagnet with respect to the resonating nucleus has been observed previously in NMR studies of lithium forms of layered manganese oxides, including α- and β-$LiMnO_2$.[36] While the magnitudes of path dependent shift contributions vary, the trends are observed to be similar.

B. α-$NaMnO_2$

The ^{23}Na MAS NMR spectrum of this layered material, at a field of 4.7 T (Figure 2.3 c.), consists of a single resonance, consistent with the presence of one sodium environment.[28] The complex line shape of this isotropic resonance hints at the existence of second order line shape effects, which are largely absent in the spectrum acquired at a higher field of 8.4T (Figure 2.3 d.), where the peak is more symmetric. The shift of the isotropic resonance of this material, at 725ppm, is significantly greater than the shift observed for β-$NaMnO_2$ (280ppm) which may be explained, in part, by a larger number of Na^{+}-O-Mn^{3+} interactions (Table 2.2), as well as the difference in orientation of bonding interactions with the first coordination shell paramagnets.

The sodium ions in α-$NaMnO_2$ are surrounded by 12 severely Jahn-Teller distorted Mn^{3+} ions (Figure 2.4 d.), leading to a total of 18 Na^{+}-O-Mn^{3+} interactions (Figure 2.4 c., four *ca* 180° interactions in which the empty manganese $d_{x^2-y^2}$ orbitals were found via DFT calculations to contribute a negative shift, twelve 90° interactions with manganese t_{2g} orbitals producing positive shift contributions, and an additional two *ca.* 180° interactions with the half filled manganese d_z^2 orbitals (which are not present for β-$NaMnO_2$), that also contribute positive shift to the overall observed isotropic chemical shift. DFT calculations, summing all calculated contributions from each of the different Na^{+}-O-Mn^{3+} interactions in the α-$NaMnO_2$ sodium local environment, produced an overall hyperfine shift that was in good agreement with the observed shift in the corresponding ^{23}Na NMR spectra, with δ_{iso} values of 816.7ppm for F_0 = 20% and 487.7ppm for F_0 = 35% hybrid Hamiltonians.[37]

C. α-$Na_{2/3}MnO_2$ and α-$Na_{2/3}Co_{2/3}Mn_{1/3}O_2$

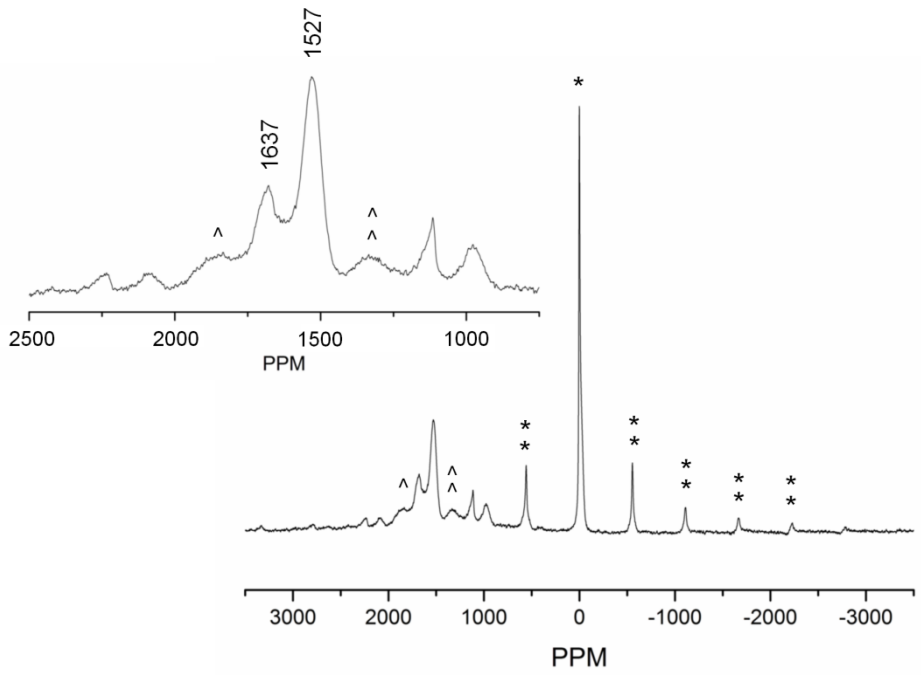

Figure 2.5 ^{23}Na NMR spectrum of α-$Na_{2/3}MnO_2$. The diamagnetic impurity is labeled with '*' and spinning sideband manifold of the impurity is labeled with '**'. The inset is a zoom of the region of interest for the paramagnetic sodium of the α-P2-$Na_{2/3}MnO_2$ material. A third paramagnetic environment is labeled with '^' and spinning sidebands of this environment with '^^'. This environment is a possible third, more Mn^{4+} rich local sodium environment within the α-$Na_{2/3}MnO_2$ structure.

The NMR spectrum of α-$Na_{2/3}MnO_2$ contains two intense hyperfine shifted sodium environments at 1527 and 1637ppm, consistent with the presence of two crystallographic sites in this structure (Figure 2.5). A third, broader paramagnetic environment isolated at 1680ppm may be a third, Mn^{4+} rich environment in the α-$Na_{2/3}MnO_2$ structure. The narrow resonance at 0.7ppm is assigned to a diamagnetic impurity, such as unreacted Na_2CO_3.

Both sodium sites from the crystallographic structure have a total of 18 Na-O-$Mn^{3+/4+}$ interactions. The first sodium site, Na1, is face sharing with layer $Mn^{3+/4+}$ octahedra above and below and has twelve 131° Na^+-O-$Mn^{3+/4+}$ interactions and six 77° interactions, while the second sodium site, Na2, is edge sharing with layer $Mn^{3+/4+}$ above and below, has six 161° Na^+-O-$Mn^{3+/4+}$ interactions and twelve 94° interactions (Table 2.2 and Figure 2.6 a. and b.).[29, 31]

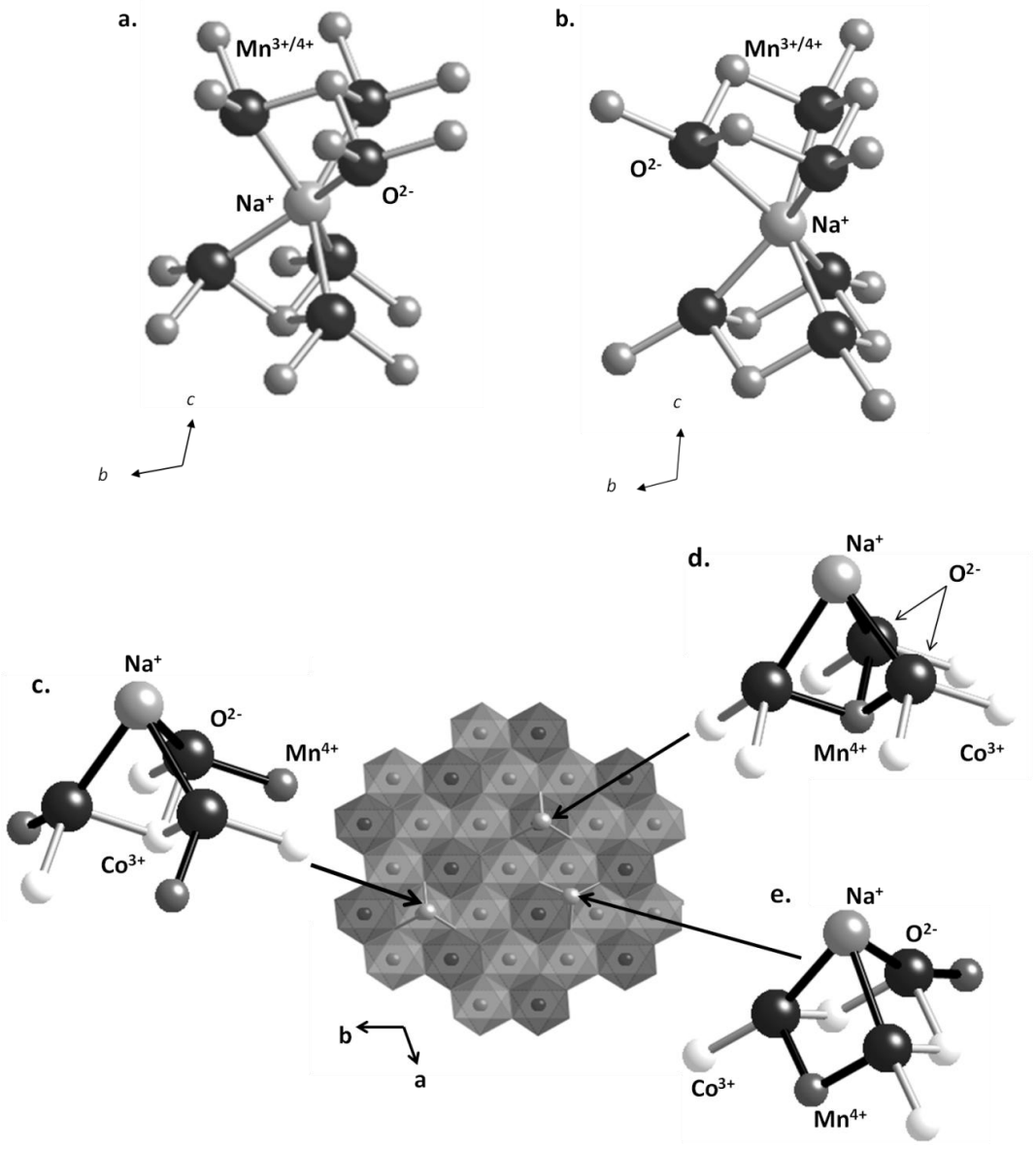

Figure 2.6 Structure of α-$Na_{2/3}MnO_2$. (a) Local coordination of Na1 prismatically coordinated to six layer oxygens generating 18 Na^+-O-$Mn^{3+/4+}$ interactions. (b) Local coordination environment of Na2, also prismatically coordinated to six layer oxygens with a total of 18 Na^+-O-$Mn^{3+/4+}$ interactions. 2.6(c)-(e) Possible sodium environments generated by clustered honeycomb ordering of layer Mn^{4+} (dark grey octahedra in the depicted layer) in α-$Na_{2/3}Co_{2/3}Mn_{1/3}O_2$ with respect to one layer. (c) a sodium Na1 cation positioned above a layer Co^{3+} layer octahedron (light grey octahedra in the depicted layer) produces three 131° Na^+-O-Mn^{4+} bonding angles. (d) a sodium Na1 cation positioned above a layer Mn^{4+} octahedron produces three 77° Na^+-O-Mn^{4+} bonding angles (e) a sodium Na2 cation at a vertex of two Co^{3+} and one Mn^{4+} octahedra produces two 94° and one 162° Na^+-O-Mn^{4+} bonding angles.

The α-$Na_{2/3}MnO_2$ structure is still poorly described by refinements, mostly hindered by the difficulty in producing phase pure material. However, drawing from refinements of similar structures such as the β form of $Na_{2/3}MnO_2$, as well as Co and Ni doped structural equivalents, the sodium site refinements consistently indicate the Na1 site to have a smaller occupancy than the Na2 site.[30] If it is reasoned that the Na1 sodium site is face sharing with layer Mn octahedra above and below and is consequently spatially less ideal for the ionic radius of the interlayer Na^+ ions, the relative occupancies of the sodium sites of α-$Na_{2/3}MnO_2$ are expected to be similar. Therefore, the less intense 1637ppm peak is assigned to the Na1 sodium environment and the more intense 1521ppm peak is assigned to the Na2 sodium environment.

Since α-$Na_{2/3}MnO_2$ contains both Mn^{3+} and Mn^{4+} ions, which give rise to different ^{23}Na NMR shifts, and no ordering pattern can be detected by XRD, additional information about magnitudes of shifts associated with Mn^{4+} was obtained from the spectrum of α-$Na_{2/3}Co_{2/3}Mn_{1/3}O_2$. This phase contains only Mn^{4+} and the diamagnetic ion Co^{3+}. Hence, the hyperfine shifted sodium environments in Figure 2.7 a. and b. are entirely due to the contributions of unpaired electron spin density transferred from Mn^{4+} to the corresponding sodium nuclei.

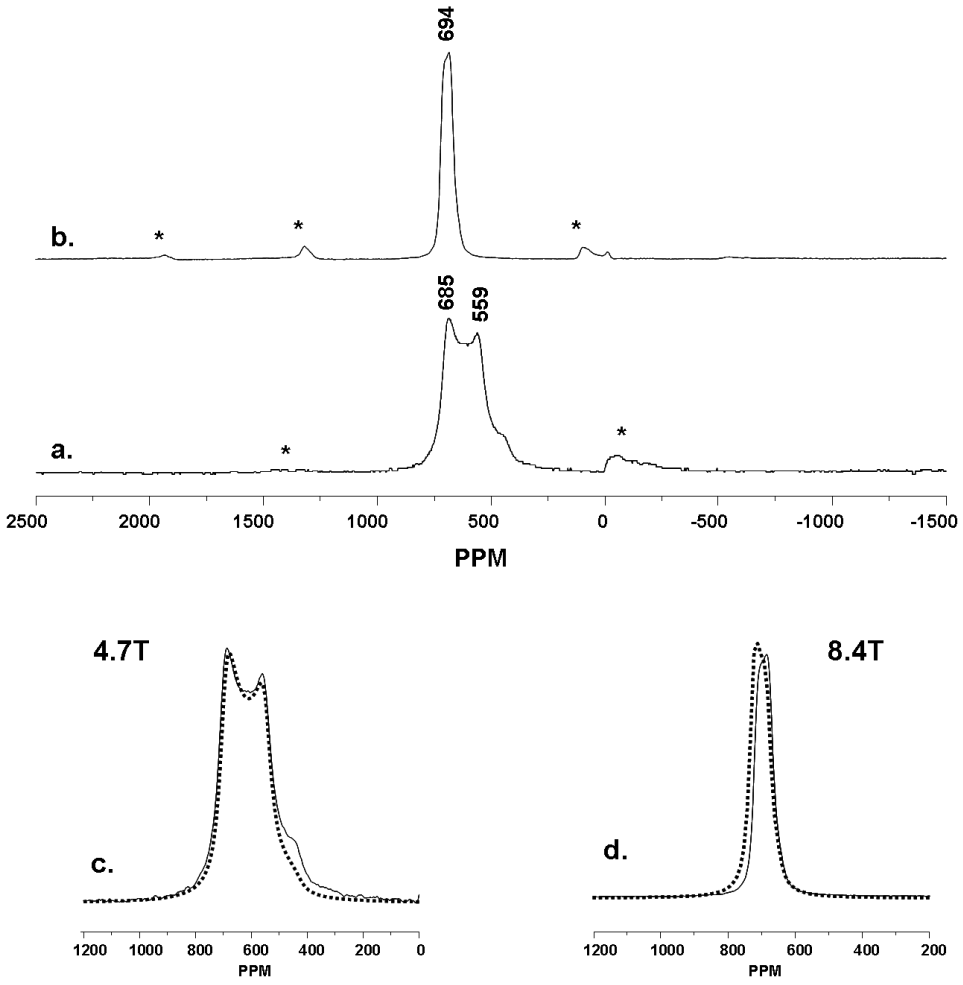

Figure 2.7 ^{23}Na NMR spectra of α-$Na_{2/3}Co_{2/3}Mn_{1/3}O_2$. (a) at 4.7T at a spinning speed of 38kHz. (b) 8.4T at spinning speed of 58kHz. For both spectra, spinning sidebands indicated by '*'. Simulations of ^{23}Na NMR spectra of α-$Na_{2/3}Co_{2/3}Mn_{1/3}O_2$ at 4.7T and 8.4T using one sodium site ((c) and (d)). Refinements produced values for χ = 3.75 + 0.1MHz, η = 0.09 + 0.04 and δ = 742 + 9ppm using 2500Hz Lorentzian line broadening.

While structural refinements indicate the existence two crystallographically unique sodium sites, the ^{23}Na NMR spectrum at 4.7 T (Figure 2.7 a.) shows discontinuities at 559 and 685ppm, which appear to be due to the second order line shape from a single sodium site. A more symmetric lineshape with a shift of about 695 ppm is and a reduced line width is observed at a field strength of 8.4T, (Figure 2.7 b.) consistent with second-order broadening of a single site. Spectral simulations were attempted using one sodium site (Figure 2.7 c. and d.). The discrepancy in shift between the 8.4T spectrum and the simulation is attributed to the sensitivity of ^{23}Na shifts to temperature (frictional heating varies with spinning speed) which the simulation

software does not account for. While both spectra were taken at room temperature, frictional heating from spinning at 58kHz is significantly greater for the 8.4T spectrum compared to the 4.7T spectrum which was collected at a spinning speed of only 38kHz. Simulations using two non-equivalent sodium sites were investigated as well but are omitted as they produced no significant improvement in fits to the spectral data. As a result, resolution of the number of sodium sites in α-$Na_{2/3}Co_{2/3}Mn_{1/3}O_2$ was inconclusive. As in the α-$Na_{2/3}MnO_2$ structure, the local structure of the two crystallographic sodium sites are composed of the same number of Na-O-Mn interactions, but differ slightly in bond angles (see Table 2.2). Ordering of Co^{3+} ions in the manganate layer could produce sodium environments which have similar shifts such that they cannot be resolved by MAS NMR.

The simplicity of the ^{23}Na NMR spectra of this compound, suggests a relatively straightforward ordering of layer Co^{3+} and Mn^{4+} ions in the local environment of sodium. The sodium may order preferentially to one of the crystallographic sites with respect to ordering of Co^{3+} ions in the manganate layers resulting in a single sodium environment. However, previous work with these layered manganese bronzes, has not found any evidence of for Co^{3+} ions ordering within the layers.[29, 38] In the absence of long range ordering, a clustered short range Co^{3+} ordering may be possible. If we assume the 2/3 Co^{3+} in the metal oxide layers will order in a similar manner as the Mn^{3+} and Mn^{4+} is generally accepted to order within the birnessite manganese oxide layers, two adjacent rows of Co^{3+} would generate diamagnetic sodium environments. Since no diamagnetic signal is observed in the ^{23}Na NMR spectra of this compound, it is unlikely that this ordering scheme occurs, even on a short range scale.

A likely ordering scheme that is favored in this triangular lattice is a honeycombed ordering of the layer Co^{3+}. Examining the possible sodium environments with respect to a single layer of honeycomb ordered Co^{3+} clustering, there are three general positions in which unique environments could be generated – two with the Na1 site and one with the Na2 site (Figure 2.6 c. to e.). However, it is likely that the configuration shown in 2.6 c. and d. is less stable than that of 2.6 e. due to the higher charge of the Mn^{4+} ion, and results in a preferential occupation of the (e) configuration. Structural refinements of $Na_{2/3}CoO_2$, one of the end members of the $Na_{2/3}Co_xMn_{1-x}O_2$ bronze series, yielded significantly lower occupancies for the face sharing Na1 site positioned directly over the layer transition metals (Figure 2.6 a.) compared to the refined occupancy of the edge sharing Na2 site (Figure 2.6 b.).[30] Higher occupancies for the Na2 site

(*ca.* 1/2) compared to the Na1 site (*ca.* 1/5) were reported by Stoyanova *et al*. in a refinement of the orthorhombically distorted β-$Na_{2/3}MnO_2$ phase as well.[39] This indicates preferential sodium occupancy of specific sites with respect to the transition metal layer in this class of materials in general, and is a phenomenon that may also occur in the case of α-$Na_{2/3}Co_{2/3}Mn_{1/3}O_2$.

The number of manganese contacts for each of the three environments (again, with reference to a single layer) are the same, but differ in bonding angles: one environment with three 131° Na^+-O-Mn^{4+} bonding angles (Figure 2.6 c.), one with three 77° Na^+-O-Mn^{4+} bonding angles (Figure 2.6 d.) and one environment with two 94° and one 162° Na^+-O-Mn^{4+} bonding angles (Figure 2.6 e.). If registry between the layers with respect to clustered Co^{3+} ordering is assumed, the number local environments present would be the same, while the number of the Na^+-O-Mn^{4+} interactions would double. In the absence of such registry, a greater number of environments could be present, though such a spread of environments would likely produce a much broader ^{23}Na NMR spectrum than the one observed.

The application of hybrid DFT calculations determined optimized structures for local sodium environments with a variety of different Mn and Co configurations for α-$Na_{2/3}Co_{2/3}Mn_{1/3}O_2$ yielding numerous local environments with similar ground state energy configurations, and very similar δ_{iso} values for F_o = 20% and F_0 = 35% hybrid Hamiltonians.[37] While there is no apparent explanation for a single, preferred local sodium configuration based on these results, it is speculated that the sodium cations in this material are highly mobile at room temperature (or near room temperature) in the interlayers and exchange frequently between sodium sites, giving rise to the broadened peak observed in the ^{23}Na NMR spectrum of α-$Na_{2/3}Co_{2/3}Mn_{1/3}O_2$.

D. β-$Na_{2/3}MnO_2$

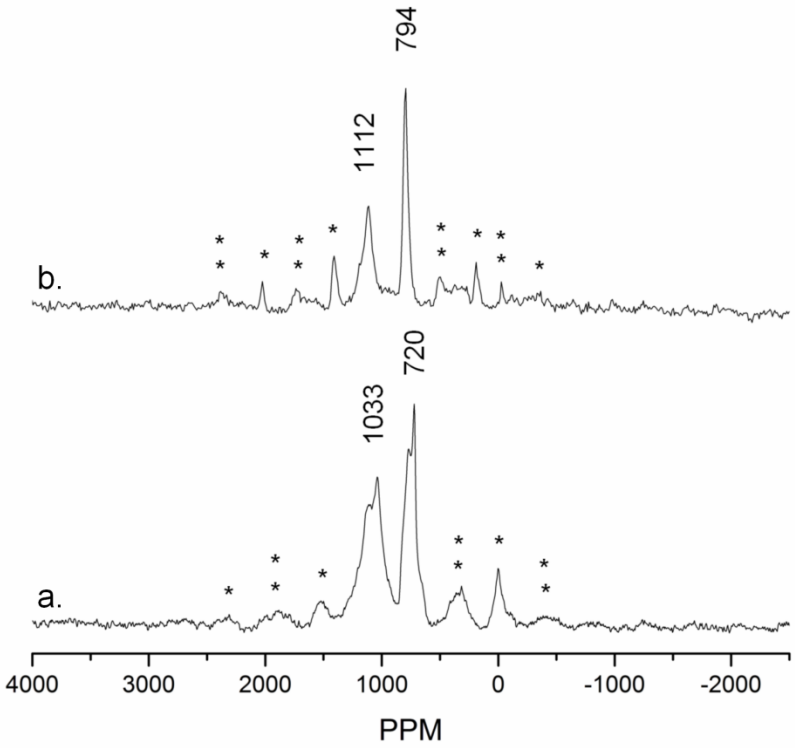

Figure 2.8 ^{23}Na NMR spectra of β-$Na_{2/3}MnO_2$ model compound. (a) spectrum taken at 4.7T at a spinning speed of 40kHz. (b) spectrum taken at 8.4T at a spinning speed of 58kHz. Spinning side bands are marked with '*'.

The ^{23}Na spectrum of the orthorhombically distorted material, β-$Na_{2/3}MnO_2$, at a 4.7 T field strength shows multiple sodium peaks and discontinuities, a simpler spectrum being observed at 8.4 T with two resonances at 794 and 1112ppm (Figure 2.8 a. and b.), consistent with the two crystallographic sites present in this material. Again both sites contain eighteen Na^+-O-$Mn^{3+/4+}$ interactions, the Jahn-Teller distortion present in this structure resulting in slight changes in the Na-O-Mn bond angles, as compared to those found in the α phase (Figure 2.9 a. and b.; Table 2.2).[30] Comparing the ^{23}Na chemical shifts for β-$Na_{2/3}MnO_2$ with those of α-$Na_{2/3}MnO_2$, there is a significant difference in shift, despite only a slight distortion in the β form compared to the α form. This may in part be due to slight differences in the average oxidation state (AOS) of the two materials, the AOS of the manganese in the α-form being slightly greater than that found in the β-form, the lower AOS being sufficient to cause a Jahn-Teller distortion in the β-form.[30]

The observation of smaller shifts in JT-distorted compounds has been observed before in lithium manganates, where it was explained by DFT calculations by Carlier et al. to be the result of reduced orbital overlap when the e_g orbital is occupied by an unpaired electron and elongates to eliminate degeneracy.[25]

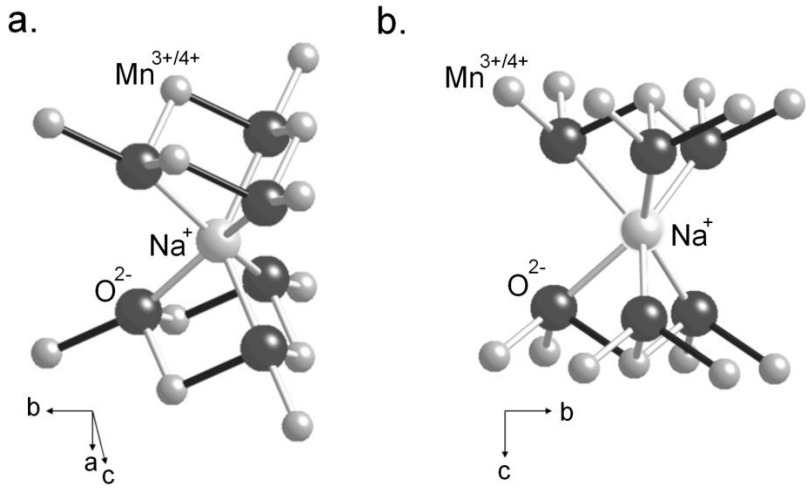

Figure 2.9 Local environments of the two crystallographically unique sodium sites in the β-$Na_{2/3}MnO_2$ model compound. Black bonds indicate Jahn-Teller distorted Mn-O bonds (a) the local coordination environment of Na1 to six oxygens giving rise to eighteen Na^+-O-$Mn^{3+/4+}$ interactions. (b) the local coordination environment of Na2 to six layer oxygens giving rise to eighteen Na^+-O-$Mn^{3+/4+}$ interactions.

The resonances may be assigned to specific local environments by using the same reasoning applied to the spectrum of α-$Na_{2/3}MnO_2$. Since the Na1 sodium site has lower occupancy,[39] the less intense resonance at 1112ppm is assigned to this sodium environment, and the Na2 is assigned to the significantly more intense resonance at 794ppm. It is interesting to note the refinement of β-$Na_{2/3}MnO_2$ by Stoyanova *et al*. reports shorter Na-Mn distances for the Na1 site;[39] this may suggest more orbital overlap in the Na-O-Mn contacts for this sodium environment, which would help explain the larger observed hyperfine shift for this environment.

V. Conclusions

The spectra of Mn^{3+} sodium manganese oxides, β- and α-$NaMnO_2$, highlight the impact of Jahn-Teller distortions and the orientation of the d_z^2 orbitals relative to the bonding angles of the Na^+-O-Mn^{3+} interactions on the observed hyperfine shifts. Contributions from DFT

calculations indicate the shift at 280ppm in the spectrum of β-$NaMnO_2$ corresponds to the sodium environment in the refined crystal structure from literature. Comparison of the spectra of β-$Na_{2/3}MnO_2$ with that of α-$Na_{2/3}MnO_2$ also highlight how Jahn-Teller distortions (arising from a slight lowering of the AOS of layer manganese) result in notably smaller hyperfine shifts despite very similar sodium environments in the two compounds.

While an estimate for the shift per Na^+-O-$Mn^{3+/4+}$ contact cannot necessarily be determined from the ^{23}Na NMR spectra of the Mn^{4+} in mixed valence manganese oxides, the spectra presented in this chapter clearly demonstrate larger shifts are seen for Na^+-O-Mn^{4+} contacts than Na^+-O-Mn^{3+} contacts. For example, the shifts of α-$Na_{2/3}MnO_2$ are three to five times greater than those observed for the α-$NaMnO_2$ and β-$NaMnO_2$ compounds despite having nearly the same number of Na^+-O-Mn contacts (see Table 2.2); α-$Na_{2/3}Co_{2/3}Mn_{1/3}O_2$ has significantly fewer Na^+-O-Mn^{4+} contacts than the number of Na^+-O-Mn^{3+} contacts in α-$NaMnO_2$, yet similar paramagnetic shifts are observed (see Table 2.2). DFT calculations could not provide an explanation for the presence of only one sodium environment in the ^{23}Na NMR spectra of α-$Na_{2/3}Co_{2/3}Mn_{1/3}O_2$, however, there are implications that sodium may be very mobile at room temperature in this compound and there is considerable exchange between sites.

VI. References

1. O'Reilly, S. E., Hochella, M. F., *Geochim. Cosmochim. Acta* **67**, 4471-4487 (2003).

2. Kuma, K., Usui, A., Paplawsky, W., Gedulin, B., Arrhenius, G., *Mineral Mag* **58**, 425-447 (1994).

3. Mckenzie, R. M., *Geochim. Cosmochim. Acta* **43**, 1855-1857 (1979).

4. Mckenzie, R. M., *Aust. J. Soil Res.* **18**, 61-73 (1980).

5. Post, J. E., Veblen, D. R., *Am. Mineral.* **75**, 477-489 (1990).

6. Drits, V. A., Silvester, E., Gorshkov, A. I., Manceau, A., *Am. Mineral.* **82**, 946-961 (1997).

7. Silvester, E., Manceau, A., Drits, V. A., *Am. Mineral.* **82**, 962-978 (1997).

8. Lanson, B., Drits, V. A., Gaillot, A. C., Silvester, E., Plancon, A., Manceau, A., *Am. Mineral.* **87**, 1631-1645 (2002).

9. Toner, B., Manceau, A., Webb, S. M., Sposito, G., *Geochim. Cosmochim. Acta* **70**, 27-43 (2006).

10. Post, J. E., *P Natl Acad Sci USA* **96**, 3447-3454 (1999).

11. McKeown, D. A., Post, J. E., *Am. Mineral.* **86**, 701-713 (2001).

12. Glasby, G. P., Ed., *Marine Manganese Deposits*, vol. 15 (Elsevier Scientific Publishing Company, Amsterdam, ed. 1, 1977), vol. 15, 1, pp. 523.

13. Yi, T. F., Zhu, Y. R., Zhu, X. D., Shu, J., Yue, C. B., Zhou, A. N., *Ionics* **15**, 779-784 (2009).

14. Whitacre, J. F., Tevar, A., Sharma, S., *Electrochem. Commun.* **12**, 463-466 (2010).

15. Qu, Q. T., Shi, Y., Tian, S., Chen, Y.H., Wu, Y.P., Holze, R. , *J. Power Sources* **194**, 1222-1225 (2009).

16. Grey, C. P., Lee, Y. J., *Solid State Sci* **5**, 883-894 (2003).

17. Grey, C. P., Dupre, N., *Chem. Rev.* **104**, 4493-4512 (2004).

18. Tevar, A. D., Whitacre, J. F., *J. Electrochem. Soc.* **157**, A870-A875 (2010).

19. Caballero, A., Hernan, L., Morales, J., Sanchez, L., Santos Pena, J., Aranda, M. A. G., *J. Mater. Chem.* **12**, 1142-1147 (2002).

20. Tsuda, M., Arai, H. Sakurai, Y., *J. Power Sources* **110**, 52-56 (2002).

21. Bach, S., Pereira-Ramos, J. P., Cachet, C., Bode, M., Tse Yu, L. , *Electrochim. Acta* **40**, 785-789 (1995).

22. Bach, S., Pereira-Ramos, J. P., Baffier, N., *J. Electrochem. Soc.* **143**, 3429-3434 (1996).

23. Mendiboure, A., Delmas, C., Hagenmuller, P. , *J. Solid State Chem.* **57**, 323-331 (1985).

24. Cheetham, A. K., Dobson, C. M., Grey, C. P., Jakeman, R. J. B., *Nature* **328**, 706-707 (1987).

25. Carlier, D., Menetrier, M., Grey, C. P., Delmas, C., Ceder, G., *Phys. Rev. B* **67**, - (2003).

26. Carlier, D., Blangero, M., Menetrier, M., Pollet, M., Doumerc, J.P., Delmas, C., *Inorg. Chem.* **48**, 7018-7052 (2009).

27. Hoppe, V. R., Brachtel, G., Jansen, M., *Z. Anorg. Allg. Chem.* **417**, 1 (1975).

28. Parant, J. P., Olazcuaga, R., Devalette, M., Fouassier, C., Hagenmuller, P., *J. Solid State Chem.* **3**, 1-11 (1971).

29. Lu, Z., Donaberger, R. A. , Dahn, J. R. , *Chem. Mater.* **12**, 3583-3590 (2000).

30. Paulsen, J. M., Dahn, J. R., *Solid State Ionics* **126**, 3-24 (1999).

31. Dolle, M., Patoux, S., Doeff, M. M., *Chem. Mater.* **17**, 1044-1054 (2005).

32. Bach, S., Henry, M., Baffier, N., Livage, J., *J. Solid State Chem.* **88**, 325-333 (1990).

33. Kim, J., Middlemiss, D. S., Chernova, N. A., Zhu, B. Y. X., Masquelier, C., Grey, C. P., *J. Am. Chem. Soc.* **132**, 16825-16840 (2010).

34. Weil, J. A., Bolton, J. R., Wertz, J. E., *Electron Paramagnetic Resonance: Elementary Theory and Practical Applications*. (John Wiley & Sons Inc., New York, ed. 1st, 1994), pp. 592.

35. Dovesi, R., Roetti, C., Freyriafava, C., Prencipe, M., Saunders, V. R., *Chem. Phys.* **156**, 11-19 (1991).

36. Lee, Y. J., Grey, C. P., *Chem. Mater.* **12**, 3871-3878 (2000).

37. Aldi, K. A., Middlemiss, D. S., Cabana, J., Sideris, P. J., Grey, C. P., (Submitted for Publication).

38. Tournadre, F., Croguennec, L., Saadoune, I., Weill, F., Shao-Horn, Y., Willmann, P., Delmas, C., *Chem. Mater.* **16**, 1411-1417 (2004).

39. Stoyanova, R., Carlier, D., Sendova-Vassileva, M., Yoncheva, M, Zhecheva, E., Nihtianova, D., Delmas, C., *J. Solid State Chem.* **183**, 1372-1279 (2010).

Chapter 3

^{23}Na NMR Spectroscopy Investigation of Cation Ordering in Triclinic Sodium Birnessite and Cation Locations in Tunnel Structured Todorokite and Cryptomelane

Birnessite is a widespread, naturally occurring layered manganese oxide that exerts significant influence over the geochemical cycling of environmentally relevant cations due to its high interlayer adsorption capacity. Triclinic sodium birnessite was used as a synthetic analogue to gain a better understanding of the nature of cation adsorption in this important phyllomanganate. Drawing from previous work correlating observed ^{23}Na NMR shifts in manganese oxides with local environment and Mn oxidation state, the ^{23}Na NMR spectra of metastable buserite and two birnessite samples, NaBi-H-I and NaBi-II were analyzed to determine the nature of the bound interlayer sodium ions in these materials. The small ^{23}Na chemical shift of buserite shows that its interlayer sodium is fully hydrated. X-ray diffraction indicates that NaBi-H-I is a disordered birnessite while NaBi-II is highly crystalline. High field (14.1T) fast MAS NMR spectra of NaBi-H-I and NaBi-II supports these observations, resolving multiple sodium environments for NaBi-H-I and only two sodium environments for NaBi-II. The observed hyperfine shifts were less than expected for sodium environments with manganate layers composed of 2/3 Mn^{4+} and 1/3 Mn^{3+} ions, and the ^{23}Na lineshapes indicated that the Na^{+} ions are in distorted environments. Both these factors suggest that the sodium ions are offset in the interlayers toward a single oxide layer and located near Mn^{3+}-rich environments within the layer. Todorokite and cryptomelane are tunnel structured manganese oxides synthesized from a birnessite precursor. Synthetic samples of these minerals were prepared and ^{23}Na NMR was used to compare sodium cation locations within the tunnels in synthetic and natural materials.

This chapter is adapted from a journal article submitted for publication in the journal, American Mineralogist.

I. Introduction

A. Birnessite

As described in the first chapter, manganese oxides, particularly layered materials such as birnessite, play a crucial role in the geochemical cycling of environmentally relevant cations (*i.e.* heavy metals such as Pb, Cd, Ni, Co, Zn). [1-11] Studies have indicated phyllomanganates, *i.e.* layered Mn oxides, are the dominant type of manganese oxide in the environment,[9, 12-14] and that birnessite is the most common form of naturally occurring layered manganese oxides.[11] This chapter focuses on the triclinic form of birnessite, composed of stacked sheets of edge-sharing manganese (IV) octahedra containing a negative layer charge arising from the presence of layer manganese (III) octahedra. To offset the negative layer charge, cations and/or protons are sorbed within the interlayers (See Chapter 1, Figure 1.4 b.).

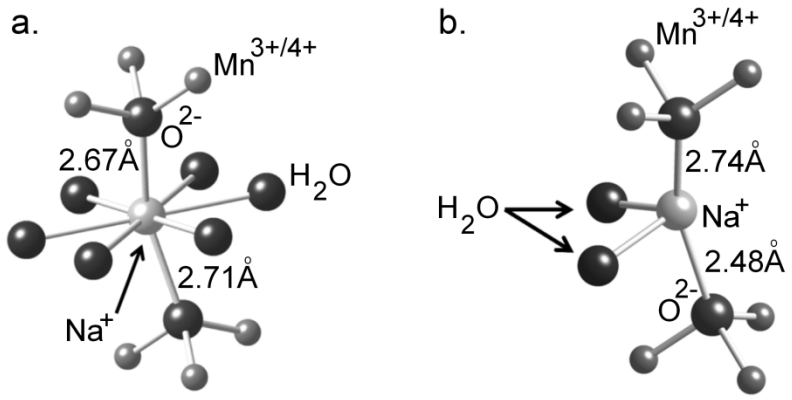

Figure 3.1 (a) Local sodium environment as proposed by Post et al.[15] Sodium is coordinated to six interlayer waters at distances of 2.85 to 2.95Å and two layer oxygens at 2.71 and 2.67Å. There are six Na^{+}-O-$Mn^{3+/4+}$ interactions resulting from coordination to two layer oxygens above and below the sodium site. (b) Local sodium environment as proposed by Lanson et al.[16] Sodium is coordinated to two layer oxygens at 2.48 and 2.74Å and two interlayer water molecules at 2.61 and 2.74Å.

Natural samples of birnessite generally occur as poorly crystallized and fine-grained particles, resulting in very broad reflections in the corresponding X-ray diffraction powder patterns that complicate their structural characterization.[11, 14] Previous work has confirmed that synthetic birnessite is a fair representative of naturally occurring birnessites, and it can be prepared in more crystalline forms, rendering it easier to characterize.[14, 17] Synthetic birnessite prepared by high pH precipitation methods are reported to contain vacancy-free manganate layers, rich in Mn^{3+}. Birnessite forms initially as a hydrated metastable intermediate phase

commonly referred to as buserite,[18] containing extra interlayer waters propping the manganate layers apart at an interlayer spacing of 10Å. Once the metastable buserite material is dried, even at room temperature, the excess water is lost and the layers collapse to the 7Å interlayer spacing that is typical of the birnessite phase.[17]

There have been numerous studies investigating the structure of synthetic birnessite, however differences in synthetic methods and considerable disorder and structural variability of this layered material have led to some ambiguities. For example, depending on the synthetic method and the interlayer cation species present, layer stacking may vary, as well as the amounts, coordination geometry and distribution of interlayer species, along with the layer charge and vacancy concentration.[19, 20] The high sorptive capacities are linked to the structural features of the layers. Many studies have probed the nature of the cation ordering and how this correlates with layer Mn vacancy and Mn^{3+} concentrations, primarily through techniques that give information on long range ordering of interlayer cations such as Rietveld refinement of X-ray diffraction, and selected area electron diffraction (SAED) data.[17, 20, 21] Characterizations of the short range local environment of hexagonal, triclinic and cation exchanged birnessites have also been performed via EXAFS and provide valuable structural insights,[22-24] but definitive assignments of possible interlayer cation ordering, particularly with respect to the manganese oxide layer, have yet to be obtained.

In the case of the triclinic high pH form of synthetic sodium birnessite, the heterovalent manganese ions are proposed to order into Mn^{3+}-rows parallel to the *b* axis, separated by two Mn^{4+}-rich rows (See Chapter 1, Figure 1.4 a.).[17, 20] This ordering is used to explain the observed lengthening of the *a* lattice parameter, an elongation in this direction minimizing steric strains from an azimuthally oriented Jahn-Teller axial elongation of Mn^{3+}-O bonds.[16, 25] Jahn-Teller distortions are typically observed in compounds containing greater than 20-30% of the Jahn-Teller ion, Mn^{3+}, in the structure.[26] The ordering of interlayer species is generally less agreed upon, studies diverging on the issue of the positioning of interlayer sodium cations. Rietveld refinements and difference electron Fourier mapping by Post et al.[15] and Lopano et al.[27] produced a model with interlayer sodium cations placed nearly centered between the layers on a split Na/H_2O site, coordinated by six interlayer waters and two layer oxygens above and below the sodium (Figure 3.1 a.),[15, 27] resulting in two long $Na\text{-}O_{layer}$ bond distances of 2.6-2.7Å. In contrast, forward simulations of the sodium birnessite x-ray diffraction powder pattern by

Lanson et al.[16] produced a model in which interlayer sodium is placed on a split site that is coordinated to two interlayer waters and two layer oxygen atoms, one above and one below (Figure 3.1 b.). This split site is shifted along the *c* axis, generating Na-O_{layer} bond distances of 2.46 and 2.74Å. Unfortunately nuances in the placement of interlayer cations in sodium birnessite were difficult to isolate via refinements/simulations of X-ray diffraction patterns or difference electron Fourier mapping due to positional disorder of interlayer species. Gaining insight into the local coordination environment of interlayer cations in the birnessite structure will enrich the understanding of the cation exchange and sorption properties associated with this phyllomanganate.

B. Todorokite

As introduced in the first chapter, todorokite is a 3x3 tunnel structure, believed to be formed through the transformation of buserite/birnessite layers via the template cation Mg^{2+} (observed in synthetic preparations, which may also occur through the same template cation present in nature for naturally occurring todorokites). The todorokite tunnel structure is relatively unstable and therefore this mineral is scarcer in nature than other forms of manganese oxide.[28] However, synthetic todorokites have shown great promise for use as cathode materials.[29-31] As such, improvements in the performance of various preparations of todorokite (tunnel dopants, layer dopants, morphology, etc) necessitate a better understanding of the interactions of tunnel cations with the tunnel walls. The considerable disorder of tunnel waters and cations in these materials make structural analysis difficult via techniques probing long range ordering.[32, 33] Mg^{2+} is the ideal template for this tunnel structure and has been determined to sit at the tunnel center (see Chapter 1, Figure 1.3). Therefore, since Mg^{2+} is more likely to sit at the tunnel center, it is not as informative as other cations that, due to their larger ionic radius, move off center into water positions and associate with the manganate tunnel walls; the connectivity of such cations with the tunnel walls can provide information regarding tunnel wall transition metal composition/oxidation state.

C. Cryptomelane

The mineral cryptomelane, as detailed in the first chapter, consists of double chains of edge shared manganese octahedra that corner share with other double chains to form a 2x2 tunnel structure (see Chapter 1, Figure 1.4). While this mineral occurs naturally, most likely through the transformation of a birnessite or buserite precursor, and plays a similar role in the

environment to that of birnessite, synthetic preparations have also been found to have useful properties as catalysts.[34, 35] For example, Hu et al. have demonstrated that Ag doped cryptomelane shows promise as a catalyst for oxidation of CO, for use in proton exchange membrane fuel cells (PEMFCs) where carbon monoxide concentrations can reduce the efficiency these low temperature range fuel cells.[36] Koivula et al. demonstrated through the use of a simulant hydrometallurgical wastewater that cryptomelane could be synthesized for removal of heavy metal contamination, posing it as a possible economically viable means of removal of heavy metals from mining wastewaters. [37] In their work, they noted the formation of cryptomelane over todorokite, despite greater amounts of Mg^{2+} than K^+ present in the simulant wastewater, indicating the K^+ and hydronium ions were likely acting as templates, favoring the formation of cryptomelane. It is possible that the selectivity of cryptomelane, also referred to as octahedral molecular sieve 2 (OMS 2), is due to the flexibility for the tunnel structure in order to accommodate tunnel cations with varying ionic radii. A distortion involving "twisting" of the Mn octahedra walls was reported by Post et al. in refinements of several natural samples of hollandite-group mineral structures (including cryptomelane) containing a majority of Ba, K and Pb tunnel cations.[38]

D. ^{23}Na MAS NMR

^{23}Na MAS NMR spectroscopy has been successfully used to investigate a number of paramagnetic materials,[39] and is applied here to the study of the local environments in Na-birnessite since the method is sensitive to coordination number, geometry and short range ordering, as well as oxidation state. The work described in Chapter 2 investigated the hyperfine shift contributions of Mn^{3+} and Mn^{4+} to observed ^{23}Na NMR spectra of various sodium manganese oxides, including the Mn^{3+} materials α– and β-$NaMnO_2$, and the mixed Mn^{3+}/Mn^{4+} materials.[40] The contribution to the overall shift was analyzed and larger contributions were observed for Mn^{4+}-O-Na contacts than Mn^{3+}-O-Na contacts. However, the magnitudes of these interactions were found to be strongly dependent on bonding angles, bond lengths and the presence of Jahn-Teller distortion. These trends are used to help rationalize the ^{23}Na NMR spectra of the synthetic sodium buserite and birnessite samples, as well as the sodium-exchanged todorokite and cryptomelane samples prepared for this study. Natural samples of birnessite, todorokite and cryptomelane, kindly provided by Dr. Jeffrey Post, the curator of the mineral collection at the Smithsonian Institution were also obtained for comparison.

This chapter provides insight into the spatial ordering of sodium cations within the interlayer space of buserite and birnessite, as well as the arrangement of interlayer cations with respect to Mn^{3+} and Mn^{4+} ions within the layer. We use ^{23}Na MAS NMR at multiple fields to obtain resolution of the sodium environments present in birnessite samples prepared by different synthetic methods. The magnitudes of the shifts observed in the NMR spectra are used to explain cation positions relative to the manganate layers. ^{23}Na NMR spectra of the tunnel structured materials are used to give insight as to the interaction of sodium ions with the tunnel walls, and spectra collected of natural samples (all found to contain some amount of sodium) provide a measure of the differences between synthetic and natural materials.

II. Experimental

A. Sample Preparation

a. Birnessite

Two different synthetic routes available in the literature that produce birnessite samples with different structural features were chosen for this study. The first synthetic method was taken from optimized parameters reported by Feng et al.:[18, 41] a 0.6M solution of freshly prepared NaOH in 3% H_2O_2 was slowly added to a 0.3M solution of $Mn(NO_3)_2$ with vigorous stirring, immediately forming a dark black/brown precipitate. The reaction was stirred for 5 minutes after the complete addition of $NaOH/H_2O_2$ solution and then aged overnight without stirring. The final precipitate was filtered, washed with copious amounts of de-ionized water and air-dried. A small amount of sample was retained at this point and is denoted: NaBi-I. Once dried, the powder was then re-suspended in a 2M solution of NaOH in a Teflon lined stainless steel hydrothermal bomb and hydrothermally treated at 175ºC for 24 hours. Finally, the sample was filtered, washed with de-ionized water and air-dried. The product of the hydrothermally treated material from this synthetic method is denoted: NaBi-H-I.

In the second synthetic method, first reported by Giovanoli et al.,[42] a 0.5M solution of $Mn(NO_3)_2$ was aerated with O_2 gas through a glass frit at a rate of ~2L/min under vigorous stirring for ~20 minutes, after which a 5.5M solution of NaOH was added. Afterwards, the reaction was run under O_2 gas aeration and stirred for 5 hours. Finally, the black/brown precipitate was filtered and washed with copious amounts of de-ionized water until the pH of the effluent was ~8. A small amount of the isolated material was kept as a wet paste and is denoted NaBu-II. The rest of the material was air-dried and is denoted: NaBi-II.

b. Todorokite

A sodium birnessite precursor was prepared as described in the NaBi-II preparation. Modified from Cui et al.,[43] the prepared NaBi-II was re-suspended in 0.5M $MgSO_4$ and stirred for 24 hours. Materials were then filtered and washed with de-ionized water. Solids were re-suspended in de-ionized water in a round bottom flask fitted with a jacketed water condenser and refluxed for 24 hours in an oil bath. The resulting material, denoted Mg-TD was filtered, washed and air dried. Mg-TD was checked for purity via X-ray diffraction, then re-suspended and stirred

in a solution of 1M NaOH for 24 hours to exchange Mg^{2+} for Na^{+} ions. Materials were filtered, washed with de-ionized water and dried. This Na^{+} exchanged material is denoted Na-TD.

c. Cryptomelane

Preparation of K-cryptomelane was followed according to the synthesis used by Frias et al.,[44] and is briefly described: 40ml of a 1.6M solution of Mn(II) acetate prepared in a round bottom flask. Next, 5ml glacial acetic acid was added and the mixture brought to reflux. A freshly prepared solution of 0.27M $KMnO_4$ was added dropwise to the Mn(II) acetate reaction mixture. After the addition, reaction mixture was refluxed another 24 hours. Resulting materials were filtered, washed with de-ionized water, and dried at 120°C. The black powder was ground and calcined in a crucible at 450°C for 2 hours. This material is denoted K-CRPT. Materials were cooled, then re-suspended in 1M NaOH and stirred for 24 hours. The Na^{+} exchanged materials were filtered, washed with de-ionized water and dried; this material is denoted Na-CRPT.

B. Powder XRD

Powder X-ray diffraction data was collected on a Scintag diffractometer (Cu Kα radiation, λ = 1.54Å) or a Rigaku Miniflex diffractometer (Cr Kα radiation, λ = 2.29Å). A step scan of 0.2°, 2θ, was used for all data collection with a scan speed of 1°/min. All data was collected with or converted to Cu Kα radition for clarity. Diffraction patterns were matched to the JCPDS pattern cards in the diffraction pattern library.

C. ^{23}Na MAS NMR

^{23}Na MAS NMR experiments were performed at 52.8MHz on a CMX-200 spectrometer in a field of 4.7T using a 1.8mm MAS probe at rotor spinning speeds (ν_r) of 38-40kHz. Additional experiments were performed at 95 and 158.4MHz using fields of 8.4 and 14.1T, respectively, using a 1.3mm MAS probe, with spinning speeds of 58-60kHz. Both probes were designed and built by A. Samoson and co-workers (NICFB, Tallinn, Estonia). A rotor synchronized spin-echo pulse sequence (90°-τ-180°-τ_1-acquisition) was used with typical 90° and 180° pulses of 1.3μs and 2.6μs, respectively. Evolution periods were $\tau=n/\nu_r$, where n=2, 3, and $\tau_1=\tau$-20μs. A 1M solution of ^{23}NaCl was used as a reference at 0ppm.

D. NMR Simulations

^{23}Na NMR spectra were modeled using the program WinSolids1 by Dr. K Eichele. Values for quadrupolar coupling constant (χ), the asymmetry parameter (η), and the isotropic

shift (δ_{iso}) were refined. Line broadening was also varied between Gaussian and Lorentzian to achieve the best fit.

III. Results

A. XRD

X-ray diffraction (XRD) was used to investigate the effect of the synthetic method on the birnessite structure and crystallinity.

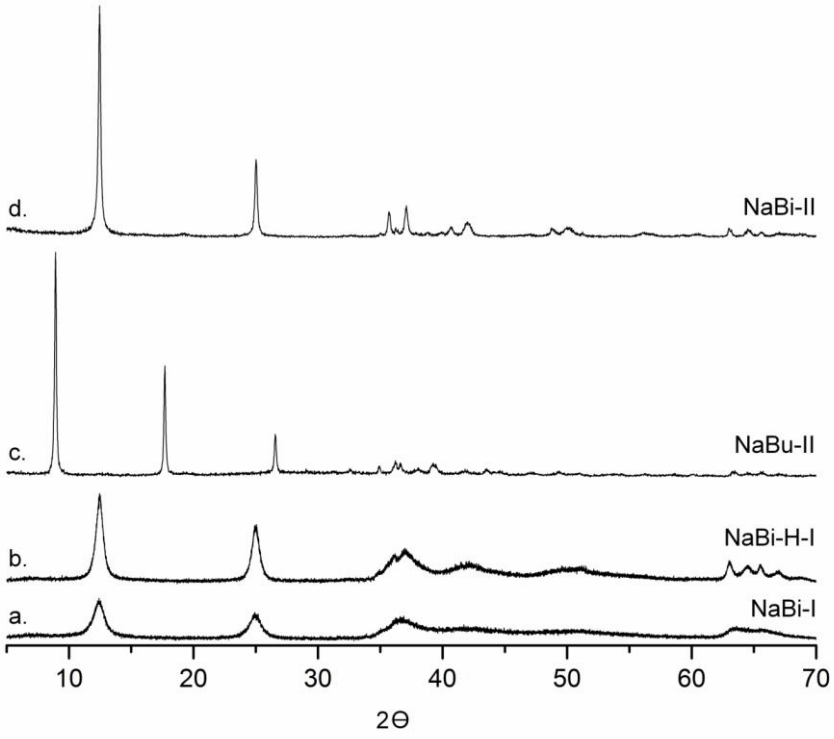

Figure 3.2 XRD patterns of triclinic birnessite synthesized via different synthetic methods. (a) NaBi-I (before hydrothermal treatment), (b) NaBi-H-I (after hydrothermal treatment), (c) NaBu-II, the metastable buserite phase formed during the synthesis of NaBi-II and (d) NaBi-II.

The synthesis of NaBi-H-I includes a hydrothermal step whereby the particle size of the material is increased.[18, 41, 45] Comparison of the XRD powder patterns of the NaBi-H-I material before and after hydrothermal treatment shows a narrowing of the Bragg reflections, as well as an increase in reflection intensity (Figure 3.2 a. and b.). Nonetheless, even the post-hydrothermal treatment sample still exhibits fairly broad Bragg reflections with weak intensities, including broadened 20*l* and 11*l* peaks around 2θ = 35º and split 31*l* and 02*l* peaks around 2θ = 64º, consistent with turbostratically stacked triclinc birnessite.[46] Conversely, the NaBi-II sample, prepared via oxidation of Mn^{2+} in solution by aerating the solution with O_2 gas, produces a more

crystalline triclinic birnessite (Figure 3.2 d.) typically associated with more ordered layer stacking.[16, 46] The NaBu-II sample, isolated before the drying process of the synthesis of NaBi-II, also exhibits high crystallinity but with a larger interlayer spacing (approx. 10Å), consistent with the extra interlayer waters present in the metastable buserite phase (Figure 3.2 c.).[47]

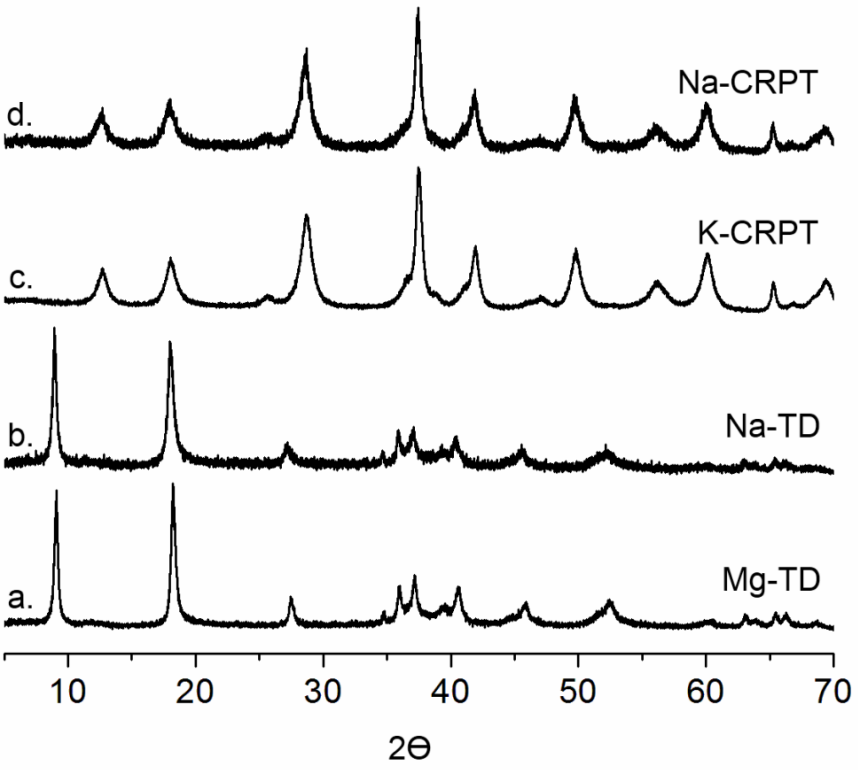

Figure 3.3 XRD of pristine and the exchanged todorokite and cryptomelane. (a) Mg-TD (b) Na-TD (c) K-CRPT and (d) Na-CRPT.

The synthesized Mg-TD and K-CRPT samples are consistent with todorokite and cryptomelane structures. The Na-exchanged materials, Na-TD and Na-CRPT, show a decrease in the crystallinity, but no impurities are observed in the X-ray diffraction powder patterns.

X-ray diffraction patterns of natural samples were not taken. The nominal chemical formula for the natural todorokite was determined to be $(Na_{0.27}Ca_{0.22}K_{0.06}Sr_{0.03}Ba_{0.01})$-$(Mn^{4+}_{5.54}Mg_{0.44}Al_{0.02}Fe_{0.01})O_{12}*3.1H_2O$ and information on the structural characterization of this sample (denoted Natural-TD in this chapter) can be found in Post et al.[33] The nominal chemical formula for the natural cryptomelane was determined to be

$(K_{0.94}Na_{0.25}Sr_{0.13}Ba_{0.10})(Mn,Fe,Al)_8(O,OH)_{16}$ and structural characterization of this sample (denoted Natural-CRPT in this chapter) can be found in Post et al.[38]

B. ^{23}Na MAS NMR of Birnessite

^{23}Na NMR spectra were acquired both for the hydrated buserite phase, NaBu-II, (material was run as a wet paste) and for the subsequently dried birnessite phase, NaBi-II (Figure 3.4). The difference in the local environment of sodium in both phases is apparent from the two spectra. The NaBu-II (Figure 3.4 a.) shows a narrow resonance at 19ppm, the small shift being consistent with sodium ions in a diamagnetic environment.[48] The total absence of peaks with large shifts strongly suggests that these Na^+ ions are fully hydrated within the buserite framework preventing direct interaction with the paramagnetic $[MnO_2]$ layers. This would also imply hydrogen bonding between interlayer water and the manganese oxide layers is the dominant interaction that holds the layers together. Once the material is dried to the birnessite form (Figure 3.4 b.) a broad and complex lineshape with discontinuities at 270 and 347ppm is observed. The shifts clearly indicate that the Na-O_{layer} distances are now short enough for the spin density from the $Mn^{3+/4+}$ ions to be transferred to the Na^+ ion. This is in contrast with reports from Potter and Rossman that IR spectra indicate interlayer cations are only weakly bound to the manganate layers in birnessite.[49]

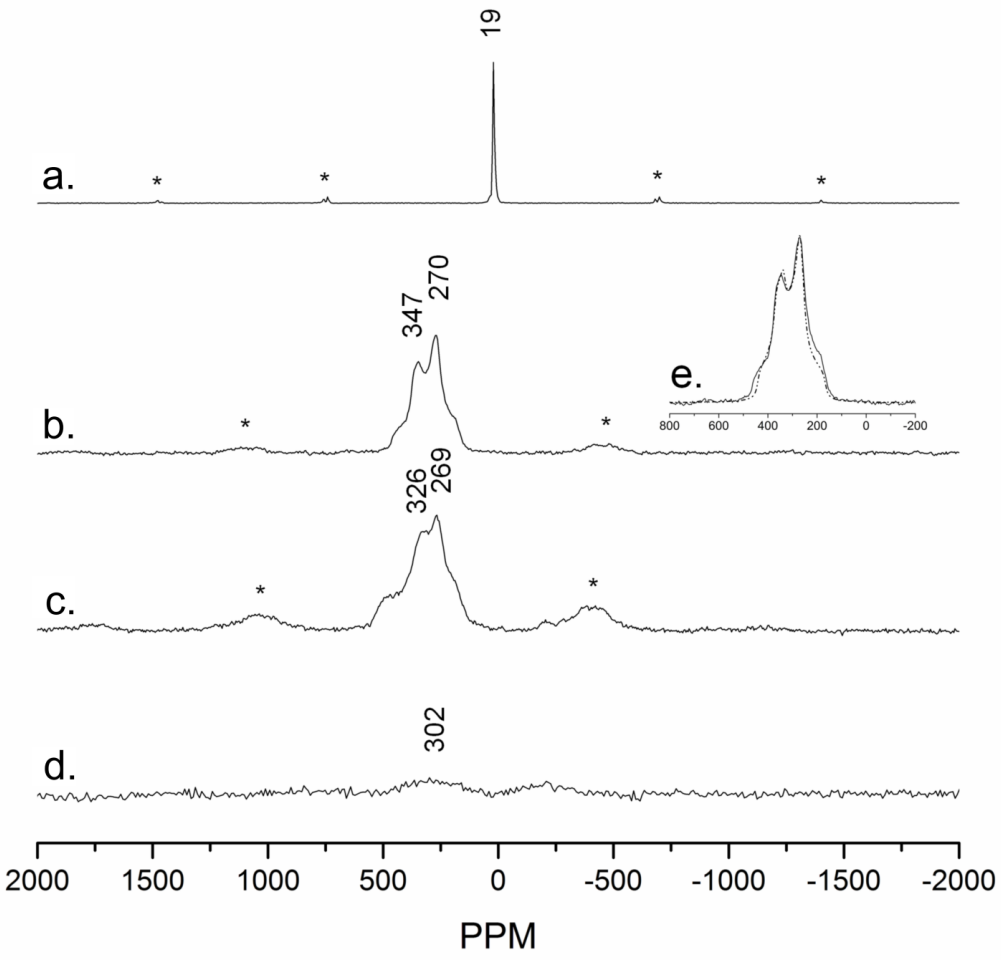

Figure 3.4 ^{23}Na MAS NMR spectra of (a) NaBu-II. (b) NaBi-II. (c) NaBi-H-I. (d) NaBi-I. All spectra were acquired in a 4.7 T field at spinning speeds of 35 - 40 kHz. Spinning sidebands are marked with '*'. (e) Inset of spectrum (b) is a simulation of the central transition of NaBi-II, where values for χ, η, δ_{iso} were extracted for two sites. Site 1: χ = 2.9±0.05MHz, η = 0.69±0.03, δ_{iso} = 444±4ppm; Site 2: χ = 2.8±0.025MHz, η = 1.0±0.05, δ_{iso} = 370±2ppm. The relative intensity of Site 1 to Site 2 used in the simulation is 0.6:1.

Solid state ^{23}Na NMR is sensitive to slight variations in local environment, which can be manifested in distributions of chemical shifts and quadrupolar interactions, both giving rise to broadened resonances. Comparison of the ^{23}Na NMR spectra of the Na birnessite materials NaBi-I, NaBi-H-I and NaBi-II indicates that the crystallinity is correlated with the definition, or lack thereof, of the spectral lineshape (Figure 3 b. – d.). The NaBi-I material shows the most featureless NMR spectrum (Figure 3.4 d.), whereas some distinct peaks clearly become noticeable after hydrothermal treatment (Figure 3.4 c.). Liu et al. observed that both particle size and sodium content appear to increase upon hydrothermal treatment of the initial disordered

birnessite phase, consistent with the weaker signal for NaBi-I compared to NaBi-H-I.[45] The lack of resolution in the NaBi-I material may be due to a disordered arrangement of Mn^{4+} and Mn^{3+} within the manganese oxide layers, or turbostratic layer stacking. Likewise, the increase in defined spectral features observed from pre- to post-hydrothermal treatment is likely due an increase in Mn^{3+} and/or layer stacking order within the framework of the birnessite structure after hydrothermal treatment. In contrast to both the pre- and post-hydrothermally treated NaBi-I material, the ^{23}Na MAS NMR spectrum of the crystalline NaBi-II material (Figure 3.4 b.) has the most well defined discontinuities of the three spectra, which is linked to the existence of the highest degree of ordering of Mn^{3+} within the birnessite layers and/or the highest degree of sodium ordering of all the samples.

The high field (8.4 and 14.1T) ^{23}Na NMR spectra of the NaBi-II and NaBi-H-I materials (Figure 3.5 a. – d.) provide more conclusive information about layer charge distribution and sodium ordering within the interlayers as greater resolution of local environments is achieved at higher fields for second-order quadrupolar broadened lineshapes. (Note that high fields necessitate the use of faster spinning speeds (59-60kHz) to avoid isotropic resonance-sideband overlap. The decrease in peak width and the increase in peak resolution confirm that the complex lineshapes observed at 4.7T arise from large quadrupolar interactions for both the NaBi-H-I and NaBi-II material. The broad isotropic resonances observed in the 4.7T spectrum of NaBi-II are resolved into two distinct sodium sites at 334 and 408ppm at a field strength of 14.1T (Figure 3.5 d.). The simplicity of the spectra suggests a highly ordered, relatively simple distribution of sodium with respect to the manganese oxide layers. The intensities of the peaks in these spectra are quantitative and can be used to obtain a relative ratio between the two sites of nearly 1:1 when spinning sideband intensity is included.

The central transition of NaBi-II spectra at 4.7T and at 14.1T field strengths were simulated by using two sodium sites, referred to as Site1 and Site 2 (see insets, Figure 3.4 e.) and Figure 3.5 e.). The relative intensity of Site 1 in the simulated spectrum at 4.7T was 60%, whereas it was 93% at 14.1T. The reasons for this are not entirely clear, but may be due to a combination of the slightly larger quadrupolar coupling constant of Site 1, coupled with differences in the dipolar coupling, resulting in more central transition intensity contained within the spinning sidebands for the Site 1 resonance at lower fields. The peaks of the 14.1T simulation are shifted relative to the spectrum, which is attributed to the temperature sensitivity of the ^{23}Na

hyperfine shifts, greater frictional heating with faster spinning speeds leading to higher temperatures and smaller shifts. This effect was not taken into account in the simulation. The parameters obtained in these simulations gave large values for the asymmetry parameter, η, for both environments: η = 0.7 for Site 1, and η = 1.0 for Site 2.

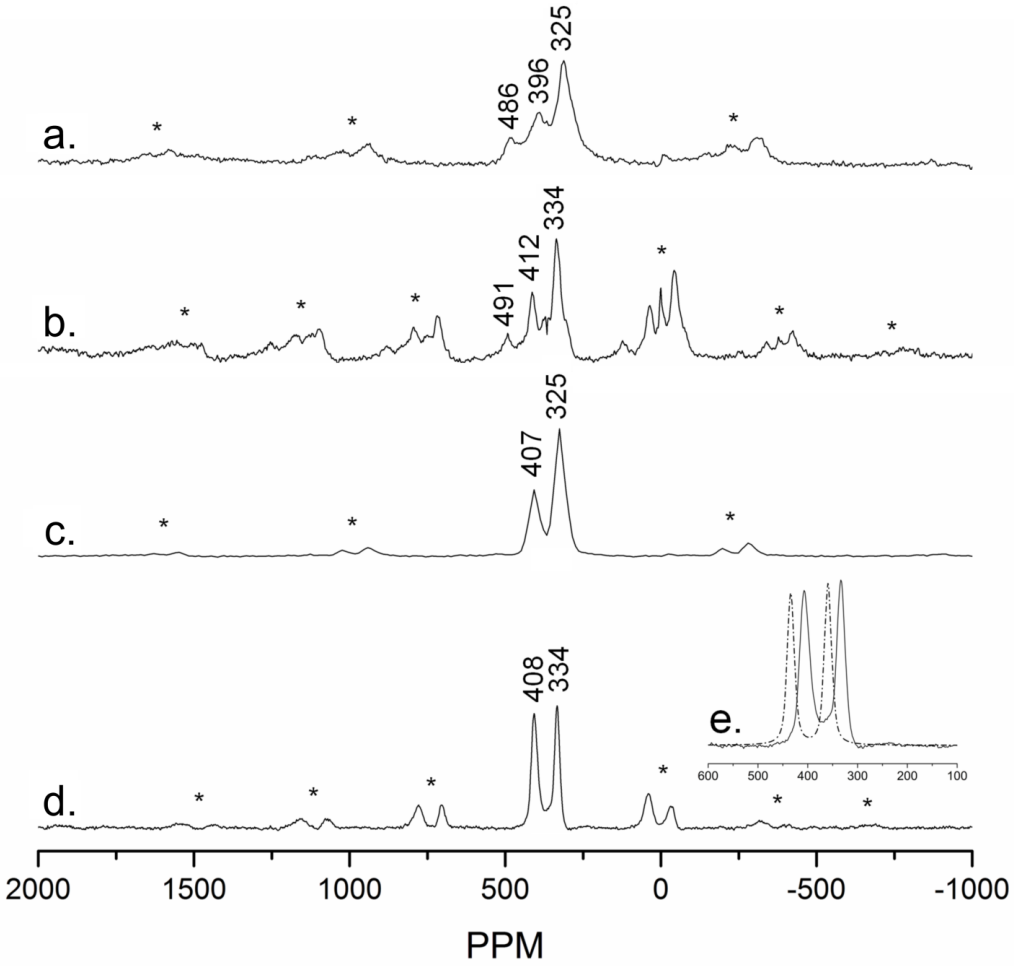

Figure 3.5 (a) ^{23}Na NMR spectra of NaBi-H-I at a 8.4T field strength and (b) at 14.1T with spinning speed of 60kHz (c) ^{23}Na NMR spectra of NaBi-II at a 8.4T field strength and (d) at 14.1T with spinning speeds of 59kHz. Spinning sidebands are marked with '*'. (e) spectral simulation of the central transition in (d) using the χ, η, δ_{iso} values refined for two sites in the 4.7T spectrum. See Figure 3.4(e). Site 1: χ = 2.9±0.05MHz, η = 0.69±0.03, δ_{iso} = 444±4ppm; Site 2: χ = 2.8±0.025MHz, η = 1.0±0.05, δ_{iso} = 370±2ppm. Spectral simulation used a relative intensity of 0.93:1 for sites 1:2 at 14.1T field strength.

The NaBi-H-I material gives a similar spectrum at 4.7 T to that of the NaBi-II material (Figure 3.4 c.) but with slightly less well-defined discontinuities at 269 and 326ppm and shoulders at 188 and 495ppm. As the field strength increases, the resolution of a number of

sodium sites is achieved. At 14.1 T, clear isotropic resonances at 334, 412, and 491ppm emerge, with a slight shoulder at 300ppm that could be an additional sodium site (Figure 3.5 b.). Of particular significance is the fact that the two most intense of these isotropic resonances occur at 334 and 412ppm, *i.e.* at the same shift position as those of the main peaks in the ^{23}Na spectra of the NaBi-II (Figure 3.5 d.). This would indicate that the ordering scheme of the interlayer sodiums in the NaBi-H-I material is largely the same as that observed in the NaBi-II, with other local sodium environments generated from possible structural disorder in layer stacking and layer defects.

C. ^{23}Na NMR of Synthetic and Natural Todorokite and Cryptomelane

The ^{23}Na NMR spectra of the synthetic and natural samples of todorokite and cryptomelane are shown in Figure 3.6. While a similar number of scans were collected for both the ^{23}Na NMR spectra of Na-TD and Natural-TD (n = 271,534 scans and 224,667 scans for Na-TD and Natural-TD, respectively), the signal to noise of the Na-TD spectrum is considerably poorer than that of the Natural-TD, indicating that exchange of sodium back into the synthetic material was minimal compared to the amount of sodium present in the natural material (Figure 3.6 a. and b.). The signal to noise of the Na-CRPT ^{23}Na NMR spectrum (n = 36,000 scans) compared to that of the Natural-CRPT spectrum (n = 93,000 scans) is also considerably worse. The signal to noise might be improved by collection of an increased number of scans for the Na-CRPT sample, however it is also likely that the exchange of sodium back into the synthetic material was minor, and that the sodium content of the Natural-CRPT sample is also greater than the sodium content in the synthetic Na-CRPT sample. Conversely, the natural samples appear to have a comparably greater amount of sodium in the structure (Figure 3.6 c. and d.).

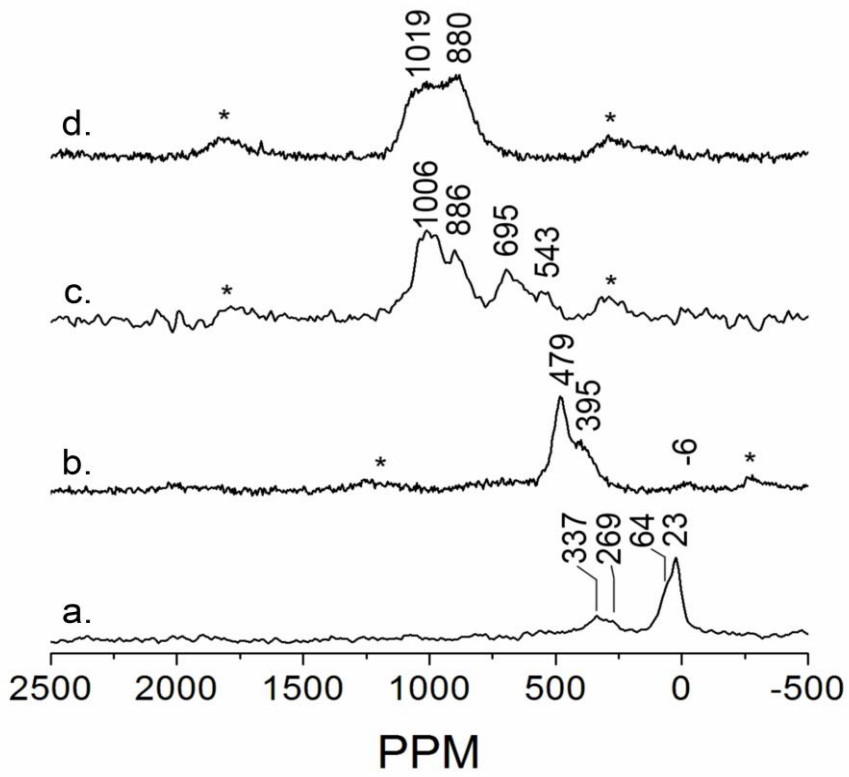

Figure 3.6 ^{23}Na NMR spectra of synthetic and natural todorokite and cryptomelane materials. (a) Na-TD (b) Natural-TD (c) Na-CRPT (d) Natural-CRPT. All spectra taken at 4.7T at spinning speeds of 38 – 40kHz. Spinning sidebands are marked with '*'.

The relative intensities of the two shifts observed in Na-TD indicate that a considerable amount of sodium present in the material is located at or near the center of the tunnels at 23ppm. A second peak with discontinuities at 269 and 337ppm are hyperfine-shifted environments, indicating that the sodium environment(s) is bonded to the manganate tunnel walls. Conversely, the natural sample shows only minor amounts of sodium located at the tunnel center. The observed shift for this environment (-6ppm) is considerably different from the synthetic material (23ppm), but the exact shift of this environment may inaccurately identified due to the very weak intensity of this peak in the natural material. Slightly greater magnitudes of the discontinuities of the hyperfine shifted environment(s) (395 and 479ppm) are also observed in the Natural-TD sample spectrum.

The resolution of the environments in Na-CRPT is poor, making assignment of environments difficult. However, resonances are observed at 543, 695, 886, and 1006ppm. All observed environments exhibit hyperfine shifts, indicating all sodium present in this material is

covalently bonded to the tunnel walls. The Natural-CRPT material, surprisingly, does not exhibit the 543 and 695ppm environments observed in Na-CRPT. Even more surprisingly, only the two larger magnitude hyperfine environments at 880 and 1019ppm are observed, particularly considering the nominal chemical formula determined by Post et al. (1982) suggests Fe and Al maybe compose some of the tunnel walls; the presences of these would be expected to produce more sodium environments.

IV. Discussion

A. Birnessite

The birnessite spectra show significantly lower shifts than those observed for other mixed valence sodium manganese oxides reported in previous ^{23}Na NMR studies (Figure 3.5).[40] In the cited work, sodium manganese oxides containing Mn^{3+} and Mn^{4+}, such as α-$Na_{2/3}MnO_2$ with a 3 to 1 Mn^{3+}:Mn^{4+} composition, produced noticeably larger shifts (1521 and 1637ppm) compared to compounds containing only Mn^{3+}, such as α-$NaMnO_2$ (725ppm).[40]

The observed shifts in the birnessite spectrum are roughly half that of the shifts observed in the Mn^{3+} sodium manganese oxide compounds from the previously mentioned study,[40] despite the presence of approximately 2/3 Mn^{4+} ions in the triclinic birnessite layers, which would be expected to produce larger shifts. Assuming Mn^{3+} orders within the manganate layers into rows as described in the introduction,[16, 25] the first implication of these spectra is that interlayer sodium is predominantly ordered near these Mn^{3+}-rich rows. Furthermore, these small hyperfine shifts are also consistent with the structural models postulated in previous work. The model proposed Post et al. (Figure 3.1 c.) in which sodium sits at the center of the interlayer spacing, will produce a weak Fermi contact shift, as a result of the two long Na-O_{layer} distances, assuming they still produce sufficient orbital overlap for the through bond transfer of spin density.[15] Earlier structural studies of other inorganic materials, such as sodium metaborate and wyllieite ($Na_2Fe_2Al(PO_4)_3$), indicate that elongated Na-O bond lengths of 2.6-2.8Å do occur.[50-52] There are also considerably fewer Na^+-O-$Mn^{3+/4+}$ contacts than the sodium environments of the model compounds (six compared to sixteen or eighteen).[40] Thus, the presence of fewer Na^+-O-$Mn^{3+/4+}$ contacts, as well as longer Na-O bonds could explain the significantly smaller hyperfine shifts seen here, over that expected purely from the oxidation state of the manganese ions. The model proposed by Lanson et al. (Figure 3.1 d.) also provides a plausible positional scheme in which

interlayer sodium forms a distinct bond with an oxide ion of a single MnO_2 layer, clearly allowing a stronger hyperfine shift, but producing only three Na^+-O-$Mn^{3+/4+}$ interactions.[16] In this case, the mechanism that leads to a smaller observed hyperfine shift in NaBi-H-I and NaBi-II would dominated by the significantly fewer Na^+-O-$Mn^{3+/4+}$ interactions via a more conventional Na-O bond distance.

The two ^{23}Na resonances found in the NaBi-I are associated with large asymmetry parameters, η, or 0.7 and 1.0 for Site 1 and 2, respectively, based on our spectral simulations. Large η values indicate highly asymmetric local environments, which is in support of interlayer sodium shifted off-center and associated with a single manganese oxide layer, *i.e.*, the model of Lanson et al. The simulations could not be optimized to capture some weak intensity of the left shoulder of the central transition in the 4.7T spectrum (see inset of Figure 3.4 e.). This discrepancy could arise from limitations of the simulation software in which infinite spinning is assumed. It is also possible that the intensity not expressed in the simulation represents a minor amount of a third sodium environment around 480-500ppm. Such an environment is resolved the 14.1T spectrum of the NaBi-H-I material at 491ppm (Figure 3.5 b.) and could therefore also be present in some, much smaller amount in NaBi-II (Figure 3.5 d.).

Ordering schemes of interlayer cations and layer charge distribution that could explain two sodium sites with a ratio of close to 1:1 were examined. A shifted sodium site, as given in the model by Lanson et al.,[16] was assumed initially, since this simplifies the analysis considerably. Since in this model, sodium is covalently bonded to only one of the two layers, the distribution of layer charge will be a more significant factor determining the local environment of sodium than the registry between the layers. Following from the ordering of Mn^{3+} ions into rows separated by two rows rich in Mn^{4+} ions, two unique sodium environments can be generated by staggering the sodium site along these Mn^{3+} rows, either above or below the layer; one type of ion is coordinated via oxygen to two Mn^{4+} and one Mn^{3+} (Figure 3.7 a.) and the second is coordinated via oxygen to one Mn^{4+} and two Mn^{3+} (Figure 3.7 b.). A third site is also possible (Figure 3.7 c.), but since this is near Mn^{4+} ions only, it is likely to be higher in energy.

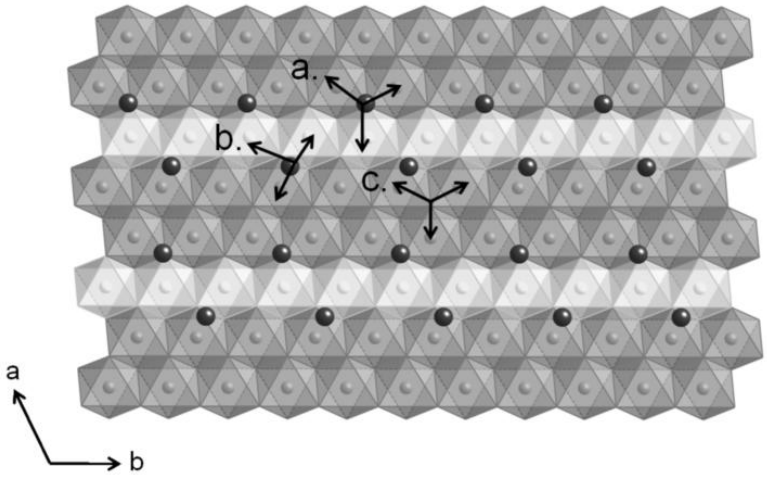

Figure 3.7 Representation of a possible cation ordering scheme for sodium, assuming Mn^{3+} (light grey) rich rows ordered along *b* separated by two Mn^{4+} (dark grey) rich rows. Interlayer cations (white) are staggered along the ordered rows of Mn^{3+} resulting in two sodium environments on either side of the layer, though all Na^{+} are shown on one side in this idealized structure. One sodium site (a) is coordinated, via oxygen, to two Mn^{4+} ions and one Mn^{3+} ions. The second sodium site (b) is coordinated, via oxygen, to two Mn^{3+} ions and one Mn^{4+}ions. A third, less favorable site (c) where Na^{+} is coordinated to three Mn^{4+} ions may be possible due to some disorder of interlayer sodium.

The sodium environment coordinated to two Mn^{4+} (Figure 3.7 a.) would give rise to the higher of the two observed isotropic shifts in the ^{23}Na NMR spectra of this sample (Figure 3.5 d.), based on the higher shifts expected for Mn^{4+}-O-Na contacts compared to Mn^{3+}-O-Na ions. With this assignment, the 14.1T spectrum of the more disordered NaBi-H-I material becomes more informative (Figure 3.5 b.). The two most intense resonances of the high field NaBi-H-I spectrum at 334 and 412ppm, are the same as those observed in the ordered NaBi-II material, are separated by about 80ppm and differ by only one Mn^{3+}, and are therefore assigned to the environments nearby one and two Mn^{4+} ions, respectively. Similarly, a third resonance at 491ppm is separated by about 80ppm from the 412ppm environment. On this basis, the 491ppm resonance is assigned to a sodium environment coordinated to three Mn^{4+} ions (Figure 3.6 c.) which, though not an ideal environment for charge balance, may occur in birnessites with a certain degree of layer and interlayer cation disorder. Furthermore, this indicates that the Mn^{4+}-rich rows of the more ordered NaBi-II material are almost, if not completely, vacant of interlayer sodium. Finally, the fact that the spectra can be readily explained based on the proximity of Na^{+} to one, two or three Mn^{4+} ions, provides further support for the off-center model: more than three

resonances are expected for sodium environments located in the center of the layer since configurations generated by binding to two layer oxygens need to be considered. This results in many more local environments Na($OMn^{3+}_{x}OMn^{4+}_{6-x}$) (where we have ignored the binding to the waters in the layers in this formula) in systems that are not fully ordered, or where there is no registry of the ordering between the layers.

B. Todorokite

The sharper peak at 23ppm in the Na-TD spectrum (Figure 3.6 a.), assigned to sodium ions placed at or near the tunnel center has a slight shoulder, which may be the result of asymmetric coordination by tunnel waters. Since sodium has a non-ideal ionic radius for this structure, it is possible that this environment may not be well ordered, shifting a bit off center towards the tunnel walls. The hyperfine shifted environment in this same spectrum has a similar magnitude to those observed in birnessite and likely results from the same factors as the Na environments of the birnessite samples: few Mn-O-Na contacts and specifically, the presence of Mn^{3+}-O-Na^{+} contacts. Sodium ions associated with tunnel walls are likely to occupy the $H_2O(3)$ site (see Chapter 1, Figure 1.3), for which refinements have determined it to be only partially occupied by water.[32] The $H_2O(3)$ site is closest to tunnel oxygen, which would produce covalent bonding distances for the Fermi-contact interaction. This would also be consistent with the relatively "small" magnitude of the hyperfine shifted sodium environment(s); refinements of the todorokite structure indicated that lower valence manganese preferentially occupies the corner manganese sites (Mn2 and Mn4 from Figure 1.3, Chapter 1) tunnel corners.[32] Sodium could feasibly coordinate to two tunnel oxygen from the $H_2O(3)$ position (Figure 3.8). Coordination of sodium to a single oxygen on one of the tunnel walls, where Mn2 and/or Mn4 sites are rich in Mn^{3+}, could produce the same sodium environments as the ones assigned in birnessite with shifts around 270 and 347ppm at 4.7T magnetic field strength. However, for definitive assignments, careful analyses of the location of sodium ions, their coordination in todorokite and resulting bonding angles would be required.

The spectrum of Natural-TD is notably different from the synthetic material (Figure 3.6 b.), indicating cation placement is considerably different. An environment with weak intensity is observed around -6ppm, and is assigned to fully hydrated sodium cations centered in the tunnel. The magnitude of the diamagnetic shift differs from Na-TD (23ppm), but the exact magnitude of

the shift may be slightly skewed by the weak intensity of the peak. Hyperfine shifted environments are also observed in the ^{23}Na NMR spectrum of Natural-TD, and are slightly greater than those observed in Na-TD. It is possible the hyperfine shifted environments differ between the synthetic and natural samples due to poor signal to noise of the Na-TD spectrum. However, the nominal chemical formula determined for Natural-TD, $(Na_{0.27}Ca_{0.22}K_{0.06}Sr_{0.03}Ba_{0.01})$-$(Mn^{4+}_{5.54}Mg_{0.44}Al_{0.02}Fe_{0.01})O_{12}$*$3.1H_2O$, indicates that considerable amounts of Mg, and minor amounts of Al and Fe also compose the tunnel walls. Tunnel Mg and Al ions introduce only diamagnetic contacts via tunnel oxygen to the observed nucleus, and the very minor component of Fe ions present in tunnel walls is insufficient to account for greater hyperfine shifts. Therefore, it seems most likely that sodium cations bind near tunnel regions rich in Mn^{4+}, otherwise the shifts would be similar to those observed in the Na-TD spectrum. Also, without preferential sodium ordering near these Mn^{4+} rich environments, smaller hyperfine shift magnitudes would also be observed due to contacts with diamagnetic tunnel ions.

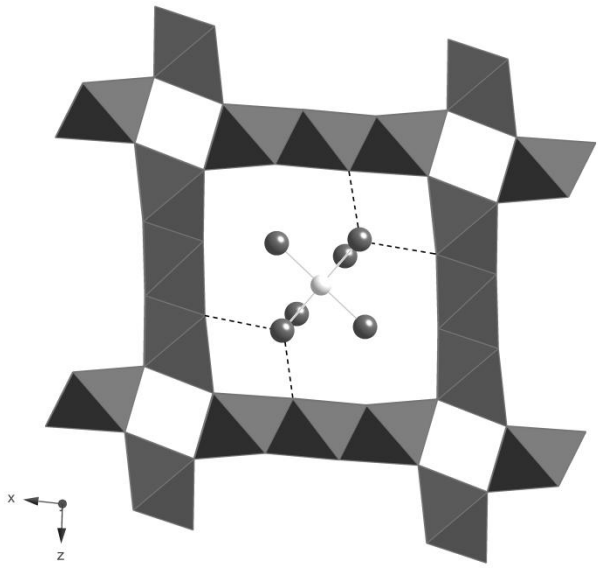

Figure 3.8 Modified from Figure 1.3 to show the possible covalent bonding of a sodium ion occupying the $H_2O(3)$ site. Bonding distances are not available for sodium at this site, however refinements provided for water sitting at this site produce interatomic distances with nearest tunnel oxygen at 2.96 and 2.69Å.[32]

C. Cryptomelane

The presence of several hyperfine shifts observed in both Na-CRPT and Natural-CRPT spectra (Figure 3.6 c. and d.) confirms previous refinements that sodium does not sit at the center of the tunnel (See Chapter 1, Figure 1.4).[38] The spectrum of Na-CRPT shows two regions of hyperfine shifted sodium environments, 543 – 695ppm and 886 – 1006ppm. The poor signal to noise of the Na-CRPT spectrum (relative to Natural-CRPT) indicates only a small amount of sodium was exchanged back into the material, and that a considerable amount of the potassium counter ion is still present. The variety of shifts may be explained by varying degrees of tunnel distortions that occur when counter ions of smaller radius than the ideal potassium ion are present.[38] For example, tunnel distortions surrounding sodium environments near potassium rich regions may be minimal, in which case, sodium likely shifts off center toward tunnel corners to make covalent contacts with tunnel walls. Conversely, sodium rich regions of the tunnel structure may have greater distortions, enabling a larger number of contacts with the tunnel walls. A greater number of contacts with tunnel walls would give rise to hyperfine shifts of larger magnitude.

This rationale may also explain why the lower magnitude shifts at 543 and 695ppm are not observed in the Natural-CRPT sample – the larger variety of counter ions present in the tunnels may generate consistent amounts of distortions such that sodium is always able to make a larger number of contacts with tunnel walls. The relative simplicity of the ^{23}Na NMR spectrum of the natural sample (and the similarity to the Na-CRPT sample spectrum) also suggests that there are only minor amounts of Fe and Al in the Natural-CRPT sample, for which the chemical formula does not specify the relative amounts of Mn, Al and Fe, and that sodium is predominately coordinated to Mn in the tunnels. Specific assignment of sodium environments to the observed shifts cannot be made without more detailed analysis of sodium cation locations within the cryptomelane structure. It is important to note that, regardless of specific assignments, the magnitude of all the hyperfine shifts observed suggest the manganese surrounding the observed sodium environments is more Mn^{4+} rich than in birnessite or todorokite.

Finally, we note that the effect of the Jahn-Teller distortions has not been considered in the analysis and assignment of the observed shifts in this study. In Chapter 2, the work on sodium manganese oxide model compounds clearly illustrate that the presence of Jahn-Teller distortions had a significant impact on shifts.[40] For example, comparison of α- and β-$Na_{2/3}MnO_2$,

layered materials in which the slightly lower Mn average oxidation state of the β- form gives rise to a Jahn-Teller distortion, shows α-$Na_{2/3}MnO_2$ to have resonances with notably larger overall shifts (1521 and 1637ppm) than those observed in spectra of β-$Na_{2/3}MnO_2$ (794 and 1112ppm).[40] We considered the different environments generated by the preferential ordering of Na^+ ions with respect to the orientation of the Jahn-Teller distorted Mn^{3+} ions and the possible effects that this might have on the hyperfine shifts. It is possible that a contribution to the differences in shifts between the three resonances may result from effects arising from the Jahn-Teller distortions, but we found no simple assignments to specific local environments. Future work will use density functional theory calculations, as was performed in our previous sodium manganese oxide compounds paper,[40] to explore this effect.

V. Conclusions

The sensitivity of MAS NMR to detect interactions between Na^+ and the manganate layers was demonstrated in the comparison of the ^{23}Na spectrum of the metastable buserite, NaBu-II, with that of the NaBi-II birnessite material, confirming the necessity of allowing reasonable orbital overlap for interlayer sodium ions in proposed structural models. The Fermi contact shift necessitates a sufficient measure of orbital overlap for the interaction to be observed spectrally. As a consequence of this requirement, interlayer sodium ions are likely to be associated with a single manganese oxide layer and therefore shifted off center in the interlayer space. This would also explain the minimal number of different sodium environments, as well as the smaller observed hyperfine shifts associated with these sodium environments due to fewer $Mn^{3+/4+}$-O-Na contacts. Spectral simulations also support asymmetric sodium sites.

The local sodium environments resolved using MAS NMR allowed a more complex discussion of interlayer sodium cation ordering with respect to structural models already proposed in the literature. The NMR spectra of NaBi-II indicate that the sodium ordering is relatively simple and is likely driven by the ordering of Mn^{3+} within the manganese oxide layers. The NMR spectra of NaBi-H-I indicates the predominant ordering scheme of sodium within the interlayers is the same as the ordering scheme found in the NaBi-II but with additional local sodium environments likely generated due to disorder of charge distribution within the manganese oxide layer.

Comparison of ^{23}Na NMR spectra of synthetic and natural samples of todorokite and cryptomelane indicate the location of sodium in the tunnels vary considerably. The majority of sodium present in Na-TD is fully hydrated at or near the tunnel center, with a notably weaker hyperfine shifted component, indicating only a minor amount of sodium ions shift off center and bind with tunnel oxygen. Conversely, the spectrum of the Natural-TD sample indicates that sodium is predominately bound to tunnel oxygen, and preferentially orders near Mn^{4+} rich regions of the tunnel wall. The spectrum of Na-CRPT shows a spread of differing hyperfine shifted environments that can be rationalized by varied amounts of tunnel distortions due to a notable amount of potassium still present in the sodium exchanged sample, likely containing sodium environments in potassium rich tunnel regions (minor tunnel distortions) and sodium environments in sodium rich tunnel regions (more severe tunnel distortions). The lack of the lower magnitude hyperfine shifts in the Natural-CRPT sample suggest that numerous types of tunnel cations invoke considerable tunnel distortions consistently throughout the material, allowing sodium ions to make a larger number of contacts with tunnel walls.

VI. References

1. O'Reilly, S. E., Hochella, M. F., *Geochim. Cosmochim. Acta* **67**, 4471-4487 (2003).

2. Pena, J., Kwon, K. D., Refson, K., Bargar, J. R., Sposito, G., *Geochim. Cosmochim. Acta* **74**, 3076-3089 (2010).

3. Mckenzie, R. M., *Aust. J. Soil Res.* **18**, 61-73 (1980).

4. Mckenzie, R. M., *Aust. J. Soil Res.* **5**, 235-& (1967).

5. Lanson, B., Drits, V. A., Gaillot, A. C., Silvester, E., Plancon, A., Manceau, A., *Am. Mineral.* **87**, 1631-1645 (2002).

6. Sherman, D. M., Peacock, C. L., *Geochem. Cosmochim. Ac.* **74**, 6721-6730 (2010).

7. Fuller, C. C., Harvey, J. W., *Environ Sci Technol* **34**, 1150-1155 (2000).

8. Harvey, J. W., Fuller, C. C., *Water Resour. Res.* **34**, 623-636 (1998).

9. Bargar, J. R., Fuller, C. C. , Marcus, M. A., Brearley, A. J., De la Rosa, M. P., Webb, S. M., Caldwell, W. A. , *Geochim. Cosmochim. Acta* **73**, 889-910 (2009).

10. Toner, B., Manceau, A., Webb, S. M., Sposito, G., *Geochim. Cosmochim. Acta* **70**, 27-43 (2006).

11. Post, J. E., *P Natl Acad Sci USA* **96**, 3447-3454 (1999).

12. Villalobos, M., Lanson, B., Manceau, A., Toner, B., Sposito, G., *Am. Mineral.* **91**, 489-502 (2006).

13. Villalobos, M., Toner, B., Bargar, J., Sposito, G., *Geochim. Cosmochim. Acta* **67**, 2649-2662 (2003).

14. Glasby, G. P., Ed., *Marine Manganese Deposits*, vol. 15 (Elsevier Scientific Publishing Company, Amsterdam, ed. 1, 1977), vol. 15, 1, pp. 523.

15. Post, J. E., Heaney, P. J., Hanson, J., *Powder Diffr.* **17**, 218-221 (2002).

16. Lanson, B., Drits, V. A., Feng, Q., Manceau, A., *Am. Mineral.* **87**, 1662-1671 (2002).

17. Kuma, K., Usui, A., Paplawsky, W., Gedulin, B., Arrhenius, G., *Mineral Mag* **58**, 425-447 (1994).

18. Feng, Q., Lui, L., Yanagisawa, K., *J. Mater. Sci. Lett.* **19**, 1567-1570 (2000).

19. Lanson, B., Drits, V. A., Silvester, E., Manceau, A., *Am. Mineral.* **85**, 826-838 (2000).

20. Drits, V. A., Silvester, E., Gorshkov, A. I., Manceau, A., *Am. Mineral.* **82**, 946-961 (1997).

21. Post, J. E., Veblen, D. R., *Am. Mineral.* **75**, 477-489 (1990).

22. Silvester, E., Manceau, A., Drits, V. A., *Am. Mineral.* **82**, 962-978 (1997).

23. Webb, S. M., Tebo, B. M., Bargar, J. R., *Am. Mineral.* **90**, 1342-1357 (2005).

24. Manceau, A., Lanson, B., Drits, V. A., *Geochim. Cosmochim. Acta* **66**, 2639-2663 (2002).

25. Gaillot, A. C., Drits, V. A., Manceau, A., Lanson, B., *Microporous Mesoporous Mater.* **98**, 267-282 (2007).

26. Rogers, D. B., Germann, R. W., Arnott, R. J., *J. Appl. Phys.* **36**, 2338-2343 (1965).

27. Lopano, C. L., Heaney, P. J., Post, J. E., Hanson, J., Komarneni, S., *Am. Mineral.* **92**, 380-387 (2007).

28. Vodyanitskii, Y. N., *Eurasian Soil Sci+* **42**, 1170-1178 (2009).

29. Duncan, M. J., Leroux, F., Corbett, J. M., Nazar, L. F., *J. Electrochem. Soc.* **145**, 3746-3757 (1998).

30. Kumagai, N., Komaba, S., Abe, K., Yashiro, H., *J. Power Sources* **146**, 310-314 (2005).

31. Song, C. H., Li, R. Q., Liu, F., Feng, X. H., Tan, W. F., Qiu, G. H., *Electrochim. Acta* **55**, 9157-9165 (2010).

32. Post, J. E., Heaney, P. J., Hanson, J., *Am. Mineral.* **88**, 142-150 (2003).

33. Post, J. E., Bish, D. L., *Am. Mineral.* **73**, 861-869 (1988).

34. Liao, S. J., Zhu, D. W., Li, Y., Liu, G. L., Liu, L. H., *React. Kinet. Mech. Catal.* **102**, 303-311 (2011).

35. Atribak, I., Bueno-Lopez, A., Garcia-Garcia, A., Navarro, P., Frias, D., Montes, M., *Appl. Catal. B-Environ.* **93**, 267-273 (2010).

36. Hu, R. R., Yan, C. F., Xie, L. Y., Cheng, Y., Wang, D. Z., *Int. J. Hydrogen Energy* **36**, 64-71 (2011).

37. Koivula, R., Pakarinen, J., Sivenius, M., Sirola, K., Harjula, R., Paatero, E., *Sep. Purif. Technol.* **70**, 53-57 (2009).

38. Post, J. E., Vondreele, R. B., Buseck, P. R., *Acta Crystallogr. Sect. B-Struct. Commun.* **38**, 1056-1065 (1982).

39. Carlier, D., Blangero, M., Menetrier, M., Pollet, M., Doumerc, J.P., Delmas, C., *Inorg. Chem.* **48**, 7018-7052 (2009).

40. Aldi, K. A., Middlemiss, D. S., Cabana, J., Sideris, P. J., Grey, C. P., (Submitted for Publication).

41. Feng, Q., Sun, E. H., Yanagisawa, K., Yamasaki, N., *J. Ceram. Soc. Jpn.* **105**, 564-568 (1997).

42. Giovanoli, R., Stahli, E., Feitknecht, W., *Helv. Chim. Acta* **53**, 209 - 220 (1970).

43. Cui, H. J., Qiu, G. H., Feng, X. H., Tan, W. F., Liu, F., *Clays Clay Miner.* **57**, 715-724 (2009).

44. Frias, D., Nousir, S., Barrio, I., Montes, M., Lopez, T., Centeno, M. A., Odriozola, J. A., *Mater. Charact.* **58**, 776-781 (2007).

45. Liu, L., Feng, Q., Yanagisawa, K., *J. Mater. Sci. Lett.* **19**, 2047 - 2050 (2000).

46. Drits, V. A., Lanson, B., Gaillot, A. C., *Am. Mineral.* **92**, 771-788 (2007).

47. Johnson, E. A., Post, J. E., *Am. Mineral.* **91**, 609-618 (2006).

48. Mackenzie, K. J. D., Smith, M. E., *Multinuclear Solid-State NMR of Inorganic Materials*. R. W. Cahn, Ed., Pergamon Materials Series (Elsevier Science Ltd., ed. 1st, 2002), vol. 6, pp. 727.

49. Potter, R. M., Rossman, G. R., *Am. Mineral.* **64**, 1199-1218 (1979).

50. Marezio, M., Plettinger, H. A., Zachariasen, W. H., *Acta Crystallogr.* **16**, 594-595 (1963).

51. Brown, I. D., Shannon, R. D., *Acta Crystallogr.* **A29**, 266-282 (1973).

52. Miletich, R., Pertlik, F., *J. Alloys Compd.* **268**, 107-111 (1998).

Chapter 4

^{2}H NMR Investigation of Layer Vacancies in Hexagonal Birnessites

Hexagonal birnessite is a layered manganese oxide characterized by a negative layer charge arising from layer vacancies. There is great interest in characterizing and quantifying these layer vacancies as previous studies have linked the high adsorption capacity of birnessite to layer vacancies. Low temperature ^{2}H MAS NMR was used to observe the multiple deuterium environments present in a series of deuterated hexagonal birnessites synthesized with increasing layer manganese vacancy concentrations. A hyperfine shifted environment at 120-133ppm is assigned to charge compensating deuterons at layer vacancies and confirmed by the disappearance of this peak in the low temperature ^{2}H NMR spectra of Zn^{2+} exchanged samples. Two kinds of interlayer water are identified: a sharp peak at 2-4ppm is assigned to interlayer water strongly bound to interlayer K^{+}, and a broad baseline intensity is assigned to interlayer water strongly hydrogen bonded to layer oxygen. A second hyperfine-shifted environment at 56-59ppm is identified as deuterons bonded to terminal manganese octahedra at particle edges. Low temperature ultra fast MAS experiments are used to isolate the isotropic resonances for integration of deconvoluted peaks and spin counting methods are used to quantify the moles of vacancies per mg of sample, confirming a general trend of increasing layer vacancy concentrations across the sample series.

I. Introduction

A. Hexagonal Birnessite

This investigation focuses on hexagonal birnessite, as discussed in Chapter 1, in which the major layer defects creating layer charge are Mn^{4+} vacancies. It has been indicated in the literature that the optimal ordering of layer vacancies in hexagonal birnessite may be a linear arrangement of alternating Mn^{4+}-□-Mn^{4+} (where □ represents a layer Mn vacancy),[1, 2] which is consistent with reported formation mechanisms for the synthesis of hexagonal birnessite rather than a hexagonal distribution similar to that of the layered mineral, chalcophanite.[3] Hexagonal birnessite is typically formed by first precipitating a triclinic form of birnessite and subsequently acidifying the suspension.[4, 5] The triclinic form of birnessite contains little to no layer vacancies; the layer charge arising from the presence of Mn^{3+}, which is believed to order in Mn^{3+} rich rows separated by two rows of Mn^{4+} oriented parallel to the *b* axis.[6, 7] Upon lowering the pH of a suspension of triclinic birnessite, disproportionation involving two neighboring layer Mn^{3+} within the Mn^{3+} rich rows results in a layer vacancy via the formation of an Mn^{2+} ion, which is taken up into the reaction solution, and leaving behind a Mn^{4+} ion in the Mn^{3+} rich row.[2, 5] This resulting birnessite structure, characterized by high layer vacancy content, is referred to as hexagonal birnessite.

Many studies have investigated the adsorption of various cations in hexagonal birnessites, successfully linking protons and interlayer cations to layer vacancies.[8-10] In general, it is assumed that protonation occurs for charge balancing, where the charge of an adsorbed cation is insufficient to completely offset the layer charge at a vacancy site.[5] A DFT study investigating Cu^{2+} sorption in birnessite indicated Cu^{2+} sorption complexes formed over a vacancy site were stabilized by protonation of the remaining oxygens not involved with the complexation, i.e. layer oxygens opposite of the coordinated cation.[8] Lanson et al. suggest protonation of these unsaturated layer oxygens occurs during formation via uptake of protons from the acidic reaction solution and that strong hydrogen bonding with interlayer water influences the stacking modes of the layers.[6] A cation exchange study by McKenzie found ~1 mole H^+ released per mole of Me^{2+} (Me = Pb, Cu Mn or Zn) taken up in hexagonal birnessite where the dominant interlayer counter ion was K^+ at pH 4.[11] The study also observed that the total moles of K^+ and H^+ released into solution was nearly equivalent to 2 times the number of moles of Me^{2+} ions taken up into the

interlayers of the birnessite material,[11] supporting assertions that protons contribute to charge compensation when the counter cation is insufficient to completely offset the total negative layer charge.

B. Common Characterization Techniques

Accurate quantification of layer vacancies in these materials is difficult to obtain via conventional techniques, such as Rietveld refinement and/or simulations of X-ray diffraction (XRD) powder patterns. Many types of disorder that are common features of these materials, both natural and synthetic samples, produce similar effects in the resulting XRD pattern for which refinements/simulations are not sensitive enough to uniquely differentiate.[12, 13] Fitting of extended X-ray absorption fine structure (EXAFS) spectra through development of a structural model is another technique commonly used to extract extended structural information such as layer vacancies in manganese oxides. These refinements also struggle with differentiating the impacts of various structural features that manifest in similar ways in the EXAFS spectrum.[14-17] Both techniques employ the use of model constraints based on foreknowledge of the birnessite structure to help improve the accuracy of the refinements, but many studies support their results by correlating the results of multiple analytical techniques.

C. ^{2}H MAS NMR of Birnessite

In this chapter, solid state magic angle spinning nuclear magnetic resonance (MAS NMR) is used to characterize interactions between interlayer crystalline water protons and charge compensating layer protons associated with the manganate layers of a series of synthetic hexagonal birnessites. ^{2}H MAS NMR is used in this study to directly observe the various deuterium environments present in a series of synthesized hexagonal birnessites with increasing amounts of layer vacancies. Samples are deuterated for this study rather than observing protons directly. This is because the ^{2}H nucleus has almost an order of magnitude lower gyromagnetic ratio compared to ^{1}H, thus reducing the broadening effects of dipolar coupling between the observed nuclear spin and the unpaired electron spin density present in the paramagnetic Mn ions. In a study comparing ^{1}H NMR spectra to ^{2}H NMR spectra of paramagnetic compounds by Liu et al., the deuterium spectra were consistently found to have better resolution than the proton spectra, which was attributed to the smaller dipolar coupling interaction between the deuterium nucleus and the electron spins of the paramagnet.[18] In the phyllomanganate system, the

crystalline interlayer water in these materials can be easily differentiated from layer deuterium environments due to the through-bond Fermi-contact interaction imparting a hyperfine shift to the layer environments.

Several Fermi-contact shifted deuterium environments are anticipated. Two layer environments are expected to have similar shift magnitudes: the vacancy deuterium environment is doubly coordinated to manganese via oxygen (H_a in Figure 4.1 a.), as well as some terminal manganese octahedra at the edges (H_b in Figure 4.1 a.). A second environment present at the particle edges is singly coordinated to layer manganese via oxygen (H_c in Figure 4.1 a.) and will, presumably, have a shift that is roughly half that of the vacancy deuteron environment and the doubly coordinated edge deuteron environment.

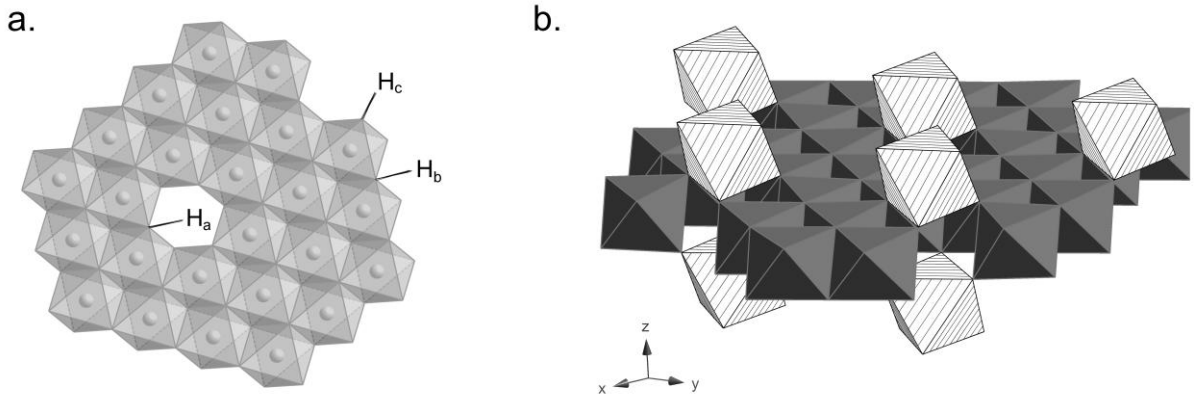

Figure 4.1 (a) The deuterium environments expected to produce a large Femi-contact hyperfine shift in hexagonal birnessite. Vacancy deuterons (H_a) are bonded to oxygens doubly coordinated to manganese. Two types of edge deuterons are possibly present in these materials – deuterons bonded to two manganese via layer oxygen (H_b) and deuterons bonded to a single manganese via layer oxygen (H_c). (b) A single layer of the mineral, chalcophanite, a manganese oxide similar to birnessite. One out of every seven layer manganese ions is vacant in chalcophanite, and vacancies are capped above and below the layer with octahedrally coordinated zinc ions.[3]

This investigation first attempts to assign deuterium environments observed in ^{2}H NMR spectra of the synthesized hexagonal birnessite. Identification of the deuterium environment corresponding to layer vacancies is aided by the interpretation of ^{2}H NMR spectra of Zn ion exchanged samples from the sample series, in which the Zn^{2+} ions are expected to displace vacancy protons, as was observed in the previously mentioned McKenzie et al. study. A zinc ion exchanged into the pristine hexagonal birnessite material is expected to cap a layer vacancy in a

similar manner as the zinc present in the well structurally characterized the layered manganese oxide, chalcophanite (Figure 4.1 b.).[3] Once environments are assigned, integration of isotropic peaks in the ultra fast MAS spectra is performed for quantification of the relative changes of layer vacancies in the sample series.

II. Experimental

A. Synthesis

a. Hexagonal Birnessite Vacancy Series Samples

A series of eight hexagonal birnessite samples was prepared using a synthetic method modified from Feng et al.[19, 20] Briefly, a fresh solution of 0.4M $KMnO_4$ was prepared in a round bottomed flask. This solution was brought to reflux in an oil bath. Under vigorous stirring, a solution of concentrated HCl diluted in 15mL de-ionized water was added dropwise to the $KMnO_4$ solution. The amount of concentrated HCl used was increased from 5.25mL to 17.5mL across the sample series labeled No.1 through No. 8. The reaction mixture was refluxed another 30 minutes and then aged overnight at 60°C. The resulting black/brown precipitate was filtered, washed with copious amounts of de-ionized water and dried at room temperature. Samples were deuterated for ^2H NMR by soaking the sample in D_2O in a sealed centrifuge tube stored in a desiccator for 1 – 2 weeks. Samples were then centrifuged, the supernatant removed and dried at room temperature under vacuum for at least 48 hours. Samples were labeled No. 1 through No. 8, the amount of acid used in the synthesis increasing from No. 1 to No. 8. The sample series was presumed to have differing concentrations of layer vacancies from sample No.1, assumed to be low vacancy concentration, to sample No.8, assumed to be highest vacancy concentration because the amount of disproportionation of layer Mn^{3+} occurring in the synthesis of each sample is expected to increase as the quantity of hydrochloric acid added to the reaction mixture is increased from sample No. 1 to sample No. 8.

b. Zn^{2+} Ion Exchange

Samples No. 2, 4 and No. 7 were chosen for ion exchange with Zn^{2+}. A suspension of 250mg of the pristine material was suspended in 90ml de-ionized water and equilibrated at pH = 6 using dilute solutions of KOH and HCl as needed. Under constant stirring, 3mmol of $ZnCl_2$ was added and the pH of the suspension monitored and maintained using an autotitrator. The

exchange was carried out for 48 hours. Solids were then centrifuged and washed with de-ionized water and air dried. Exchanged materials were then deuterated by soaking the samples in D_2O in a sealed centrifuge tube for 1 – 2 weeks. Samples were centrifuged, the supernatant removed and dried at room temperature for at least 48 hours.

B. Characterization

a. Scanning Electron Microscopy (SEM)

SEM (LEO 1550, Germany) images were collected at 19kV and a 12mm working distance, using a Robinson backscatter detector. The elements were identified using an energy dispersive spectrometer (EDAX and iXRF, USA). Samples were prepped on silicon wafers; Each sample was sonicated in water to form a suspension. A drop of the suspension was placed onto the wafer and allowed to air dry. The silicon wafers were then fixed to sample platforms using copper tape.

b. X-ray Diffraction (XRD)

X-ray diffraction powder patterns of each sample were collected using a Rigaku Miniflex Diffractometer (Cr Kα radiation, $\lambda = 2.29$Å). A step scan of 0.2°, 2θ, was used for all samples with a scan speed of 0.5°/min. Diffraction patterns were matched to the JCPDS pattern cards in the diffraction pattern library of the JADE v9.1.1 pattern processing program (Materials Data, Inc.). Selected peak fitting was performed using the peak profile fitting feature of the JADE v9.1.1 pattern processing program. A linear background subtraction was used and the reflection was fit with a pseudo-voigt function.

c. Laser Light Scattering Particle Size Measurements

Light scattering particle size measurements were taken using a Brookhaven Instruments Corp. instrument operating with ZetaPlus Particle Sizing Software, Version 4.10. Measurements were taken of sonicated water suspensions of each sample.

d. Energy Dispersive X-ray Spectroscopy (EDS)

Energy Dispersive X-ray Spectroscopy (EDS) element mapping of Zn^{2+} ion exchanged samples was performed to confirm intercalation of the zinc into the interlayers of the pristine materials. SEM and EDS characterizations were carried out using a Helio Nanolab 600 dualbeam SEM/FIB (FEI Inc.) equipped with EDS function. The EDS system (Oxford Instruments) has an INCAPentalFET Si(Li) detector and the data were processed with the associated INCA program. The excitation energy was varied between 5kV and 20kV.

e. Elemental Analysis and Thermogravimetric Analysis

Elemental analyses of pristine and zinc exchanged materials were performed using flame atomic absorption spectroscopy (AAS) by the Analytical Lab, Marine Science Institute at the University of Santa Barbara. Thermogravimetric data was collected from room temperature to 400°C at a rate of 5°C/min under nitrogen flow using a TA TGA Q500 instrument. Interlayer water content was calculated from the total mass loss from the temperature range of 80 - 200°C which was selected from the reported dehydration temperatures for birnessites with different interlayer counter ions in Johnson and Post (2006).[21]

f. ^{2}H MAS NMR

Room temperature ^{2}H MAS NMR experiments were performed at 55.2MHz on a Bruker 360 spectrometer in a field of 8.4T using a 1.8mm MAS probe built by A. Samoson and coworkers (NICFB, Tallinn, Estonia), at rotor spinning speeds (ν_r) of 30kHz. Low temperature MAS experiments were performed on a Varian 360 spectrometer using a 4mm HX T3 MAS probe, with spinning speeds of 12-15kHz. Ultra fast MAS low temperature experiments were performed on a Bruker spectrometer, 8.4T field strength, using the same 1.8mm MAS probe built by A. Samoson and co-workers. A rotor synchronized spin-echo pulse sequence (90°-τ-180°-τ_1-acquisition) was used with typical 90° pulses of 2μs and 5.125μs, for the 1.8mm and 4mm probe, respectively. Evolution periods were $\tau = n/\nu_r$, where n = 1, 2, and $\tau_1 = \tau$-20μs. Deuterium oxide was used as a reference at 4.8ppm.

g. Deconvolution, Intensity Integration and Quantification

To allow for quantitative analyses via "spin counting", all low temperature ultra fast MAS spectra were taken under the same experimental parameters, and are normalized for sample

weight and number of scans. A deuterium "model compound" of known chemical formula was run under the same experimental conditions (temperature and spinning speed). For these experiments, the deuterated polymer $(CD_2O)_n$, paraformaldehyde-*d2* was used, and the intensity per scan per mole of deuterium was determined from this model compound spectrum.

The broad baseline component was removed from the hexagonal birnessite spectra. Spectral FIDs were zero filled to ensure an integer number of sampling points and cropped into sections with a spectral width equivalent to the spinning speed of 40kHz. These sections were folded onto the centerband section and the intensities summed. The software DMfit was used to deconvolute spectra using a model containing 3 peaks initially centered at approximate peak positions observed in the spectra.[22] Peak positions, intensities and lineshapes (Gaussian and Lorentzian) were floated in the fits. The analytical integrals of the fitted peaks were used to represent the absolute intensities of the different environments. The integration of the deuterium model compound used for spin counting was performed in a similar manner, again using the DMfit software,[22] but fitting each sideband separately to ensure the best fit.

III. Results

A. SEM

SEM images, collected with an Inlens detector show large particle agglomerations despite extensive sonication of samples prior to mounting on silicon wafers (Figure 4.2). The particle sizes do not appear to be mono-dispersed, though the particle size dispersion appears similar for all samples in the series. The presence of a second needle-like morphology in samples No. 6 and No. 8 indicates an unidentified impurity, likely to be the tunnel structured manganese oxide, cryptomelane (α-MnO_2) discussed previously in Chapters 1 and 2, in which synthetic methods use K^+ as a template cation to form the 2x2 tunnel structure.[23, 24] Images of sample No. 6 were also collected using a 50:50 mix of Inlens and SE2 detectors to obtain better textural resolution of the impurity. Due to the presence of this impurity, samples No. 6 and No. 8 are omitted from further analysis. All other samples were scrutinized carefully to ensure this impurity was not present. Only samples No. 1 through No. 5 and sample No.7, determined to be phase pure, will be discussed further in this work.

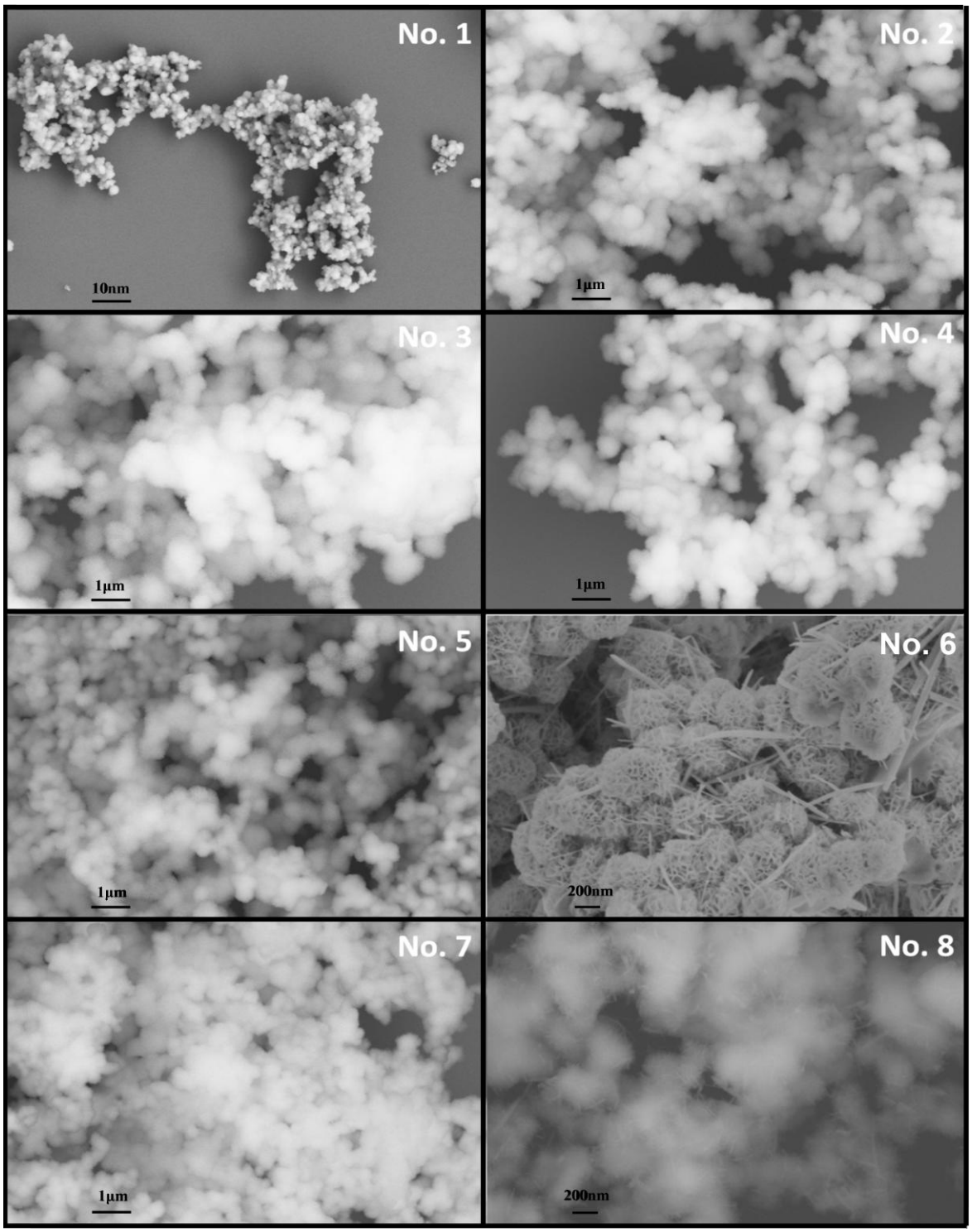

Figure 4.2 SEM images of samples No. 1 through No. 8. Sample No. 1 is shown at a magnification of 3K to illustrate the particle agglomerations. Samples No.2 through 5 and No. 7 are shown at a magnification of 30K. Particle sizes are clearly not mono-dispersed, but appear to fall within a range of less than 1µm. Samples No. 6 and No. 8 are shown at a magnification of 100K to illustrate the presence of the needle-like morphology impurity.

B. XRD

X-ray diffraction shows samples No. 1 through No. 5 and No. 7 to be layered birnessites. Peak reflections of the powder patterns have relatively weak intensities with significant broadening, consistent with a turbostratically stacked hexagonal birnessite.[12] For each sample, the width of the 001 reflection (corresponding to the interlayer spacing) was selected in the XRD pattern as a rough measure of the particle thickness using the peak profile fitting feature of the JADE v9.1.1 pattern processing program. The average particle thickness in the series is 51Å. The decrease in intensity of the 001 reflection observed in samples No. 5 and No. 7 is attributed to the slightly smaller estimated average particle thickness, *ca*. 48 and 43Å, respectively.

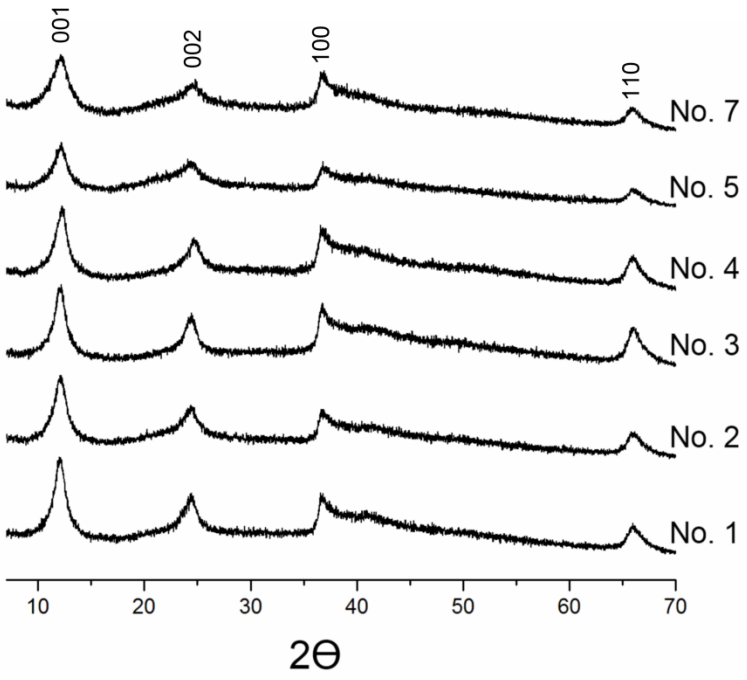

Figure 4.3 X-ray diffraction powder patterns of samples No. 1 through No.5 and No. 7 indicate turbostratically stacked layers of hexagonal birnessite. The indices of the characteristic reflections are labeled.

C. Laser Light Scattering Particle Size Measurements

Light scattering particle size measurements indicate that the samples are not mono-dispersed, but rather fall in a range of particle sizes from 250-600nm (Table 4.1). The

measurements also indicate the presence of 1.5 micron and 7-10 micron particle sizes, which are attributed to the agglomerates of the smaller particles observed in the SEM images.

Table 4.1 Laser light scattering measurements. Particle sizes fall within a 250-600nm range. The reported particle sizes of 1 micron or larger are attributed to particle agglomerations.

Sample	Particle Size Range (nm)	Sample	Particle Size Range (nm)
1	**622 – 924** **8220 – 10000**	**4**	**431 – 604** **1059 – 1326** **7989 – 10000**
2	**349 – 564** **1869 – 2677** **7869 – 10000**	**5**	**283 – 471** **2170 – 3180** **7752 – 10000**
3	**461 – 575** **895 – 1384** **8027 – 10000**	**7**	**382 – 609** **1378 – 2196** **7920 – 10000**

D. EDS

To confirm intercalation of Zn^{2+} ions into the interlayers of the ion exchanged materials, EDS was performed to map the Mn, O and Zn distributions (Figures 4.4 To 4.6). The elemental mapping shows an even distribution of zinc in the particles relative to manganese and oxygen, indicating the Zn^{2+} ions have been exchanged into the interlayers of samples No. 2, No. 4 and No. 7.

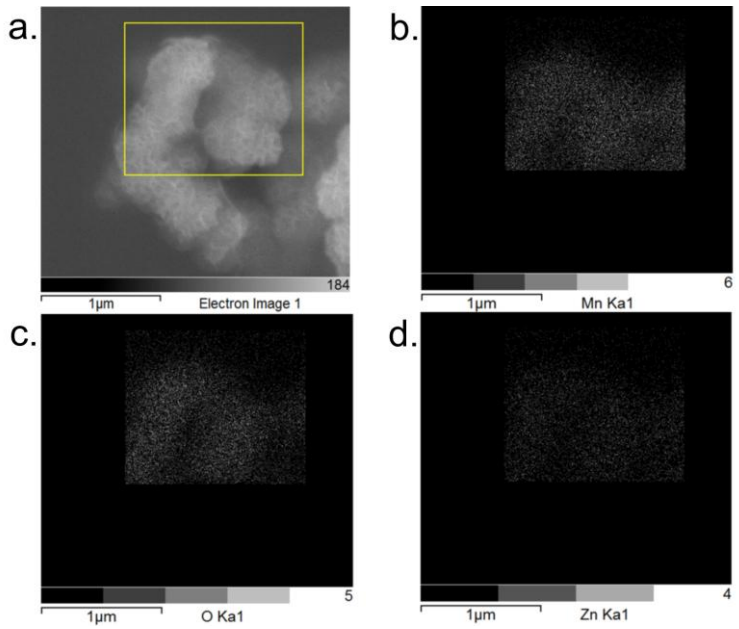

Figure 4.4 EDS element mapping images of the Zn^{2+} ion exchanged No. 2 material. (a) Image of the mapped particles (b) EDS elemental mapping of manganese (c) oxygen and (d) zinc in the particles.

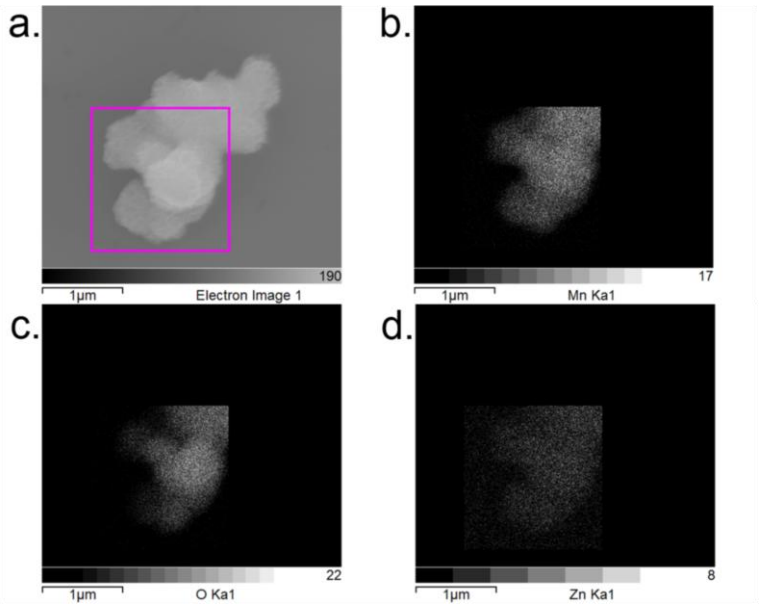

Figure 4.5 EDS element mapping images of the Zn^{2+} ion exchanged No. 4 material. (a) Image of the mapped particles (b) EDS elemental mapping of manganese (c) oxygen and (d) zinc in the particles.

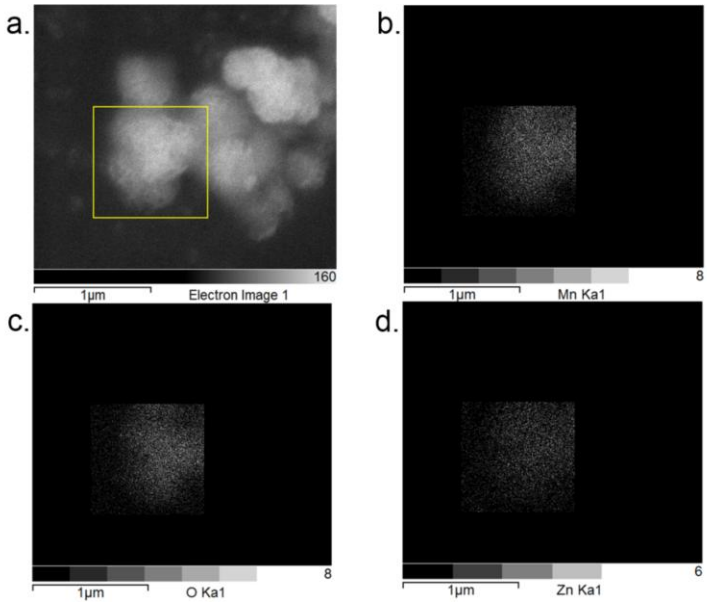

Figure 4.6 Energy EDS element mapping images of the Zn^{2+} ion exchanged No. 7 material. (a) Image of the mapped particles (b) EDS elemental mapping of manganese (c) oxygen and (d) zinc in the particles.

E. Elemental Analysis and TGA

Elemental analyses of the pristine materials shows a slight decrease of potassium content across the sample series (Table 4.2). While this is initially counterintuitive for increasing layer vacancy concentration, comparison of the K:Mn ratios with that of the pH of the reaction mixture suggest that, as the pH drops in the reaction mixture, protons likely become increasingly competitive with potassium ions for charge compensation. Calculated water content from TGA curves indicate that interlayer water content does not vary significantly in the sample series (Table 4.2).

Table 4.2 Elemental analysis results for potassium and manganese content in pristine vacancy series materials and the corresponding pH of synthesis reaction mixtures and results of water content from TGA data.

Sample	mol K^+/ mg sample	mol Mn/ mg sample	ratio K:Mn	pH of reaction mixture	Water content (mol H_2O/ mg sample)
1	**$1.82x10^{-6}$**	**$8.26x10^{-6}$**	**0.22**	**6.7**	**$6.36x10^{-6}$**
2	**$1.98x10^{-6}$**	**$8.50x10^{-6}$**	**0.23**	**6.4**	**$6.28x10^{-6}$**
3	**$1.93x10^{-6}$**	**$8.07x10^{-6}$**	**0.23**	**7.9**	**$7.12 x10^{-6}$**
4	**$1.92x10^{-6}$**	**$8.40x10^{-6}$**	**0.22**	**6.3**	**$7.36 x10^{-6}$**
5	**$1.65x10^{-6}$**	**$8.37x10^{-6}$**	**0.19**	**3.0**	**$7.04 x10^{-6}$**
7	**$1.19x10^{-6}$**	**$8.46x10^{-6}$**	**0.14**	**1.1**	**$6.83 x10^{-6}$**

F. ^{2}H MAS NMR

a. Room Temperature NMR

Room temperature ^{2}H NMR spectra were collected of samples No. 1 – 5 and No. 7 (Figure 4.7). These spectra exhibit a single deuterium environment, the shift of this environment appearing to increase across the sample series. The NMR spectrum of sample No. 1 (assumed lowest concentration of layer vacancies) has a shift at 4ppm, compared to the spectrum of sample No. 7 (assumed to have the greatest concentration of layer vacancies) with a shift at 42ppm. Intermediate samples, No. 2, 3, 4 and 5 exhibit shifts at 20, 22, 27 and 30ppm, respectively.

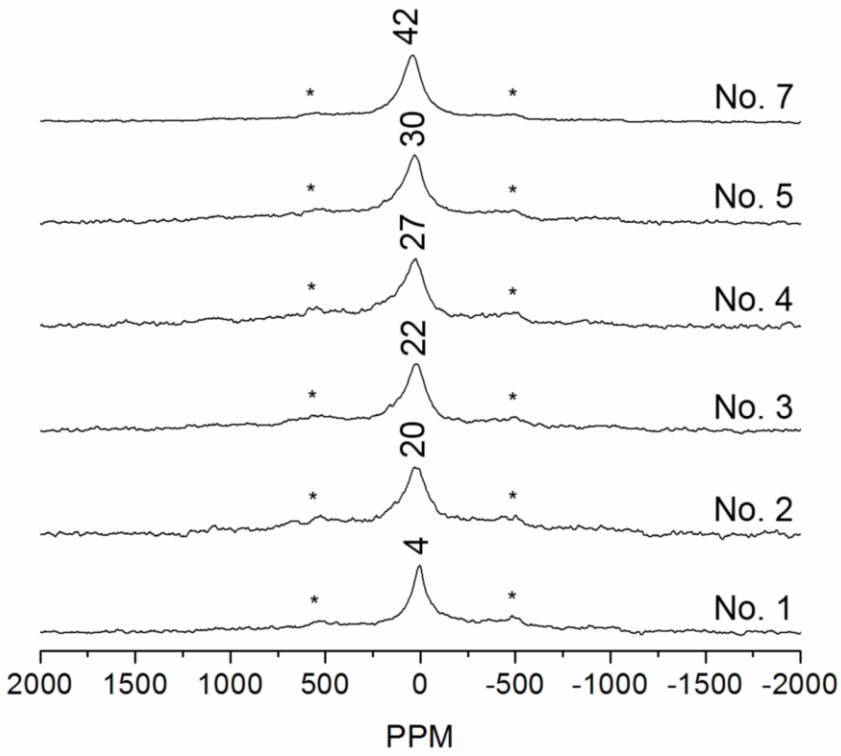

Figure 4.7 ^{2}H NMR spectra of vacancy series samples. All spectra collected at 295K with a spinning speed of 30kHz. Spectra are normalized for sample weight and number of scans. Spinning sidebands are indicated with an asterisk '*'.

b. Low Temperature NMR

The low temperature ^{2}H NMR spectra acquired with spinning speeds of 12 to 14kHz have at least two distinct deuterium environments at around 2 - 4ppm and 120 - 133ppm (Figure 4.8 and the isotropic region in Figure 4.9). The resonance at 2 - 4ppm is attributed to a diamagnetic interlayer water deuterium environment, whereas the resonance at 120 - 133ppm is attributed to a paramagnetic environment, likely deuterons associated with layer vacancies. The assignment of the larger shift is supported by the qualitative observation that the intensity of this peak appears to increase with the expected increase in layer vacancies from sample No. 1 to No.5 and No. 7. Vacancy deuterons are bonded to two manganese ions via layer oxygen (Figure 4.1). A hyperfine-shifted shoulder at 50 – 66ppm is also present in these spectra, suggesting a second paramagnetic environment. A broad baseline feature is also present in all spectra, which may be

intensity from a structural feature of these materials, or due to incomplete resolution of individual spinning sidebands.

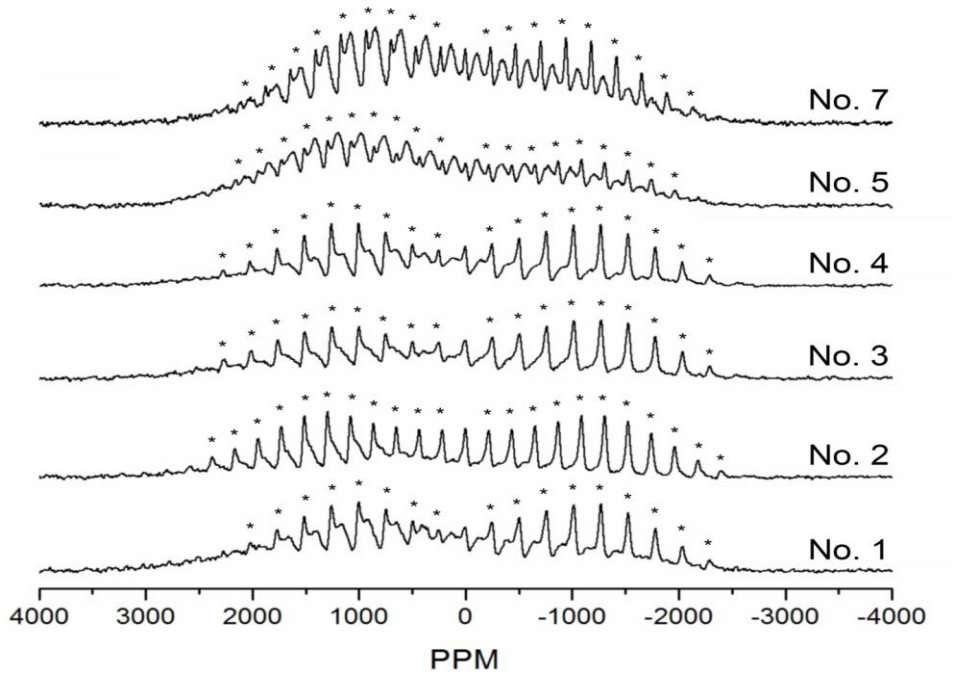

Figure 4.8 ^{2}H NMR spectra of vacancy series samples. All spectra collected at 170K with a spinning speed of 12-14kHz. Spectra are normalized for number of scans but not sample weight. Groups of spinning sidebands are indicated with an asterisk '*'.

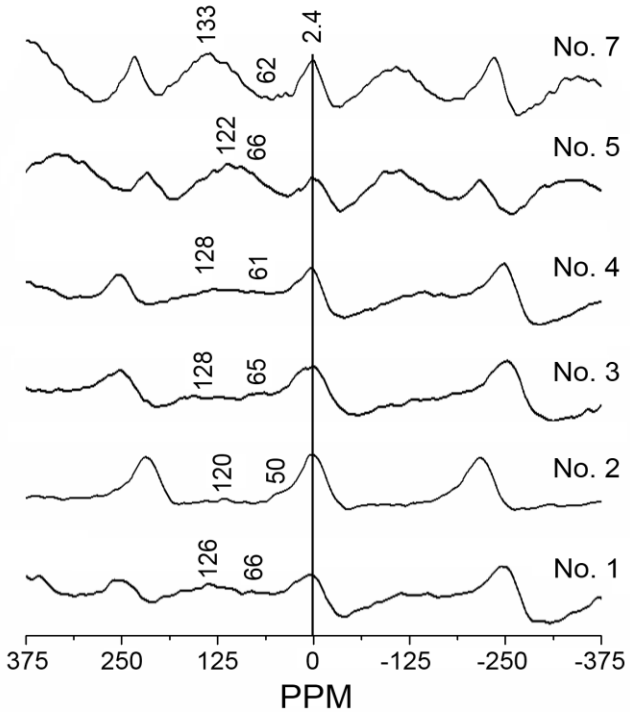

Figure 4.9 The isotropic region of the low temperature ^{2}H NMR spectra from Figure 4.8.

c. Low Temperature NMR of Zn^{2+} Exchanged Materials

Deuteration and subsequent ^{2}H NMR of the No. 2 and No. 7 Zn^{2+} exchanged materials do show a notable decrease in the peak at 120 - 133ppm (Figure 4.10), confirming displacement of these deuterons by the uptake and coordination of Zn^{2+} cations over layer vacancies and indicating they are in fact, vacancy deuterons. A ^{2}H NMR spectrum of the Zn^{2+} exchanged No. 4 material could not be obtained due to an insufficient amount of sample recovered from the exchange experiment. In the spectra of the exchanged materials (Figure 4.10 b. and d.), minimal intensity is observed for the 120 - 133ppm environment identified in the corresponding pristine material (Figure 4.10 a. and c.). A slight shoulder at 56 - 59ppm is also observed in the spectra of the exchanged material, similar to that observed in the pristine materials.

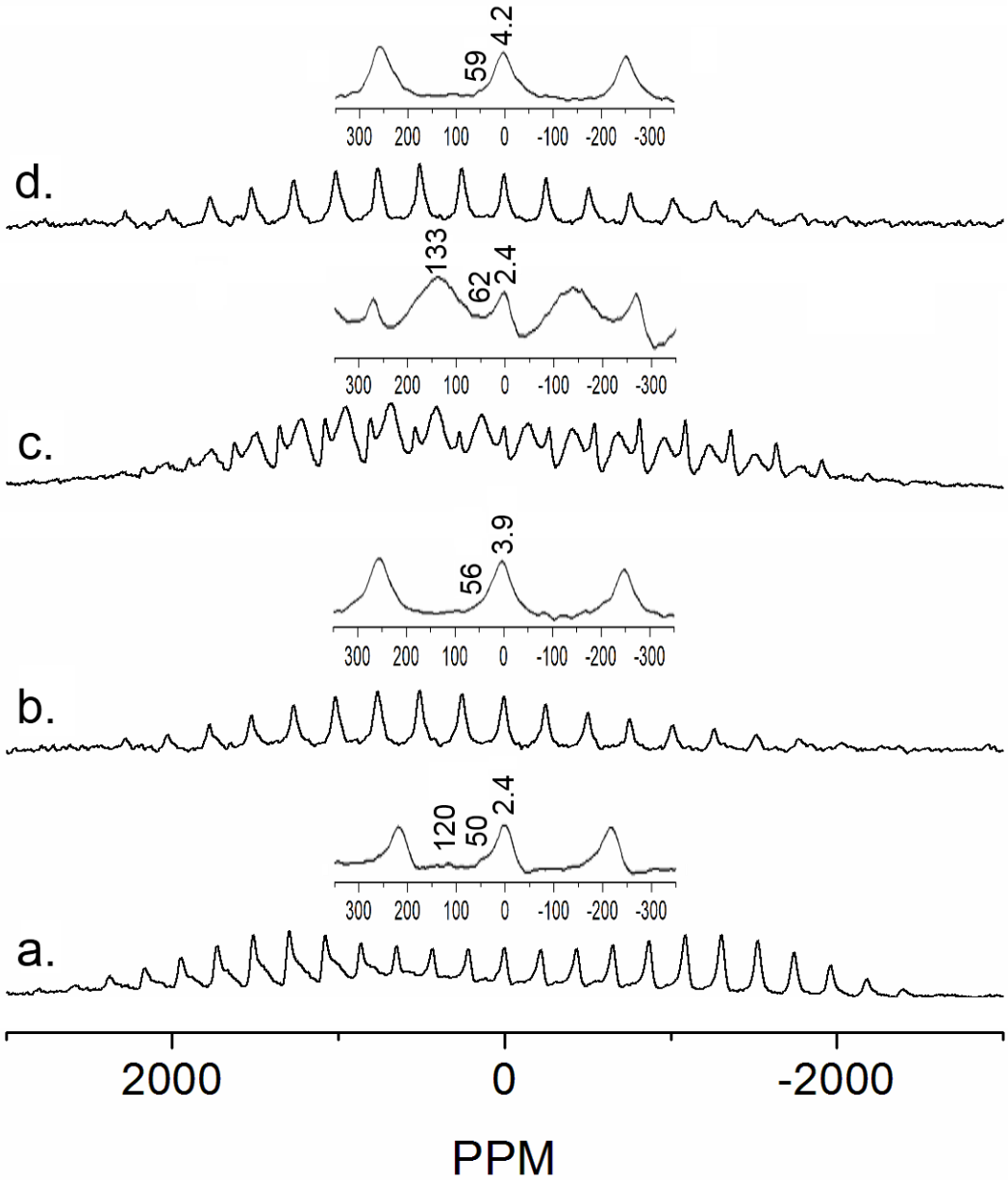

Figure 4.10 Low temperature ^{2}H NMR of pristine and Zn^{2+} ion exchanged material. (a) pristine No. 2 material (b) Zn exchanged No. 2 (c) pristine No. 7 material (d) Zn exchanged No. 7. Spectra were collected at 170K with a spinning speed of 12kHz. Insets above spectra show isotropic resonances.

Elemental analysis of the exchanged samples indicates the total potassium and zinc content relative to the manganese content is similar for all the samples, despite differing layer vacancy content (Table 4.3). It is also important to note the concentrations of manganese in the

supernatant of the exchange reaction, which can be a measure of the significance of interlayer Mn^{2+} present in the samples. The amount of manganese in the No. 2 Zn exchange supernatant was below detection limits. The No. 4 Zn exchange supernatant was only just above detection limits and, assuming the manganese present in solution is due to displacement from the interlayers of the pristine material during exchange, correlates to $7.1x10^{-8}$mol Mn per mg sample present as interlayer Mn counter ions. The Mn content in the supernatant of the Zn exchanged No. 7 material was noticeably higher, corresponding to a total of $2.52x10^{-7}$mol Mn per mg sample present as interlayer Mn counter ions. The minor amounts of manganese present in the supernatants of the exchanged samples suggests there is negligible amounts of charge compensating interlayer Mn^{2+} for samples No. 2 and No. 4, but that the charge compensation of Mn^{2+} may need to be taken into consideration for sample No. 7.

Table 4.3 Elemental analyses of zinc exchanged samples No. 2, No. 4 and No. 7 and the supernatant solutions.

Sample	mol K^+/mg exchanged sample	mol Zn/mg exchanged sample	K+Zn:Mn	mol Mn/L in exchange supernatant
Exch. No. 2	**$4.69x10^{-7}$**	**$1.71x10^{-6}$**	**0.29**	**$<1.1x10^{-7}$**
Exch. No. 4	**$4.49x10^{-7}$**	**$1.80x10^{-6}$**	**0.29**	**$1.82x10^{-7}$**
Exch. No. 7	**$3.25x10^{-7}$**	**$1.74x10^{-6}$**	**0.28**	**$6.37x10^{-5}$**

d. Ultra Fast MAS Low Temperature NMR of Pristine Materials

Faster spinning speeds were required to attain separation of spinning sidebands from the central transitions. However, frictional heating from spinning the rotor can be problematic for maintaining the actual sample temperature sufficiently low to freeze the exchange in these materials. A cryostat probe enabled spinning speeds of 40kHz while keeping the sample temperature low (estimated to be only 10-15 degrees above 170K, the temperature at which the data was collected) (Figure 4.11 and the isotropic region in Figure 4.12).

The broad baseline intensity, previously noted and tentatively attributed to incomplete separation of spinning sidebands, is still present in these faster spinning low temperature spectra. Increasing the echo pulse sequence τ delays by multiple rotor periods show uniform reduction of spectral intensities for the sharper isotropic resonances as well as the broad feature, indicating

the broad component has similar T_2 relaxation times to that of the other confirmed deuterium environments. These observations indicate that this broad feature is from a structural component of these materials rather than spectral artifacts from the tails of rf pulses (probe ringing), and therefore represents another deuterium environment.

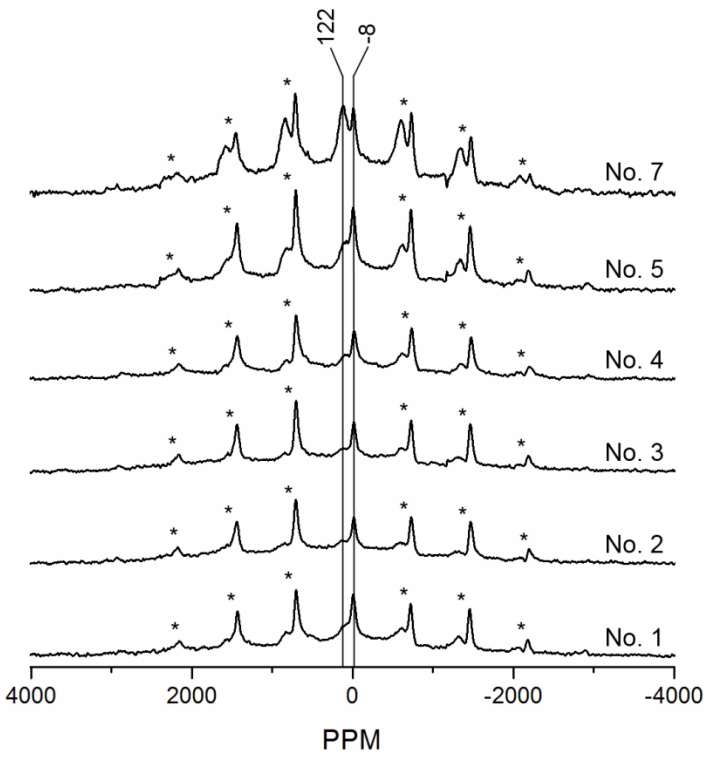

Figure 4.11 ^{2}H NMR of vacancy series samples. Spectra collected at 170K with a spinning speed of 40kHz. The shifts (in ppm) are indicated for the main isotropic resonances and represent an average shift for all spectra. Spinning sidebands are marked with an asterisk '*'.

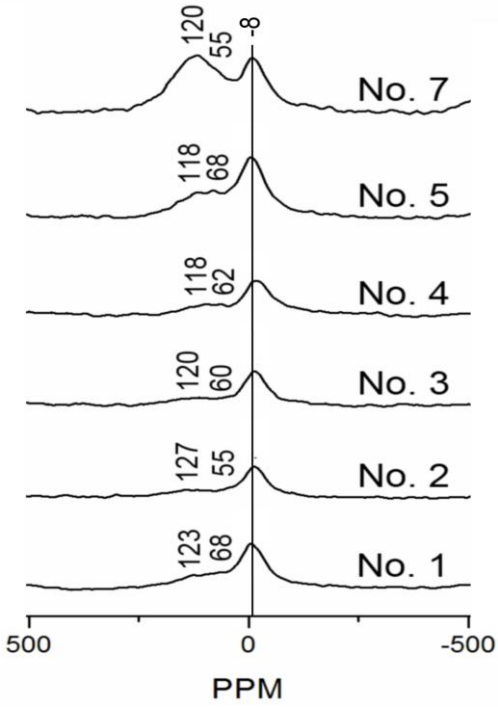

Figure 4.12 The isotropic region of the low temperature ^{2}H NMR spectra from Figure 4.11.

G. Intensity Integration of Ultra Fast MAS Spectra for Vacancy Quantification

In order to quantify vacancies by deconvolution and integration of the low temperature ultra fast MAS spectra (Figure 4.10), assumptions as to the composition of interlayer counter ions are required. Mn^{2+} ions are not expected to be readily available in the reaction mixture, except for any present due to disproportionation of layer Mn^{3+}. The elemental analyses of the supernatant solutions from the Zn ion exchanged No. 2 and No. 4 samples indicate negligible amounts of manganese released into solution from the exchange. Therefore, it would be a reasonable to assume no interlayer manganese counter ions for these samples. However, there was a notably greater amount of Mn detected in the supernatant (Table 4.3) of the zinc exchanged No. 7 sample that should be addressed for how significantly it may impact the results of spin counting. Assuming this aqueous manganese originated in the pristine material as interlayer counter ions, and is therefore included in the total Mn reported in Table 4.2, this manganese accounts for only about 3% of the total manganese content in the pristine No. 7 sample. Therefore, the presence of this small amount of interlayer manganese will be ignored in order to treat the integration of the low temperature spectra of all the samples in a similar manner. Consequently, the dominant counter ions in these materials that will be considered for charge compensation are K^+ and protons.

Elemental analysis of K and Mn content of the pristine materials indicates the K^+ content decreases across the series with increasing vacancy concentration, suggesting that proton compensation becomes increasingly dominant in the samples with higher vacancy concentration (Table 4.2). So, for every Mn^{4+} vacancy in the layer (assuming isolated vacancies), a 4+ charge compensation is expected from a combination of K^+ and protons.

The integration and "spin counting" of the acquired low temperature spectra (Figure 4.10) also requires estimates. The second hyperfine-shifted environment observed in spectra at 55 - 68ppm is assigned to edge deuterons, and is not well enough resolved in the NMR spectra to accurately separate the intensity from this environment from the intensity from the vacancy environment. These two overlapping environments are therefore treated as a single peak for integration purposes. Spectra are normalized for number of scans and sample weight, and spinning sideband intensities are folded in on the centerband for integration. A deuterium "model compound" with known molecular weight is run under the same experimental conditions that all

the other spectra were collected. The spectrum of the model compound used for normalization, the deuterated polymer $(CD_2O)_n$, paraformaldehyde-*d2*, allows the calculation of the intensity per scan per mole of deuterium. This normalizing factor is then applied to all the sample spectra to calculate the number of moles of deuterium per mg sample (Table 4.4).

Table 4.4 Calculated moles of deuterium for the vacancy and edge deuterium environments from the spin counting integration of low temperature ultra fast MAS NMR spectra. Potassium content from elemental analysis is included again for easy reference.

Sample	Mol ^2H in "vacancy"/ mg sample (N_{2H})	Mol K^+/mg sample (N_{K^+})
1	**$6.99x10^{-7}$**	**$1.82x10^{-6}$**
2	**$2.68x10^{-7}$**	**$1.98 x10^{-6}$**
3	**$3.75x10^{-7}$**	**$1.93 x10^{-6}$**
4	**$5.46x10^{-7}$**	**$1.92 x10^{-6}$**
5	**$1.09x10^{-6}$**	**$1.65 x10^{-6}$**
7	**$2.58x10^{-6}$**	**$1.20 x10^{-6}$**

Comparison of the calculated moles of "vacancy" deuterium per mg of sample in Table 4.4 indicate that the moles of K^+ varies from 2.6 times greater (sample No. 1) to only ½ of the calculated number of moles of deuterium (sample No. 7). Under the assumption that potassium charge compensates only vacancies and that each vacancy is charge compensated by two K^+ ions, the moles of "vacancy" deuterium is insufficient to provide the rest of the +4 charge compensation required for per vacancy. However, accounting for the presence of layer Mn^{3+} provides a reasonable explanation for the potassium surplus and deuterium deficiency. Allowing for each vacancy to be charge compensated by two K^+ ions, only two deuterons are necessary to fulfill the required +4 compensation. Therefore, vacancy content can be ascertained via the amount of deuterium available for charge compensation. The number of moles of layer vacancies per mg sample (X_{vac}) will be given by:

$$\mathbf{X_{vac} = (N_{2H})/2}$$

where N_{2H} is the moles "vacancy" deuterium per mg sample (Table 4.4). With two K^+ per vacancy, the amount of K^+ charge compensating layer Mn^{3+} - and therefore the amount of Mn^{3+} present in the layer - ($X_{Mn}{}^{3+}$) would then be given by:

$$\mathbf{X_{Mn}{}^{3+} = N_{K}{}^{+} - 2X_{vac}}$$

where $N_{K}{}^{+}$ is the moles of K^+ per mg of sample, as determined from elemental analysis. The calculated number of moles of layer vacancies per mg sample and the moles of K^+ charge

compensating layer Mn^{3+} are presented in Table 4.5. The value of X_{Mn}^{3+} is negative for sample No. 7 (Table 4.5), indicating that there is little or no layer Mn^{3+}. This is to be expected since the value of N_K^+ less than half of the value of X_{vac} and therefore, all vacancies cannot be charge compensated by two K^+ ions. The percentage of layer vacancies corresponding to the reported values of X'_{vac} were also calculated (reported also in Table 4.5) using the following equation:

$$\% \text{ vac}(X_{vac}) = 100 \times [(X_{vac})/(X_{vac}+N_{Mn})]$$

where N_{Mn} is the moles of Mn in the pristine material, and therefore $X_{vac}+N_{Mn}$ the total moles of manganese in the pristine material in the absence of layer vacancies.

Table 4.5 Calculations of X_{vac} and X_{Mn}^{3+} assuming two K^+ ions charge compensate each layer vacancy.

Sample	X_{vac}	% vac. using X_{vac}	X_{Mn}^{3+}
1	3.49×10^{-7}	4.1	1.12×10^{-6}
2	1.34×10^{-7}	1.6	1.71×10^{-6}
3	1.88×10^{-7}	2.3	1.55×10^{-6}
4	2.73×10^{-7}	3.2	1.37×10^{-6}
5	5.44×10^{-7}	6.1	5.62×10^{-7}
7	1.29×10^{-6}	13.2	-1.38×10^{-6}

However, it may also be assumed that only one K^+ charge compensates some layer vacancies, resulting in three deuterons completing the required 4+ charge compensation. Assuming this charge compensating scheme for all vacancies, then the moles of vacancies per mg sample (X'_{vac}) are calculated by the following equation:

$$X'_{vac} = (N_{2H})/3$$

And then moles of K^+ per mg sample that charge compensate layer Mn^{3+} (X'_{Mn}^{3+}) would be determined by the equation:

$$X'_{Mn}^{3+} = N_K^+ - X'_{vac}$$

The results of these calculations are presented in Table 4.6. The percentage of layer vacancies corresponding to the reported values of X'_{vac} were calculated (reported also in Table 4.6) using the following equation:

$$\%vac(X'_{vac}) = 100 \times [(X'_{vac})/(X'_{vac}+N_{Mn})]$$

where N_{Mn} is the moles of Mn in the pristine material, and therefore $X'_{vac}+N_{Mn}$ the total moles of manganese in the pristine material in the absence of layer vacancies.

Table 4.6 Calculations of X'_{vac} and $X'_{Mn}{}^{3+}$ assuming only one K^+ charge compensates each layer vacancy.

Sample	X'_{vac}	% vac. using X_{vac}	$X'_{Mn}{}^{3+}$
1	**2.33×10^{-7}**	**2.7**	**1.59×10^{-6}**
2	**8.93×10^{-8}**	**1.0**	**1.89×10^{-6}**
3	**1.25×10^{-7}**	**1.5**	**1.81×10^{-6}**
4	**1.82×10^{-7}**	**2.1**	**1.74×10^{-6}**
5	**3.63×10^{-7}**	**4.2**	**1.29×10^{-6}**
7	**8.59×10^{-7}**	**9.2**	**3.40×10^{-7}**

In practice, charge compensation of layer vacancies is likely to occur via some combination of one and two K^+ ions per vacancy, but the calculations of the two charge compensation schemes represent extremes of the possible range in layer vacancy content. These calculations show a trend of increasing layer vacancy content from samples No. 2 to No. 5 and No. 7. Sample No. 1 is clearly an outlier, falling somewhere between sample No. 4 and sample No. 5 with regards to layer vacancy content.

Both cation ordering arrangements (one and two K^+ ions charge compensating each layer vacancy) also allow for commentary on the amount of layer Mn^{3+} present in each compound. X-ray diffraction powder patterns of the samples are consistent with turbostratically stacked hexagonal birnessite (Figure 4.3), taken to indicate the major source of negative layer charge is layer manganese vacancies. However, the birnessite structure is highly variable and birnessites with hexagonal layer symmetry may have some layer Mn^{3+} present, suggesting there is insufficient layer Mn^{3+} in these samples to produce the coordinated Jahn-Teller distortion

observed in triclinic birnessite.[25] Table 4.7 shows the calculated percentage of total manganese consisting of Mn^{3+}, given by the calculated moles of K^+ charge compensating layer Mn^{3+}, assuming one or two K^+ per vacancy.

Table 4.7 The Mn^{3+}:Mn^{4+} ratios determined from calculations of X_{vac} and X'_{vac}.

Sample	% Mn^{3+} assuming X_{vac}	% Mn^{3+} assuming X'_{vac}
1	14%	19%
2	20%	22%
3	19%	22%
4	16%	21%
5	7%	15%
7	–	4%

IV. Discussion

A. Particle sizes and morphology

SEM images isolated impurities in samples No. 6 and No. 8 (Figure 4.2). All samples were checked thoroughly for the presence of this second morphology observed in the SEM images of samples No. 6 and No. 8 (Figure 4.2), but samples No. 1 to No. 5 and No. 7 were found to be phase pure. The impurity was more carefully imaged for sample No. 6 using a mix of detectors for better resolution of the needle-like morphology. While the impurity was not definitively identified, in particular because no noticeable reflections indicating an impurity were observed in the XRD powder patterns, it was assumed to be a 2x2 tunnel structured manganese oxide, cryptomelane; the reaction solution contained K^+ ions in the synthesis of these materials, which is a template cation in the formation of cryptomelane.[26] As such, it was decided these samples should be excluded from this investigation. SEM images of the remaining samples, No.

1 through No. 5 and No. 7 appear to have similar particle size distributions. Further analyses will focus only on these samples, determined to be phase pure.

X-ray diffraction powder patterns of the series samples indicate they are turbostratically stacked hexagonal birnessites (Figure 4.3). Slight decreases in the powder pattern intensities for the 001 and 002 reflections in samples No. 5 and No. 7 suggest fewer layer stackings, which is supported by the estimates provided by the calculated "particle sizes." The sample particles are non-spherical, and so this procedure is a poor estimate of actual particle size. However, if applied to the 001 reflection corresponding to the interlayer spacing, this provides a reasonable gauge for the estimation of the number of layers stacked per particle.

Light scattering measurements also support the observations of the SEM images, that particle size of the sample series is not mono-dispersed. The particle size dispersions of the series samples fall within the range of about 250 – 600nm (Table 4.1). Larger particle size ranges observed in the light scattering measurements are concluded to be agglomerations of particles. Despite considerable sonication of samples prior to measurements, it was difficult to successfully disperse particles thoroughly into an aqueous suspension. The presence of particle agglomerations is confirmed in the SEM images. There were no indications of particle sizes smaller than 250nm.

As was discussed in the introduction to this chapter in regards to the expected deuterium environments in the manganese oxide layer, there are edge environments doubly coordinated to manganese via oxygen (H_b from Figure 4.1 a.). These environments can potentially complicate interpretation of spectra since they will likely overlap with that of the vacancy deuterium environment (H_a from Figure 4.1 a.). Therefore, it would be advantageous to estimate the impact this edge deuterium environment may have on the sought after vacancy deuterium environment. A hexagonally shaped particle with diameter of 400nm was assumed to calculate the number of terminal manganese octahedra relative to the total number of octahedra in a single layer. For a particle of this size, terminal octahedra account for only 0.24% of the total octahedra in a layer, and is not likely to pose a significant problem to the interpretation and quantification of the vacancy environment since these values are 1 to 1.5 orders of magnitude greater.

B. ^{2}H MAS NMR

A minimum of three deuterium environments can be expected for these hexagonal birnessites including an interlayer water environment (around 0.9 - 4.8ppm) and two deuterium environments associated with the manganese oxide layer at vacancies and edges, easily differentiated from the interlayer water by a larger hyperfine shift observed in the NMR spectrum. Previous infrared (IR) spectroscopy studies have also identified the presence of hydroxyl and/or hydronium species in addition to at least one type of structural interlayer water in hexagonal birnessite, further corroborating the presence of multiple deuterium environments.[21] However, a single resonance in the room temperature spectra (Figure 4.7) may be explained by exchange between these possible multiple environments. Increasing layer vacancies, as is expected across the sample series, would result in a larger population of hyperfine-shifted deuteron environments relative to the water deuterium environment. Exchange between the various environments, in addition to an increasingly greater contribution of the hyperfine-shifted deuterium environment, will cause the center of gravity of the exchange averaged peak to shift in the direction of the hyperfine environment to higher ppm values, as is observed. Also in support of site exchange at room temperature is the observation of very few spinning sidebands, indicating mobile –OD groups.[27]

In order to test the hypothesis of exchange between multiple deuterium environments at room temperature, as well as explore the dynamics of the exchange, low temperature ^{2}H NMR experiments at 170K were performed (Figure 4.8). Variances in shifts for each of the isotropic resonances are observed in these spectra, which are attributed to the temperature fluctuations inherent in the experimental conditions under which these spectra were collected. A slight shoulder is present in these spectra at 50 - 66ppm, suggesting the presence of a second hyperfine-shifted environment (Figure 4.9). This second hyperfine environment is roughly half of the 120 - 133ppm environment, which would be consistent with edge deuterons bonded to oxygen that is singly coordinated to manganese (H_c Figure 4.1 a.). However, as was discussed previously, edge environments for the average particle size of 400nm accounts for only ~0.24% of the total Mn octahedra in the layer. Therefore, this second, possible hyperfine shifted environment is likely due to slightly differing vacancy environments. Differing vacancy environments may be achieved by the presence of layer Mn^{3+}, so that vacancy deuterons (doubly coordinated to layer manganese via oxygen) may be coordinated to Mn^{4+} and/or Mn^{3+} via oxygen; the hyperfine shift

from a Mn^{3+}-O-D contact will have a smaller contribution than a Mn^{4+}-O-D contact to the overall Fermi-contact shift. Therefore, this shoulder resonance at 50 - 66ppm is attributed to layer vacancies as well.

To validate the assignment of the 120 - 133ppm peak to vacancy deuterons (Figure 4.8), ion exchange with Zn^{2+} was performed with the pristine materials of sample No. 2, 4, and 7, containing low, medium and high concentration of layer vacancies, respectively. The EDS spectra confirmed intercalation of Zn^{2+} into the materials (Figure 4.4 to 4.6). It has been observed in previous studies that the formation of hexagonal birnessite below pH 5 results in minimal re-uptake of Mn^{2+} from solution into the layers.[6] Elemental analysis of pristine materials, as well as the Zn ion exchanged samples No. 2, 4 and 7 also indicate negligible amounts of interlayer Mn^{2+} counter ions. Following from this, K^+ and protons are expected to be the major counter ions and, upon their exchange with Zn^{2+} ions, significant amounts of layer protons should be displaced. The ^2H NMR spectra of the exchanged materials do exhibit a noticeable decrease of the 120 - 133ppm peak intensity compared to that of the pristine material (Figure 4.10). However some intensity from the 120 - 133ppm peak is may still present due to incomplete ion exchange, as well as overlapping intensity from the edge deuterium environment that is also doubly coordinated to layer Mn via an oxygen anion.

The zinc content for each of the exchanged samples has little variation, in contradiction with the expectation that greater layer vacancies allows greater uptake of zinc into the interlayers (Table 4.3). There is a notable change in the shape of the spinning sideband manifold for the environment corresponding to layer water in the spectrum of the exchanged material compared to that of the pristine material. The shape of the spinning sideband manifold for the sharp water environment in the spectrum of the pristine material is that of the Pake doublet, indicating strongly bound crystalline waters (Figure 4.10 a. and c.).[28, 29] However, the shape of the spinning sideband manifold for this same environment in the exchanged materials has changed drastically. This suggests that the mobility of the interlayer water is changing and may be the result of an increasing presence of H_3O^+ in the exchanged samples, acting as another counter ion species with more mobility than the crystalline waters strongly bound to interlayer cations, as observed in the pristine samples. While it is difficult to differentiate D_2O from D_3O^+ in a ^2H NMR spectrum based on chemical shift,[30] the changing shape of the spinning sideband manifold

suggests an increase in mobility,[31] which may arise from the coordination of the hydronium ion as a counter ion instead of coordination to interlayer cations. Following this trend, the counterintuitive zinc content in the exchanged materials is explained by hydronium ions competing with zinc ions for coordination as a counter ion. In addition to various other competitive counter ions present, it is also important to note that there are several Zn(II) species present at pH = 6, including $Zn_2(OH)^{3+}$, $Zn(OH)_2(aq)$, $ZnOH^+$ in addition to Zn^{2+} ions.[32] Some of these ionic species may be too large to allow intercalation of Zn into the 7Å interlayer spacing, also contributing to the lower values of Zn adsorption into the interlayers.

The spectra collected using ultra fast MAS spinning (Figure 4.11) successfully separate the isotropic resonances from neighboring spinning sidebands. However, the central transitions still overlap and therefore require deconvolution for any attempt to be made at quantifying vacancy deuterons. The peak corresponding to vacancy deuterons has a shift of 118 to 127ppm and the interlayer water peak at -3 to -12 ppm (Figure 4.12). The broad baseline feature, observed in all low temperature spectra, is also identified as yet another deuterium environment and is tentatively assigned as interlayer water deuterons strongly hydrogen bonded to layer oxygen.

Hydrogen bonding between interlayer water and layer oxygen has been discussed in previous studies as important cohesive interactions between the manganese oxide layers, even influencing layer stacking patterns at low pH.[6] Infrared spectroscopy has also been used to investigate interlayer water of birnessite with various interlayer counter ions, identifying two types of interlayer water in some birnessites, and a similar amount of hydrogen bonding between crystalline water and layer oxygen in all birnessite forms.[21] The X-ray diffraction powder patterns of these samples (Figure 4.3) indicate a high degree of stacking faults in these samples, which presumably create significant disorder in the strengths of hydrogen bonding interactions between the interlayer waters and layer oxygen. With evidence of a covalent component to hydrogen bonding,[33, 34] some small Fermi-contact shift may be imparted through stronger hydrogen bonded interlayer waters, further broadening these resonances.

The assignment of the broad environment to interlayer water hydrogen bonded to layer oxygen necessitates more specific definition of the water assigned to the sharp resonance at -3 to -12ppm. This environment, previously attributed to general interlayer waters, is now specified as

interlayer waters strongly bound to interlayer cations. Previous studies of interlayer water in birnessites have suggested that such hydrogen bonding networks between the cation-bound interlayer waters exist in these materials.[6, 7]

C. Intensity Integration for Vacancy Quantification

The integration of the ultra fast MAS spectra show a trend regarding the vacancy environment that is similar to the qualitatively observed trend in the low temperature experiments performed both at 12-14kHz and 40kHz (Figure 4.9 and Figure 4.12). The values obtained from calculations assuming one or two K^+ ions charge compensating layer vacancies in the "spin counted" spectra for the moles of layer vacancies per mg of sample for samples No. 2 through No. 5 and No. 7 confirm the layer vacancy concentrations increase across this sample series (Table 4.5 and 4.6).

The moles of vacancies per mg sample for the No. 1 material indicate it is not the lowest layer vacancy concentration sample, but falls between No. 4 and No. 5 in terms of vacancy concentration (Table 4.5 and Table 4.6). The potassium content of the No. 1 sample, relative to the calculated moles of vacancies per mg sample is also inconsistent with the general trends observed in the rest of the sample series (Table 4.2), however, remains consistent with the observed correlation between potassium content and the pH of the reaction mixture during synthesis. This indicates that the synthesis procedure of these samples may be highly sensitive to a number of conditions other than just the amount of hydrochloric acid added to the reaction mixture. Factors such as stir rate and the rate of addition of reagents can have a significant impact in the resulting material synthesized.[35, 36] Therefore, the data indicating sample No. 1 as an outlier in the sample series suggests a procedural variance in the synthesis of this sample.

The layer Mn^{3+} content for each sample, inferred from the "excess" potassium after charge compensation of layer vacancies was accounted for, suggests that, while the X-ray diffraction powder patterns of each sample is consistent with turbostratically stacked hexagonal birnessite, the lower vacancy concentration samples may fall on the triclinic side of the two extremes of the birnessite structural continuum described in Chapter 1. The percentage Mn^{3+} relative to the total Mn, calculated for the two cation ordering scenarios where one and two K^+ ions charge compensate each layer vacancy, indicate in all cases that the Mn^{3+} layer content is below 22% of layer manganese for all samples (Table 4.7). Jahn-Teller distortions are typically

observed in mixed valence manganese oxides in which there is at least 20-30% Mn^{3+} content.[25] Therefore, since the calculated values of layer Mn^{3+} content for the vacancy series samples are on the lower end of this range for transition to a coordinated Jahn-Teller distortion, it may be below the required amount of Mn^{3+} to produce the coordinated distortion in these materials, maintaining hexagonal layer symmetry.

The presence of Mn^{3+} in the layer of these materials is also supported by the relatively small magnitude of the shift corresponding to layer vacancies (118 – 133ppm) in the low temperature ^2H NMR spectra. Previous work studying the ^2H NMR of various cathode material manganese oxides assigned a deuterium environment at 150ppm to a "Reutschi" defect site. This deuterium environment, while doubly coordinated to Mn^{4+} via an intervening oxygen anion at defect sites in the manganese oxide, EMD, the electrons in the e_g orbitals of the manganese ions surrounding the deuterium environment are delocalized due to the presence of some structural Mn^{3+} ions. This delocalization reduces the efficiency of the superexchange mechanism by which the Fermi-contact interaction imparts a hyperfine shift, and hence, the typical hyperfine shift of 100ppm per Mn^{4+} contact is reduced for the Reutschi defect environment.[27] The magnitude of hyperfine shifts corresponding to deuterium environments that are doubly coordinated to Mn^{4+} via oxygen, where electrons were not delocalized due to the presence of Mn^{3+}, were observed to be notably larger (~350ppm) in work by Paik et al.[27] Therefore, in the case of the hexagonal birnessite sample series, the hyperfine shifts observed for the vacancy deuterium environment indicate that layer Mn^{3+} ions present near vacancies induce some delocalization of electrons surrounding the vacancy deuterium environment, reducing the efficiency of the Fermi-contact interaction. The shoulder observed in low temperature spectra at 50-66ppm can be attributed to vacancy deuterons coordinated to only Mn^{3+} ions.

V. Conclusions

This chapter investigated a series of hexagonal birnessites synthesized with increasing layer vacancies via ^2H MAS NMR. The particle size distributions and morphology were confirmed via SEM and laser light scattering measurements to be consistent across the series of hexagonal birnessites prepared with increasing layer vacancy concentrations in samples No.1 to No. 5 and No.7. Room temperature ^2H NMR spectra of the remaining hexagonal birnessite samples indicate that there is significant exchange between the interlayer water deuterons and charge

compensating layer deuterons. Low temperature ^{2}H NMR spectra of samples No. 1 through No. 5 and No. 7 freeze this exchange and allow resolution of multiple environments, including a sharp peak assigned to crystalline waters strongly coordinated to interlayer K^{+}, and two broader environments, a shoulder at 50 - 66ppm and a more well defined peak at 120 - 133ppm, attributed to deuterons doubly coordinated to manganese (both Mn^{3+} and Mn^{4+}) via oxygen at layer vacancy sites. The assignment of the 120 - 133ppm peak to layer vacancies is supported by the notable decrease in intensity for this environment in the low temperature ^{2}H NMR spectra of the Zn^{2+} ion exchanged samples. Low zinc uptake into samples, despite increasing layer vacancies is likely due to the increasing presence of more mobile H_3O^{+} ions in the interlayers, coordinating with the layer as another counter ion species. Low temperature ultra fast MAS experiments allowed separation of the spinning sideband manifold from the isotropic resonances, also confirming that the broad baseline intensity observed in all low temperature spectra was structural. The baseline intensity is ascribed to interlayer water deuterons that are strongly hydrogen bonded to layer oxygen. Elemental analyses of pristine and Zn ion exchanged materials allow for the assumptions that K^{+} and protons are the major counter ions present in the interlayers. Integration and spin counting of the ultra fast MAS spectra allow the determination of the number of moles of vacancies per mg of sample, confirming a trend of increasing layer vacancies in these samples, with sample No. 1 being an outlier that falls between sample No. 4 and No. 5 in regards to layer vacancy concentration. The large potassium content from elemental analysis, and relatively small deuterium content from integrated spectra of the pristine materials indicates that potassium may also charge compensate some layer Mn^{3+}. The amount of Mn^{3+} present in the pristine materials from calculations is less than 22% of the total manganese content for all samples, and is unlikely to produce a coordinated Jahn-Teller distortion, consistent with the hexagonal layer symmetry observed in the XRD patterns. The presence of Mn^{3+} in the layer near vacancy sites is also consistent with the small magnitudes of the hyperfine shift of the vacancy deuterium environment, suggesting that e_g electrons of the surrounding Mn ions are delocalized and reduce the efficiency of the Fermi-contact interaction for this environment.

VI. References

1. Kuma, K., Usui, A., Paplawsky, W., Gedulin, B., Arrhenius, G., *Mineral Mag* **58**, 425-447 (1994).

2. Drits, V. A., Silvester, E., Gorshkov, A. I., Manceau, A., *Am. Mineral.* **82**, 946-961 (1997).

3. Post, J. E., Appleman, D. E., *Am. Mineral.* **73**, 1401-1404 (1988).

4. Giovanoli, R., Stahli, E., Feitknecht, W., *Helv. Chim. Acta* **53**, 209-220 (1970a).

5. Silvester, E., Manceau, A., Drits, V. A., *Am. Mineral.* **82**, 962-978 (1997).

6. Lanson, B., Drits, V. A., Silvester, E., Manceau, A., *Am. Mineral.* **85**, 826-838 (2000).

7. Lanson, B., Drits, V. A., Feng, Q., Manceau, A., *Am. Mineral.* **87**, 1662-1671 (2002).

8. Sherman, D. M., Peacock, C. L., *Geochem. Cosmochim. Ac.* **74**, 6721-6730 (2010).

9. Toner, B., Manceau, A., Webb, S. M., Sposito, G., *Geochim. Cosmochim. Acta* **70**, 27-43 (2006).

10. Lanson, B., Drits, V. A., Gaillot, A. C., Silvester, E., Plancon, A., Manceau, A., *Am. Mineral.* **87**, 1631-1645 (2002).

11. Mckenzie, R. M., *Geochim. Cosmochim. Acta* **43**, 1855-1857 (1979).

12. Drits, V. A., Lanson, B., Gaillot, A. C., *Am. Mineral.* **92**, 771-788 (2007).

13. Pecharsky, V. K., Zavalij, P. Y., *Fundamentals of Powder Diffraction and Structural Characterizatin of Materials*. (Springer, New York, 2005), pp. 713.

14. Webb, S. M., Tebo, B. M., Bargar, J. R., *Am. Mineral.* **90**, 1342-1357 (2005).

15. Webb, S. M., Tebo, B. M., Bargar, J. R., *Geomicrobiol. J.* **22**, 181-193 (2005).

16. Ressler, T., Brock, S. L., Wong, J., Suib, S. L., *J. Phys. Chem. B* **103**, 6407-6420 (1999).

17. Villalobos, M., Lanson, B., Manceau, A., Toner, B., Sposito, G., *Am. Mineral.* **91**, 489-502 (2007).

18. Liu, K., Ryan, D., Nakanishi, K., McDermott, A., *J. Am. Chem. Soc.* **117**, 6897-6906 (1995).

19. Feng, X. H., Zhai, L. M., Tan, W. F., Liu, F., He, J. Z., *Environ. Pollut.* **147**, 366-373 (2007).

20. Feng, X. H., Ginder-Vogel, M., Zhu, M. Q., Sparks, D., *Abstr Pap Am Chem S* **236**, 47-GEOC (2008).

21. Johnson, E. A., Post, J. E., *Am. Mineral.* **91**, 609-618 (2006).

22. Massiot, D., Fayon, F., Capron, M., King, I., Le Calve, S., Alonso, B., Durand, J. O., Bujoli, B., Gan, Z. H., Hoatson, G., *Magn. Reson. Chem.* **40**, 70-76 (2002).

23. Tian, H., He, J. H., Zhang, X. D., Zhou, L., Wang, D. H., *Microporous Mesoporous Mat.* **138**, 118-122 (2011).

24. Mckenzie, R. M., *Mineral Mag* **38**, 493-& (1971).

25. Rogers, D. B., Germann, R. W., Arnott, R. J., *J. Appl. Phys.* **36**, 2338-2343 (1965).

26. Frias, D., Nousir, S., Barrio, I., Montes, M., Lopez, T., Centeno, M. A., Odriozola, J. A., *Mater. Charact.* **58**, 776-781 (2007).

27. Paik, Y., Osegovic, J. P., Wang, F., Bowden, W., Grey, C. P., *J. Am. Chem. Soc.* **123**, 9367-9377 (2001).

28. Kim, J., Nielsen, U. G., Grey, C. P., *J. Am. Chem. Soc.* **130**, 1285-1295 (2008).

29. Hauch, A., Bildsoe, H., Jakobsen, H. J., Skibsted, J., *J. Magn. Reson.* **165**, 282-292 (2003).

30. Nielsen, U. G., Majzlan, J., Grey, C. P., *Chem. Mater.* **20**, 2234-2241 (2008).

31. Stepanov, A. G., Shegai, T. O., Luzgin, M. V., Essayem, N., Jobic, H., *J. Phys. Chem. B* **107**, 12438-12443 (2003).

32. Younger, P. L., Banwart, S. A., Hedin, R. S., *Mine Water: Hydrology, Pollution, Remediation (Environmental Pollution)*. (Kluwer Academic Publishers, Dordrecht, ed. 1st, 2002).

33. Isaacs, E. D., Shukla, A., Platzman, P. M., Hamann, D. R., Barbiellini, B., Tulk, C. A., *Phys. Rev. Lett.* **83**, 4445-4445 (1999).

34. Neuefeind, J., Benmore, C. J., Tomberli, B., Egelstaff, P. A., *J Phys-Condens Mat* **14**, L429-L433 (2002).

35. Feng, X. H., Liu, F., Tan, W. F., Liu, X. W., *Clays Clay Miner.* **52**, 240-250 (2004).

36. Feng, Q., Lui, L. , Yanagisawa, K. , *J. Mater. Sci. Lett.* **19**, 1567 - 1570 (2000).

Chapter 5

Investigation of Vacancies in Hexagonal Birnessite via EXAFS Modeling

A series of hexagonal birnessites, synthesized with increasing layer vacancy concentrations and characterized in Chapter 4 by SEM, laser light scattering measurements, X-ray diffraction, and ^{2}H MAS NMR, was studied via EXAFS Mn K-edge data modeling. A structural model was developed to simulate the collected EXAFS spectra of the samples in this series. Scattering paths were selected and parameterized for inclusion in a structural model developed based on the foreknowledge obtained regarding structural characteristics of the samples from the previous characterization discussed in Chapter 4. The refined occupancy of layer manganese in the sample series indicate that vacancies increase from sample No. 2 through No. 5 and No. 7, with the No. 1 sample having a refined layer vacancy concentration similar to that of sample No. 4 or No. 5. These results support the reported layer vacancy trends observed in the ^{2}H NMR study. Therefore, the structural model produced in this work illustrates the simplifications that can be made and still extract extended structural information such as layer vacancy content. Correlation of Pb uptake with that of layer vacancy content was then explored via Pb exchange of samples No. 2, 4 and 7, as well as two forms of triclinic birnessite containing little to no layer vacancies, NaBi-H-I and NaBi-II. While no notable increase of Pb was observed for No. 2, 4, and 7, the results are similar to those observed in the Zn exchange experiments described in Chapter 4 which was attributed to multiple cation species (e.g. K^{+} and H_3O^{+}) participating in charge compensation and competing with Pb for uptake. However, the uptake of Pb in the hexagonal birnessites was notably greater than that of the triclinic birnessites. Comparison of the Pb content of exchanged NaBi-H-I with that of NaBi-II suggests that disordered stacking and low crystallinity (as exhibited by NaBi-H-I) seem to favor increased Pb uptake over ordered layer stacking and high crystallinity (as exhibited by NaBi-II).

This chapter is modified from a manuscript that has been prepared for publication.

I. Introduction

A. Hexagonal Birnessite and Previous Characterization

This chapter investigates refinement of Mn k-edge EXAFS data on a series of synthetic hexagonal birnessite samples previously studied using ^{2}H solid state Magic Angle Spinning Nuclear Magnetic Resonance (MAS NMR), as reported in Chapter 4.[1] Forward simulations of X-ray diffraction data and simulations of Mn K-edge EXAFS spectroscopy measurements have been used to quantify vacancy sites within biogenic and synthetic hexagonal birnessites, convincingly linking the coordination of cation species at vacancy sites with reasonable precision.[2, 3] Unfortunately the quantification vacancies in these materials via XRD simulations and EXAFS modeling have high errors associated with the refinements of this particular structural feature. Forward simulations of X-ray diffraction powder patterns use a variety of structural models to produce different diffraction effects,[22] which are then compared to experimental XRD patterns to determine via trial-and-error the proper structural fit parameters.[4] Many types of disorder that are present in mixed valence manganese oxides (*i.e.* vacancy defects, layer stacking defects, Jahn-Teller distortions) produce similar peak shape/broadening effects or changes in peak intensities in experimental X-ray diffraction powder patterns, [5] for which Rietveld refinement and/or pattern simulations are not particularly sensitive in differentiating unambiguously.[6] Similarly, building a structural model to fit EXAFS spectra is complicated by Jahn-Teller distortions, edge terminations and layer vacancy defects that affect peak shapes and intensities.[7, 8] However, for both techniques, advanced structural knowledge of the material enables the use of constraints, allowing the extraction of extended structural information.

B. Previous EXAFS Structural Models for Birnessite

Several EXAFS studies investigate the development of a robust structural model for improving the refinement of extended structural features such as vacancies, but the complexity of these models makes them difficult to apply to a variety of differing samples.[7, 8] Ressler et al. refined the structures of sodium birnessite and other phyllomanganates using a model that included a total of 57 scattering paths (13 single scattering (SS) paths and 44 multiple scattering (MS) paths).[8] This model emphasized that any SS and MS paths contributing to the EXAFS scattering (with amplitudes $\geq$ 2%) must be included in the model fit to obtain meaningful refinements, constraining parameters based on foreknowledge of the structure to reduce the

number of floated parameters. Included SS paths were further constrained by using SS paths as componential legs defining MS paths. Peak intensities in R space were attenuated by using split shells in the structural model to account for Jahn-Teller distortions that are typically present in mixed valence phyllomanganate materials. The occupancy of layer Mn was not refined in these materials, as it was assumed vacancies are a minor contribution.

While the model employed by Ressler et al. obtained good fits to the experimental data, the model itself is cumbersome for the less expert EXAFS spectroscopist to wield and has limited applications to future studies of similar materials that are encompassed by the term of "birnessite." Upon reviewing available literature on birnessite, it becomes clear that the term "birnessite", in practice, actually refers to veritable structural continuum of mixed valence layered manganese oxides that are typically characterized by a 7Å interlayer spacing.[9, 10] Depending on the synthesis conditions, the average oxidation state (AOS) of layer manganese can vary considerably, as well as amounts of layer vacancies and the types, amounts and distribution of interlayer counter ions.[2, 11-14]

Webb et al. modified the model presented by Ressler et al., exploring the inclusion of only SS and MS paths with significant scattering contributions, demonstrating that meaningful extended structural information could still be extracted with such simplifications. This model used a total of 29 paths, reducing the number of MS paths to include only three collinear 3- and 4-leg paths determined to dominate multiple scattering contributions.[7] Shells were still included as split shells to account for peak intensity attenuation due to Jahn-Teller distortions. The parameter, f_{occ}, was introduced to refine layer Mn occupancy to account for vacancies, and a parameter, β, was included to refine the buckling of the layers from Jahn-Teller distortions, accounting for the attenuation of intensities of the collinear MS paths. A SS path was included to account for the presence of corner sharing interlayer Mn^{2+} capping layer vacancies, and all path intensities were attenuated according to the refined amount of interlayer Mn^{2+} contributing to the second Mn k-edge environment. While the inclusion of interlayer Mn^{2+} and even interlayer Ca^{2+} ions (which were likely to be present given the preparation of the materials in the study) was relevant to the structural refinement of these materials, without proper constraints on these variables, the refined values often had greater than 50% error.

C. Previous Structural Characterization of the Samples Investigated

In this work, we attempt to tailor the model used by Webb et al. to include "case specific" relevant features to yield an optimized model structure for the samples in question. The series of hexagonal birnessites used in this study were previously characterized via X-ray diffraction, SEM, laser light scattering measurements and ^{2}H MAS NMR to determine particle size distributions and relative layer vacancy contents in each sample (Chapter 4).[1] In the ^{2}H NMR study of the samples in the series, numbered No. 1 through No. 8 (No. 1 expected to have the fewest vacancies, each subsequent sample increasing in layer vacancy concentration through to No. 8, expected to have the greatest amount of vacancies), SEM images of samples indicated No. 6 and No. 8 had α-MnO_2 impurities and were excluded from further analysis. For this reason, only samples No. 1 through No. 5 and No. 7 will be considered in our investigation. Pertinent information regarding the structural characterization of these samples includes laser light scattering measurements indicating a similar particle size distribution throughout the sample series, with a particle size range typically falling between 250 – 600nm. Terminal manganese octahedra were estimated to account for only 0.24% of total manganese octahedra in a hexagonal particle shape that is 400nm in diameter. With no evidence for smaller particles in these materials, edge terminations will likely have negligible impact on the EXAFS model used in this work to refine the apparent occupancy of layer manganese.

Elemental analyses of K and Mn showed a decreasing trend of the K:Mn ratio from sample No.1 to No. 5 and No. 7, however, it was reasoned that because the pH of the reaction mixture was decreasing across the sample series, protons likely became the more abundant counter ion available. It was also determined that Mn^{2+} likely plays a minimally small role as a counter ion in these materials since Mn^{2+} was not readily available in the reaction mixture and because it has been noted that uptake of Mn^{2+} present from disproportionation of layer Mn^{3+} in synthetic birnessites becomes minimal below a pH of 4.[11] Elemental analysis of the supernatant of Zn^{2+} exchange into sample No. 2, No. 4 and No. 7 indicated only minor or undetectable release of Mn^{2+} ion solution (Pena et al. observed the release of notable amounts of Mn^{2+} ions into solution upon sorption of Ni^{2+} onto biogenic birnessite [15]),[1] also suggesting an minimal interlayer Mn^{2+}.

The integration of the low temperature ^{2}H NMR spectra allowed the determination of the number of moles of vacancies per mg of sample.[1] Quantification of vacancies using the

potassium and vacancy deuterium contents determined from elemental analysis and spin counting of NMR spectra, respectively, indicated that some amount of potassium charge compensates layer Mn^{3+}. The layer Mn^{3+} content, for all samples, was determined to be less than 22%, and thus, without sufficient Mn^{3+} present in the layers to produce a coordinated Jahn-Teller distortion, hexagonal layer symmetry was observed in the samples. Sample No. 1 was determined to be a slight outlier with regards to layer vacancies in the sample series, where integration of peak intensities from the ^2H NMR spectrum gave a vacancy content between that of the No. 4 and No. 5 samples. However, for the purposes of this study, the values obtained via integration of ^2H NMR spectra are not a reliable means of direct comparison to results of EXAFS model fits; complete deuteration of samples was not ensured, suggesting that the calculated vacancy content for each sample is actually an underestimate of the actual layer vacancy concentration. Another factor contributing to the inaccuracy of the spin counting performed on NMR spectra is the simplistic assumptions made for charge compensation per vacancy; only deuterons and potassium were assumed to charge compensate layer vacancies, ignoring cation species such as Mn^{2+} and D_3O^+ which are also likely to be present as counter ions. As a result, only the general trend of increasing layer vacancies, with sample No. 1 being a slight outlier, can be reliably taken from the ^2H NMR study for applications toward this EXAFS Mn K-edge study.

II. Experimental Methods

A. Data Collection

Samples were diluted with sucrose and loaded into an aluminum sample holder, 1mm thick, with kapton X-ray windows and into a liquid nitrogen cryostat. Transmission Mn K-edge XAS spectra were collected at the SSRL beamline 4-1, equipped with a Si(220) monochromator and harmonic rejection mirror set at a 9.5keV cut off energy. Energy calibration was performed in a separate experiment by use of the pre-edge peak of $KMnO_4$ (6543.34eV) periodically throughout data collection.

B. Data Processing

Collected spectra were analyzed by using SixPack and the IFEFFIT library.[16, 17] Data reduction included aligning replicate spectra to a common energy scale, dead-time correction and signal averaging. Averaged spectra were background-subtracted with the following parameters: E_o = 6550eV, R_{bkg} = 1.0Å with no clamps, a linear pre-edge function and quadratic post-edge

function, default number of spline knots, a Kaiser-Bessel window function, and *k*-weight = 3. Phase and amplitude functions for single scattering (SS) and multiple scattering (MS) paths were calculated using FEFF6l.[18] The atom cluster used in these calculations was generated by WebAtoms,[19] using the crystal structure of triclinic birnessite published by Post et al.[9] The Mn k-edge EXAFS were fit using a layered manganese oxide structure, modified from the procedure used by Webb et al. to model biogenic manganese oxides. [7, 12] The amplitude reduction factor (S_o^2) of 0.86 was determined by fitting the Mn-O shell of $MnCl_2$(aq) EXAFS spectrum. A single ΔE_0 was applied to all paths and allowed to vary during fitting.

C. Pb Exchange of Pristine Materials

Pristine materials No. 2, 4 and 7 were selected for Pb exchange, as well as two forms of triclinic birnessite, NaBi-H-I (disordered layer stacking, low crystallinity) and NaBi-II (ordered layer stacking, high crystallinity), as was synthesized and discussed in Chapter 2. A suspension of 250mg of pristine material in 90mL de-ionized water was brought to pH = 4 using small amounts of stock KOH and/or HCl solutions. Two millimoles of $Pb(NO_3)_2$ was then added to the suspension under vigorous stirring and the pH maintained at pH = 4 via auto-titration of the KOH stock solution. The reaction mixture was stirred for 24 hours, the solids centrifuged and the supernatant decanted. The solids were then re-suspended in de-ionized water to wash the materials, centrifuged and decanted. This was repeated 5 times for each sample. Elemental analysis was performed using flame atomic absorption spectroscopy (AAS) by the Analytical Lab, Marine Science Institute at the University of Santa Barbara to obtain the Pb:Mn ratios for each exchange sample.

III. Results

A. Raw Data

The presence of commonly used diagnostic features in the EXAFS data at 6.8 , 8.0 and 9.3$Å^{-1}$ confirms that these samples are layered materials (Figure 5.1 b.).[20] In particular, the sharpness of the feature at 8.0 $Å^{-1}$ differentiates these materials as layered instead of the tunnel structure, todorokite, as was illustrated by McKeown and Post (2001) where the origins of this feature were determined to be from the second nearest neighbor Mn-Mn contributions; in todorokite, this feature is dampened due to the presence of two different second shell Mn-Mn contributions.[20] A single antinode at the 8.0 $Å^{-1}$ feature provides confirmation of hexagonal layer

symmetry,[7, 12] as a double antinode would be present at this feature due to Jahn-Teller distortions for triclinic birnessite.

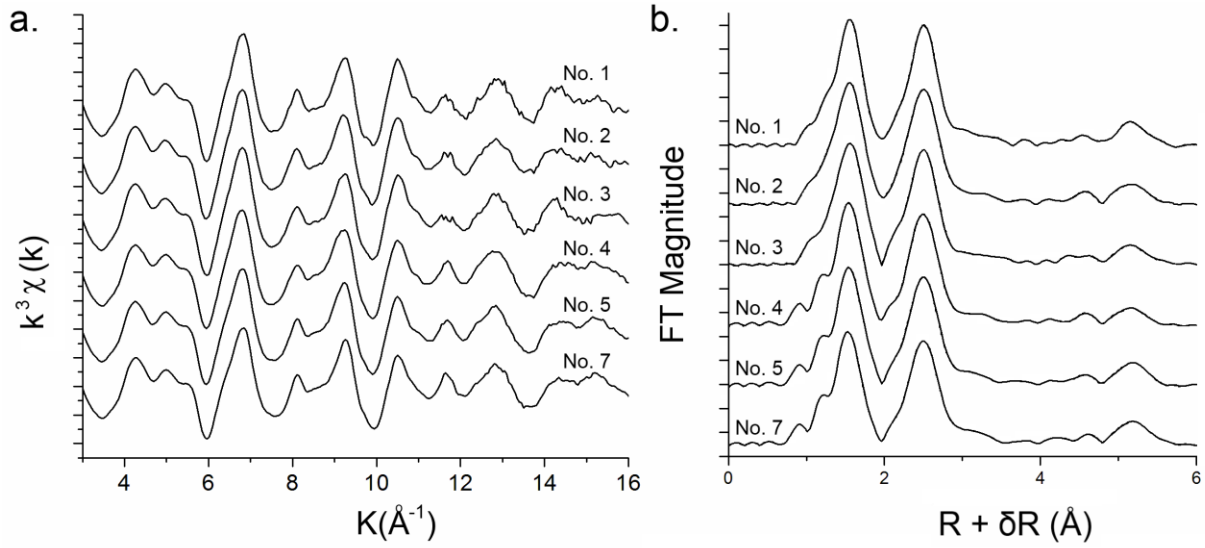

Figure 5.1 (a) EXAFS data at the Mn K-edge and (b) Fourier transforms. Fourier transforms are not corrected for phase shift.

The Fourier transforms of the Mn K-edge EXAFS (Figure 5.1 b.) data show features also supporting hexagonal layer symmetry for all the birnessite samples. The intensity peak near 5.6Å^{-1} indicates minimal layer bending that typically occurs in triclinic birnessite where Jahn-Teller distortions cause buckling of the Mn – Mn – Mn scattering pathways in the layers.[7]

B. Development of Structural Model

All EXAFS spectra were fit in *R*-space over the *k*-range 3-16.3Å^{-1} and *R*-range 1-10Å, with a total of 15 independent points (n_{indep}). A structural model modified from the model developed by Webb et al. was applied to these spectra.[7]

A total of 7 SS paths were included, accounting for first, second and third shell Mn-O; first, second and third shell Mn-Mn; and a Mn-K path to account for the presence of interlayer K^+ ions. The coordination numbers (CN) of included shells were fixed based on foreknowledge of the birnessite structure given by Post and Veblen,[9] and not directly refined in the fit. The CN for the Mn-K scattering path was set to a value of 6, which was attenuated by the K:Mn ratio determined by elemental analysis, the results of which are discussed in Chapter 4. Layer Mn vacancies were refined in terms of the layer occupancy of Mn, defined in the model as f_{occ}. As

mentioned previously, terminal manganese octahedra account for only 0.24% of all octahedra in hexagonal shaped particle layer of 400nm, which is a mid-range estimate of the particle size distribution observed in all samples.[1] Webb et al. used Monte Carlo simulations to demonstrate the effect of edge terminations on the refined occupancy of layer Mn, estimating that particle sizes larger than 30-50nm will not be significantly impacted by edge Mn octahedra.[7] Therefore, edge terminations are expected to have only a minor impact on the variable f_{occ}.

Interlayer Mn^{2+} ions, though included as an important contribution to EXAFS scattering in some models in the literature, was excluded from this model, following from the analyses in the ^2H NMR studies of these materials indicating it was likely an insignificant component of interlayer ion species.[1] Thermal disorder was expected to be minimal in the collected spectra since the data was collected using a cryostat sample holder. With no presumed ordering of layer vacancies, static disorder from distortions surrounding vacancies was assumed to be random. All Debye-Waller factors were floated for Mn-Mn SS paths, while the Debye-Waller factors for the second and third Mn-O SS paths were linked.

As with the model in Webb et al., three types of collinear MS paths were considered and parameterized similarly in this model: a 3-legged Mn-Mn-Mn path and two 4-legged Mn-Mn-Mn-Mn paths (Figure 5.2) in which the path distances and Debye-Waller factors for these MS paths are parameterized using SS path components, and therefore are not freely varied.

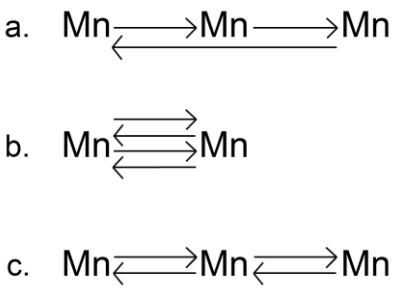

Figure 5.2 Illustration of the three and four legged MS paths between adjacent Mn atoms in the lattice that are included in the model. (a) a triple MS path between three different adjacent Mn atoms. (b) a quadruple MS path between two Mn atoms. (c) a quadruple MS path between three Mn atoms. The arrows indicate the direction of the scattered photoelectron.

The same assumption was made whereby correlated bond distances in the MS paths have a Debye-Waller equal to $\sigma^2_{MS} = 4\sigma^2_{SS}$ and MS paths in which bond distances are not fully correlated, the Debye-Waller is reasonably approximated by $\sigma^2_{MS} = 2\sigma^2_{SS}$. Unlike the model in Webb et al., layer bending (resulting from Jahn-Teller distortions commonly observed in triclinic

birnessites) was not included. The samples under investigation in this study have been characterized as hexagonal birnessite and therefore, layer bending is expected to be minimal. The exclusion of this parameter reduces the number of included paths considerably since split shells need not be considered.

Table 5.1 Summary of EXAFS parameters from the Mn K-edge using the developed structural model.

Sample	R	χ^2	f_{occ}	Shell	CN	Dist(Å)	σ^2
1	0.0114	1430	0.83(5)	Mn-O	6	1.906(2)	0.0049(2)
				Mn-Mn edge	6	2.877(2)	0.0058(4)
				Mn-O	6	3.46(1)	0.006(1)
				Mn-K interlayer	1.32	3.90(5)	0.004(5)
				Mn-O	12	4.73(2)	
				Mn-Mn diag	6	4.96(1)	0.009(1)
				Mn-Mn next	6	5.53(1)	0.007(1)
2	0.0086	1073	0.88(5)	Mn-O	6	1.908(2)	0.0049(2)
				Mn-Mn edge	6	2.881(2)	0.0062(3)
				Mn-O	6	3.455(8)	0.007(1)
				Mn-K interlayer	1.4	3.92(5)	0.003(5)
				Mn-O	12	4.72(1)	
				Mn-Mn diag	6	4.96(1)	0.009(1)
				Mn-Mn next	6	5.54(1)	0.008(1)
3	0.0134	1649	0.86(6)	Mn-O	6	1.909(2)	0.0048(2)
				Mn-Mn edge	6	2.879(3)	0.0062(4)
				Mn-O	6	3.46(1)	0.007(1)
				Mn-K interlayer	1.44	3.91(2)	0.005(3)
				Mn-O	12	4.75(2)	
				Mn-Mn diag	6	4.97(1)	0.009(1)
				Mn-Mn next	6	5.54(1)	0.008(2)
4	0.0147	1731	0.80(7)	Mn-O	6	1.907(3)	0.0050(2)
				Mn-Mn edge	6	2.879(3)	0.0059(5)
				Mn-O	6	3.45(1)	0.007(2)
				Mn-K interlayer	1.38	3.91(4)	0.009(5)
				Mn-O	12	4.73(2)	
				Mn-Mn diag	6	4.96(2)	0.009(1)
				Mn-Mn next	6	5.53(2)	0.010(3)
5	0.0162	1845	0.81(7)	Mn-O	6	1.907(3)	0.0052(2)

				Mn-Mn edge	6	2.879(3)	0.0060(5)
				Mn-O	6	3.46(1)	0.007(1)
				Mn-K interlayer	1.18	3.93(4)	0.009(5)
				Mn-O	12	4.74(2)	
				Mn-Mn diag	6	4.97(2)	0.008(2)
				Mn-Mn next	6	5.54(2)	0.007(2)
7	0.0161	1676	0.76(7)	Mn-O	6	1.904(3)	0.0056(2)
				Mn-Mn edge	6	2.873(3)	0.0057(5)
				Mn-O	6	3.45(1)	0.006(1)
				Mn-K interlayer	0.85	3.91(4)	0.011(6)
				Mn-O	12	4.75(2)	
				Mn-Mn diag	6	4.97(2)	0.008(2)
				Mn-Mn next	6	5.53(2)	0.006(1)

The refinements of the k-edge Mn EXAFS data using the structural model described are presented in Table 5.1. The R factors and χ^2 values, the measures for "goodness-of-fit" of the calculated EXAFS fit, indicate reasonable fits to the data. The vacancies, refined through the fit parameter, f_{occ}, show the expected decreasing trend across the sample series, also indicating sample No. 1 is an outlier regarding layer vacancy concentration (as was observed via ^{2}H NMR from Chapter 4).

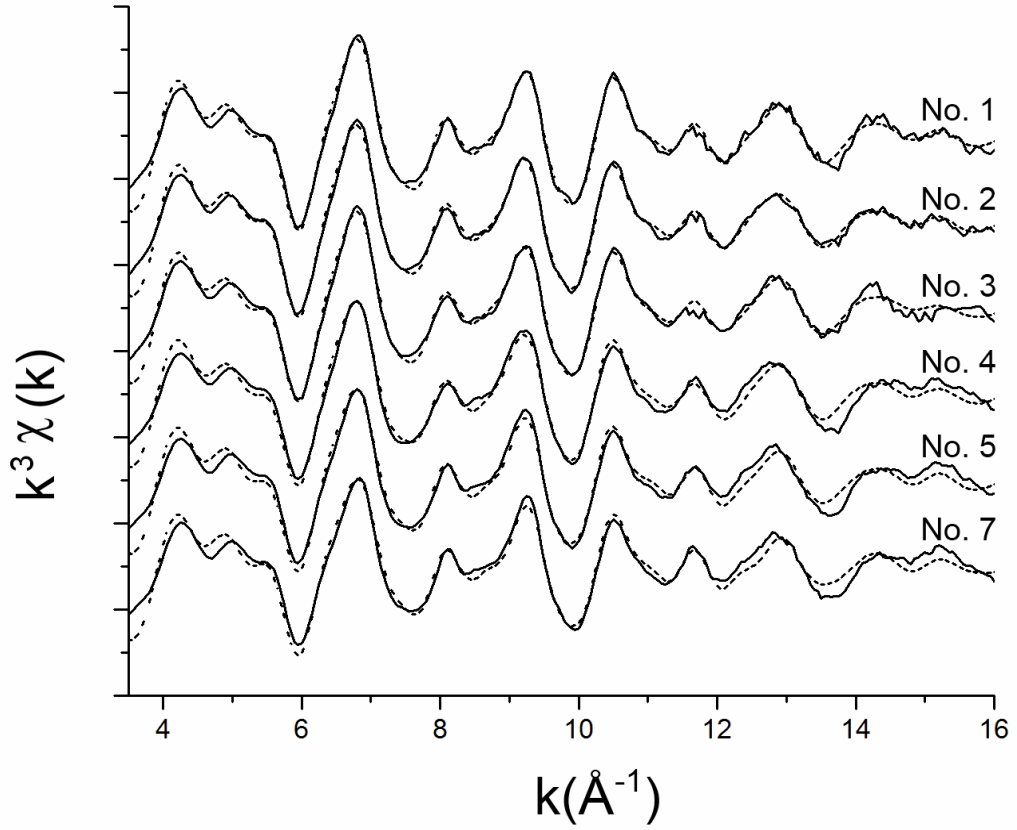

Figure 5.3 EXAFS data for hexagonal birnessite vacancy series samples. Raw data is shown as solid lines, the data fit from the structural model is denoted by dotted lines. Each spectrum and fit are labeled with the sample name, No. 1 through No. 5 and No. 7.

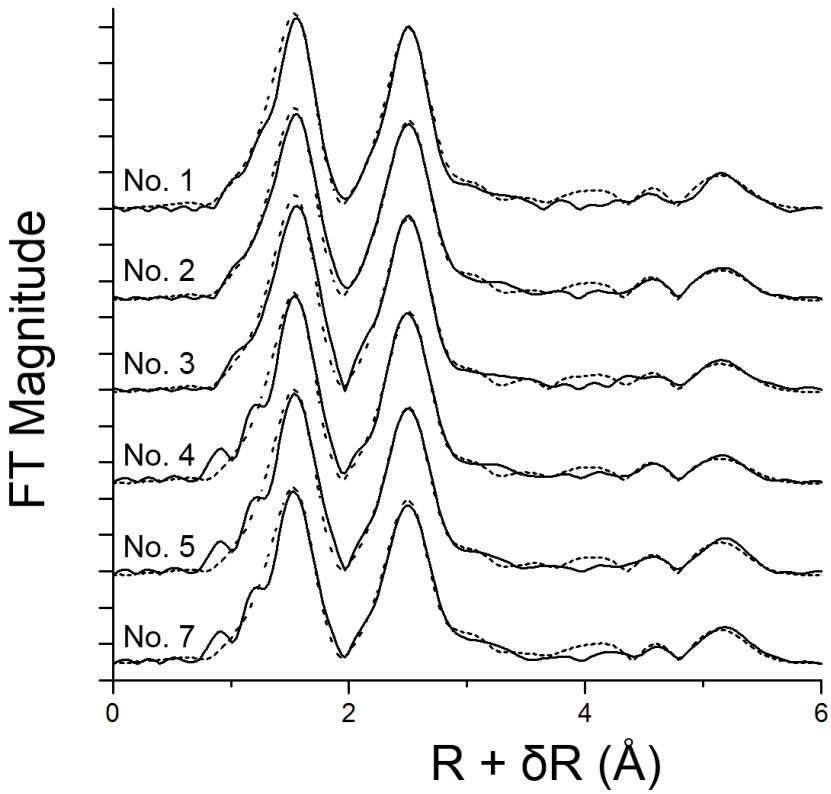

Figure 5.4 Fourier transforms of the EXAFS data and model fits. Collected spectra are shown as solid lines and structural model fits are shown as dotted lines. Each spectrum and fit are labeled with the sample name, No. 1 through No. 5 and No. 7.

Data fits, shown in k space and in R space (Figures 5.3 and 5.4, respectively), indicate the model provides a good fit to the hexagonal birnessites. The peak distances in Figure 5.4 are not phase corrected for the phase shift that occurs with the photoelectron backscattering process, and therefore are shifted to lower R values by about 0.4Å. The EXAFS data (Figure 5.3) shown show slight phase discrepancies between the data and fit for samples No. 4, No. 5 and No. 7 between 12$Å^{-1}$ to 15$Å^{-1}$, and data fits shown in the Fourier transforms (Figure 5.4) show slight intensity discrepancies between 3.5 and 4.5Å.

C. Elemental Analysis of Pb Exchanged Materials

The elemental analysis of the Pb exchanged samples shows no notable difference in Pb uptake between the vacancy series birnessite samples No. 2, 4, and 7. However, there is considerably less Pb uptake in the triclinic birnessite samples, NaBi-H-I and NaBi-II, compared to that of the vacancy series samples. While the Pb content of the triclinic birnessites is

considerably less than for the hexagonal birnessite samples, the Pb content of the NaBi-H-I sample is twice that of the NaBi-II sample.

Table 5.2 The Pb:Mn ratios derived from elemental analysis of Pb exchanged samples.

Sample	Pb:Mn ratio
No. 2	**0.28**
No. 4	**0.23**
No. 7	**0.22**
NaBi-H-I	**0.18**
NaBi-II	**0.083**

IV. Discussion

A. Regarding Important Structural Features of the Hexagonal Birnessite Materials of this Study

Split shells were initially included, but were observed to collapse to the same interatomic distances in initial refinements. This indicated, as expected, that Jahn-Teller distortions were not a significant feature of these samples, consistent with hexagonal birnessite layer symmetry. Some distortions are likely to occur in hexagonal birnessites surrounding layer manganese vacancies,[21] but since no definitive ordering scheme for layer vacancies is presented in the literature, these distortions will be treated as disordered (unlike the coordinated Jahn-Teller distortions that can be addressed with split shells) and can be accounted for with refinement of Debye-Waller factors as part of the static disorder present. Since Jahn-Teller distortions were concluded to not be a relevant feature of these materials, refinement of layer buckling was also excluded.[7] This is supported by the observation of an intense peak around 5.6Å in the Fourier transforms of the EXAFS data (Figure 5.4), a feature in birnessite Mn k-edge spectra which has been shown to be extremely sensitive to the presence of layer buckling, the intensity decreasing notably even with small amounts of buckling.[7, 12]

Attempts were made to include Mn^{2+}-O and Mn-Mn^{2+} scattering paths to account for the presence of interlayer Mn^{2+} ions, floating the CN of Mn^{2+} present, but the model could not be

adequately constrained. When the CN of the Mn-Mn^{2+} scattering path was floated, it was observed to directly correlate with the f_{occ} value; the f_{occ} value decreased as the CN of the Mn-Mn^{2+} scatter path increased. It was decided the inclusion of this the interlayer Mn^{2+} scattering paths could not be justified without more information to constrain them in the model. As a result, the only interlayer cation included in the model was a Mn-K scattering path. The necessity of including this path was evaluated by comparison of the calculated R factor values of the model containing and excluding the Mn-K scattering path. Interestingly, the R factors were improved by ~2 to 6% for samples No. 1 through No. 4, and the R factors were slightly worsened by ~1% for samples No. 5 and No. 7. Since the decrease in improved fit with the inclusion of the Mn-K scattering path across the sample series was consistent with the potassium content decreasing across the sample series, from No.1 to No. 5 and No. 7, and the negative impact on the R factors for No. 5 and No. 7 were minor, the path was retained in the structural model. Coordination numbers for this path were constrained using the K:Mn ratios determined via elemental analysis reported in the previously mentioned ^{2}H NMR study.[1]

The Debye-Waller factors, σ^2, of Mn-O and Mn-Mn SS paths were found to refine to notably larger values than typically accepted for fits (0.013 – 0.025) when all were floated freely. When a Debye-Waller factor was shared for the second and third Mn-O shells, the values of all other SS paths refined to reasonable values. Unfortunately this leads to a noticeable overestimation of the intensity due to the Mn-O shell at ~4.5Å. This discrepancy may be due to the presence of some Mn^{3+} ions in the layer, as reported in Chapter 4; while the Mn^{3+} present in these materials appears to be insufficient to produce the coordinated Jahn-Teller distortions, it may be the source of the large refined Debye-Waller factors when σ^2 is freely floated for all paths. However, it is difficult to account for this disorder in a systematic manner that can be included in a structural model since the distortions produced by the the Mn^{3+} present in the layer are unknown and can therefore, not be easily be parameterized.

The σ^2 for the Mn-K SS path refined to somewhat lower values for some of the sample spectra, but with errors within reasonable values. Due to the general disorder reported for interlayer cation ordering in birnessites,[9, 22, 23] larger σ^2 values might be expected for this SS path, but small σ^2 values may imply that inclusion of other interlayer species may be necessary. For example, Webb et al. included SS paths for interlayer Mn^{2+} and Ca^{2+} (or Na^+) counter ions

present in the materials in the study. While Mn^{2+} ions are expected to be a minority component of interlayer species in the materials of this study, interlayer water or hyrdonium ions (H_3O^+) may become a more important backscatterers as protons play a larger role in charge compensation in lieu of larger counter ions. A slight overestimation of intensity in the model fits in the Fourier transformed spectra from 3.5 to 4.5Å region may be due to the exclusion of scattering paths from more interlayer species (Figure 5.4). However, since reasonable fits were obtained without inclusion SS paths for interlayer species other than K^+, they were left out of the model for the sake of keeping the parameterization as simple as possible.

The refined values of f_{occ} for each sample follow a decreasing trend, indicating layer vacancies are increasing in the materials, from sample No. 2 through No. 5 and No. 7. The No. 1 is also shown in the EXAFS data fits to be an outlier regarding the change in layer vacancy concentration, with respect to the sample series, with an f_{occ} value similar to the No. 4 and No. 5 materials. As anticipated, the No. 1 sample is an outlier, though is not definitively placed as having greater vacancy content than the No. 5 material. However, within the reported errors for the f_{occ} values, the same trend reported in the previously mentioned NMR study is observed in the fits using the developed EXAFS model.

B. Regarding Common Important Structural Features of Other Birnessites

As suggested in the introduction, the term birnessite encompasses layered manganese oxides with a variety of structural features. As such, any refinement of Mn K-edge EXAFS data will likely require specific adjustment to parameterization of available models presented in the literature (and in this work).

Particle size of materials should be determined to assess whether or not terminal manganese octahedra will significant impact refinements of layer vacancies. Characterization via several techniques such as X-ray diffraction, laser light scattering measurements, SEM or TEM, will make this determination more accurate. If particle sizes necessitate consideration in development of a structural model, calculating the percentage of edge octahedra relative to all octahedra in a layer of the average sample particle size can be used to adjust the modulation of pertinent scattering path intensities in the model.

Both split shells to account for Jahn-Teller distortions and unsplit shells should be explored to see which describes the data best, as was explored in the beginning development of the model used in this work. The presence of Jahn-Teller distortions will also likely require addressing layer buckling. The intensity of the peak feature around 5.6Å will also allow assessment of how important layer buckling is, and whether or not it need be included.

Elemental analysis provides useful information regarding composition of interlayer species for determination of which Mn_{layer}-$X_{interlayer}$ (where X is a charge compensating cation) SS paths to include. Though it was not performed in this study, the average oxidation state of manganese could provide useful information as to the amount of Mn(III) and/or Mn(II) present. Confirmation of whether or not Mn^{2+} ions compose a significant portion of interlayer species can be obtained via detection of Mn in the supernatant in ion exchange reactions (as was performed in the ^{2}H NMR study using Zn^{2+} ion exchange).

C. Correlating Ion Uptake with Layer Vacancies

Samples No. 2, 4, and No. 7 were used for Pb exchange experiments in order to correlate the amount of ion uptake with layer vacancy content. Two forms of triclinic birnessite were also included in the exchange experiments for comparison. Previously described in Chapter 3, sample NaBi-H-I is a turbostratically stacked triclinic birnessite, and NaBi-II is a more crystalline and well ordered triclinic birnessite.[24]

Surprisingly, the Pb:Mn ratio of the elemental analyses of the exchanged No. 2, 4 and 7 materials show little difference in the Pb uptake with the increasing layer vacancies present from No.2 to No. 4 and No. 7, as determined from the EXAFS model fits, as well as from the ^{2}H NMR quantification discussed in Chapter 4. However, these results are similar to those observed with Zn exchange experiments performed in Chapter 4; the trends with Zn exchange were attributed to an increasing amount of D_3O^+ ions present as counter ions as well, in competition with other interlayer cations. Since the exchange of Pb into these materials was performed at pH = 4, there is an increased likelihood of H_3O^+ being present as a competing counter ion in the Pb exchanged materials as well. Therefore, the apparent lack of enhanced uptake of Pb by increasing layer vacancies in these materials is again attributed to a more complex charge compensation scheme involving multiple species of counter ions. It is also important to note that under different

conditions, more resembling likely environmental conditions, a correlation between increased uptake of Pb and increased layer vacancies may be observed.

However, despite the trends observed in the comparative Pb uptake of the selected vacancy series samples, the elemental analyses of the exchanged triclinic birnessite samples NaBi-H-I and NaBi-II indicate notably less Pb uptake compared to that of samples No. 2, 4, and 7. These results are consistent with the expectation that layer vacancies, producing a greater negative layer charge than layer Mn^{3+} ions (the dominant source of negative layer charge in triclinic birnessite), allow for increased ion uptake into birnessite. Interestingly, the Pb content of the more disordered NaBi-H-I birnessite is more than double that of the more ordered NaBi-II, suggesting that the disordered layer stacking contributes to increased uptake and sorption of ions into the interlayers of these materials.

V. Conclusions

A structural model was developed using simplifications of previous models based on foreknowledge of the series of hexagonal birnessite samples under investigation. Through previous characterization, a trend of increasing layer vacancy content was expected. The EXAFS refinements using the structural model support this trend, producing the same results observed with ^{2}H NMR regarding sample No. 1 as outlier. These results illustrate how important structural features can be special tailored in the development of a model that best describes the nature materials being studied. This study focused on simplifying parameterization as much as possible, and demonstrated how reliable extended structural information such as layer vacancy content could still be extracted. The ion exchange of Pb into selected samples from this vacancy series indicates that the vacancy content has no real impact on the amount of Pb taken up into the interlayers under the conditions in which the exchanges were performed. Under the conditions of the Pb exchange performed in this study, it is also likely that a more complex charge compensation scheme exists and therefore, the dynamics of competition between different cation species must be addressed. However, there was notably less Pb uptake in the two triclinic birnessite samples included in this exchange study, suggesting that vacancies do produce an increase in Pb uptake relative to the absence of layer Mn vacancies. With more than double the Pb content in the NaBi-H-I exchanged sample compared to that of the NaBi-II exchanged sample suggests that the disordered layer stacking aids in increased Pb uptake as well.

VI. References

1. Aldi, K. A., Heeinmaa, I., Kim, J., Ilott, A., Zheng, D., Grey, C. P., (Submitted for Publication).

2. Villalobos, M., Toner, B., Bargar, J., Sposito, G., *Geochim. Cosmochim. Acta* **67**, 2649-2662 (2003).

3. Villalobos, M., Lanson, B., Manceau, A., Toner, B., Sposito, G., *Am. Mineral.* **91**, 489-502 (2006).

4. Drits, V. A., Lanson, B., Gorshkov, A. I., Manceau, A., *Am. Mineral.* **83**, 97-118 (1998).

5. Pecharsky, V. K., Zavalij, P. Y., *Fundamentals of Powder Diffraction and Structural Characterizatin of Materials*. (Springer, New York, 2005), pp. 713.

6. Drits, V. A., Lanson, B., Gaillot, A. C., *Am. Mineral.* **92**, 771-788 (2007).

7. Webb, S. M., Tebo, B. M., Bargar, J. R., *Am. Mineral.* **90**, 1342-1357 (2005).

8. Ressler, T., Brock, S. L., Wong, J., Suib, S. L., *J. Phys. Chem. B* **103**, 6407-6420 (1999).

9. Post, J. E., Veblen, D. R., *Am. Mineral.* **75**, 477-489 (1990).

10. Kuma, K., Usui, A., Paplawsky, W., Gedulin, B., Arrhenius, G., *Mineral Mag* **58**, 425-447 (1994).

11. Lanson, B., Drits, V. A., Silvester, E., Manceau, A., *Am. Mineral.* **85**, 826-838 (2000).

12. Webb, S. M., Tebo, B. M., Bargar, J. R., *Geomicrobiol. J.* **22**, 181-193 (2005).

13. Bruno Lanson, V. A. D., Qi Feng, Alain Manceau, *Am. Mineral.* **87**, 1662-1671 (2002).

14. Silvester, E., Manceau, A., Drits, V. A., *Am. Mineral.* **82**, 962-978 (1997).

15. Pena, J., Kwon, K. D., Refson, K., Bargar, J. R., Sposito, G., *Geochim. Cosmochim. Acta* **74**, 3076-3089 (2010).

16. Webb, S. M., *Phys. Scr.* **T115**, 1011-1014 (2005).

17. Newville, M., *J. Synchrot. Radiat.* **8**, 322-324 (2001).

18. Newville, M., *J. Synchrot. Radiat.* **8**, 96-100 (2001).

19. Ravel, B., *J. Synchrot. Radiat.* **8**, 314-316 (2001).

20. McKeown, D. A., Post, J. E., *Am. Mineral.* **86**, 701-713 (2001).

21. Kwon, K. D., Refson, K., Sposito, G., *Phys. Rev. Lett.* **100**, (2008).

22. Lopano, C. L., Heaney, P. J., Post, J. E., Hanson, J., Komarneni, S., *Geochim. Cosmochim. Acta* **68**, A86-A86 (2004).

23. Manceau, A., Lanson, B., Drits, V. A., *Geochim. Cosmochim. Acta* **66**, 2639-2663 (2002).

24. Aldi, K. A., Cabana, J., Sideris, P. J., Middlemiss, D. S., Grey, C. P., (Submitted for publication).

Chapter 6

I. General Conclusions

The work described in this thesis investigates a variety of manganese oxides, both synthetic and naturally occurring, illustrating the utility of solid state NMR in the study of manganese oxides, where structural variability often complicates the characterization and comparison of compounds exhibiting such structural variety.

The comparison of ^{23}Na NMR spectra of layered sodium manganese oxide materials with differing Mn^{3+}:Mn^{4+} ratios exhibit larger observed Fermi-contact shifts with greater Mn^{4+} content. Determining the sensitivity of the Fermi-contact interaction to the oxidation state of the surrounding manganese provides useful reference for ^{23}Na NMR investigations of a various sodium manganese oxide materials, for which there is a growing interest as battery cathode materials in which manganese oxidation states change during a charge and discharge cycle.[1, 2]

The ^{23}Na NMR spectra of several synthetic sodium forms of the naturally occurring layered manganese oxide, triclinic birnessite, were also interpreted using the model compounds as references. These NMR spectra indicate significant ordering of sodium cations relative to the distribution of the Mn^{3+} and Mn^{4+} ions in the oxide layers. This suggests that cation uptake and ordering within these materials is driven by the distribution of negative charge present in the manganese oxide layer. While there are a number of studies in the literature that apply solid state NMR to the investigation of cation sorption to aluminum and iron oxide mineral surfaces,[3-5] the results reported in this thesis illustrate the utility of the technique in manganese oxide systems.

The application of ^{2}H NMR to the study of a series of hexagonal birnessites illustrated how, by means of the NMR technique of "spin counting", the layer vacancies present in the materials might be quantified. There is great interest in quantifying vacancies, as numerous studies using Rietveld refinement of XRD and structural modeling of EXAFS will attest.[6-9] The sorption capacity of these materials has been linked to the presence of layer vacancies and layer Mn^{3+} ions, and therefore a dominant influence on the uptake of various cations, particularly those of environmental interest. The trends observed in the ^{2}H NMR spectra of these hexagonal birnessites also enabled the development of a simplified but robust structural model for the refinement of Mn K-edge measurements of the hexagonal birnessite samples. The model

produced for the refinement of the Mn K-edge data illustrates that a structural model, considerably simplified from previous models, is still capable of capturing useful information regarding layer vacancies.

The comparison of the refined vacancy content via spin counting of ^{2}H NMR with that of the vacancy content extracted from Mn K-edge structural modeling fits highlights the considerably different values. The vacancy content calculated from ^{2}H NMR and considering the two different charge compensation schemes indicate layer vacancies range from 1.0-1.5% to 9.2-13.2% across the sample series. These values are considerably less than the vacancy content range of 12-24% obtained from EXAFS data fits. A number of factors may contribute to this discrepancy, including incomplete deuteration of the samples for ^{2}H NMR and more complicated charge compensation schemes involving other counter ions not taken into consideration, both of which would lead to lower vacancy concentrations obtained from spin counting NMR experiments. The vacancy content refined from EXAFS data fits may also be slightly greater than the true values due to errors introduced by edges, though this may only be a small contribution. The discrepancy between the, vacancy content obtained via ^{2}H NMR and via EXAFS refinement is considerably larger for the lower vacancy concentration samples; this can be explained by the greater layer Mn^{3+} content in these samples may produce some Jahn-Teller based distortion that would lead to diminished peak intensities for the Mn-Mn scattering paths, skewing the vacancy content values.

The exchange of Pb and Zn into selected hexagonal vacancy series birnessites and two forms of triclinic birnessite suggest that, while the presence of layer vacancies notably increases the uptake of these ions into the interlayers, the amount of uptake is not a direct function of layer vacancy content. It is postulated that the charge compensating species in the exchange of these birnessite materials are more diverse than was taken into account in this study, and that correlation of ion uptake with layer vacancy content would benefit from exchange conditions more closely resembling possible environmental conditions.

II. References

1. Carlier, D., Cheng, J. H., Berthelot, R., Guignard, M., Yoncheva, M., Stoyanova, R., Hwang, B. J., Delmas, C., *Dalton T* **40**, 9306-9312 (2011).

2. Athouel, L., Moser, F., Dugas, R., Crosnier, O., Belanger, D., Brousse, T., *J. Phys. Chem. C* **112**, 7270-7277 (2008).

3. Kim, J., Middlemiss, D. S., Chernova, N. A., Zhu, B. Y. X., Masquelier, C., Grey, C. P., *J. Am. Chem. Soc.* **132**, 16825-16840 (2010).

4. Kim, J., Nielsen, U. G., Grey, C. P., *J. Am. Chem. Soc.* **130**, 1285-1295 (2008).

5. Li, W., Feng, J., Kwon, K. D., Kubicki, J. D., Phillips, B. L., *Langmuir* **26**, 4753-4761 (2010).

6. Webb, S. M., Tebo, B. M., Bargar, J. R., *Am. Mineral.* **90**, 1342-1357 (2005).

7. Ressler, T., Brock, S. L., Wong, J., Suib, S. L., *J. Phys. Chem. B* **103**, 6407-6420 (1999).

8. Drits, V. A., Lanson, B., Gaillot, A. C., *Am. Mineral.* **92**, 771-788 (2007).

9. Lanson, B., Drits, V. A., Silvester, E., Manceau, A., *Am. Mineral.* **85**, 826-838 (2000).

References

Chapter 1

1. Post, J. E., *P Natl Acad Sci USA* **96**, 3447-3454 (1999).

2. Vodyanitskii, Y. N., *Eurasian Soil Sci+* **42**, 1170-1178 (2009).

3. Grangeon, S., Lanson, B., Miyata, N., Tani, Y., Manceau, A., *Am. Mineral.* **95**, 1608-1616 (2010).

4. Leeper, G. W., Uren, N.C. , *Soil Science, An Introduction*. (Overseas Press India Private Limited, New Delhi, ed. Fifth, 2006), pp. 300.

5. Tebo, B. M., *Deep-Sea Research Part a-Oceanographic Research Papers* **38**, S883-S905 (1991).

6. Bargar, J. R., Tebo, B. M., Villinski, J. E., *Geochim. Cosmochim. Acta* **64**, 2775-2778 (2000).

7. Bricker, O., *Am. Mineral.* **50**, 1296-& (1965).

8. Mckenzie, R. M., *Geochim. Cosmochim. Acta* **43**, 1855-1857 (1979).

9. O'Reilly, S. E., Hochella, M. F., *Geochim. Cosmochim. Acta* **67**, 4471-4487 (2003).

10. Lanson, B., Drits, V. A., Gaillot, A. C., Silvester, E., Plancon, A., Manceau, A., *Am. Mineral.* **87**, 1631-1645 (2002).

11. Toner, B., Manceau, A., Webb, S. M., Sposito, G., *Geochim. Cosmochim. Acta* **70**, 27-43 (2006).

12. Sherman, D. M., Peacock, C. L., *Geochem. Cosmochim. Ac.* **74**, 6721-6730 (2010).

13. Pena, J., Kwon, K. D., Refson, K., Bargar, J. R., Sposito, G., *Geochim. Cosmochim. Acta* **74**, 3076-3089 (2010).

14. Bargar, J. R., Fuller, C. C. , Marcus, M. A., Brearley, A. J., De la Rosa, M. P., Webb, S. M., Caldwell, W. A. , *Geochim. Cosmochim. Acta* **73**, 889-910 (2009).

15. Kuma, K., Usui, A., Paplawsky, W., Gedulin, B., Arrhenius, G., *Mineral Mag* **58**, 425-447 (1994).

16. Tevar, A. D., Whitacre, J. F., *J. Electrochem. Soc.* **157**, A870-A875 (2010).

17. Whitacre, J. F., Tevar, A., Sharma, S., *Electrochem. Commun.* **12**, 463-466 (2010).

18. Caballero, A., Hernan, L., Morales, J., Sanchez, L., Santos Pena, J., Aranda, M. A. G., *J. Mater. Chem.* **12**, 1142-1147 (2002).

19. Tsuda, M., Arai, H. Sakurai, Y., *J. Power Sources* **110**, 52-56 (2002).

20. Bach, S., Pereira-Ramos, J. P., Cachet, C., Bode, M., Tse Yu, L. , *Electrochim. Acta* **40**, 785-789 (1995).

21. Bach, S., Pereira-Ramos, J. P., Baffier, N., *J. Electrochem. Soc.* **143**, 3429-3434 (1996).

22. Post, J. E., Heaney, P. J. , Hanson, J., *Powder Diffr.* **17**, 218-221 (2002).

23. Giovanoli, R., Stahli, E., Feitknecht, W., *Helv. Chim. Acta* **53**, 209-220 (1970a).

24. Lanson, B., Drits, V. A., Silvester, E., Manceau, A., *Am. Mineral.* **85**, 826-838 (2000).

25. Lanson, B., Drits, V. A., Feng, Q., Manceau, A., *Am. Mineral.* **87**, 1662-1671 (2002).

26. Rogers, D. B., Germann, R. W., Arnott, R. J., *J. Appl. Phys.* **36**, 2338-2343 (1965).

27. Potter, R. M., Rossman, G. R., *Am. Mineral.* **64**, 1199-1218 (1979).

28. Giovanol.R, *Chimia* **23**, 470-& (1969).

29. Post, J. E., Veblen, D. R., *Am. Mineral.* **75**, 477-489 (1990).

30. Cui, H. J., Qiu, G. H., Feng, X. H., Tan, W. F., Liu, F., *Clays Clay Miner.* **57**, 715-724 (2009).

31. Feng, X. H., Liu, F., Tan, W. F., Liu, X. W., *Clays Clay Miner.* **52**, 240-250 (2004).

32. Post, J. E., Heaney, P. J., Hanson, J., *Powder Diffr.* **17**, 218-221 (2002).

33. Webb, S. M., Tebo, B. M., Bargar, J. R., *Geomicrobiol. J.* **22**, 181-193 (2005).

34. Drits, V. A., Silvester, E., Gorshkov, A. I., Manceau, A., *Am. Mineral.* **82**, 946-961 (1997).

35. Drits, V. A., Lanson, B., Gorshkov, A. I., Manceau, A., *Am. Mineral.* **83**, 97-118 (1998).

36. Lopano, C. L., Heaney, P. J., Post, J. E., Hanson, J., Komarneni, S., *Geochim. Cosmochim. Acta* **68**, A86-A86 (2004).

37. Lopano, C. L., Heaney, P. J., Post, J. E., Hanson, J., Komarneni, S., *Am. Mineral.* **92**, 380-387 (2007).

38. Giovanoli, R., Burki, P., Giuffredi, M., Stumm, W., *Chimia* **29**, 517-520 (1975).

39. Johnson, E. A., Post, J. E., *Am. Mineral.* **91**, 609-618 (2006).

40. Silvester, E., Manceau, A., Drits, V. A., *Am. Mineral.* **82**, 962-978 (1997).

41. Villalobos, M., Toner, B., Bargar, J., Sposito, G., *Geochim. Cosmochim. Acta* **67**, 2649-2662 (2003).

42. Villalobos, M., Lanson, B., Manceau, A., Toner, B., Sposito, G., *Am. Mineral.* **91**, 489-502 (2006).

43. Post, J. E., Bish, D. L., *Am. Mineral.* **73**, 861-869 (1988).

44. Post, J. E., Heaney, P. J., Hanson, J., *Am. Mineral.* **88**, 142-150 (2003).

45. Post, J. E., Vondreele, R. B., Buseck, P. R., *Acta Crystallogr. Sect. B-Struct. Commun.* **38**, 1056-1065 (1982).

46. Laws, D. D., Bitter, H. M. L., Jerschow, A., *Angew Chem Int Edit* **41**, 3096-3129 (2002).

47. Duer, M. J., Ed., *Solid-State NMR Spectroscopy: Principles and Applications*, (Wiley-Blackwell, Oxford, ed. 1st, 2001), 1st, pp. 592.

48. Ashbrook, S. E., *PCCP* **11**, 6892-6905 (2009).

49. Ilott, A. J., Palucha, S., Batsanov, A. S., Wilson, M. R., Hodgkinson, P., *J. Am. Chem. Soc.* **132**, 5179-5185 (2010).

50. Nielsen, U. G., Heinmaa, I., Samoson, A., Majzlan, J., Grey, C. P., *Chem. Mater.* **23**, 3176-3187 (2011).

51. Griffin, J. M., Miller, A. J., Berry, A. J., Wimperis, S., Ashbrook, S. E., *PCCP* **12**, 2989-2998 (2010).

52. Grey, C. P., Dupre, N., *Chem. Rev.* **104**, 4493-4512 (2004).

53. Duer, M. J., *Introduction to Soild-State NMR Spectroscopy*. (Blackwell Publishing Ltd, ed. First, 2004), pp. 349.

54. Mackenzie, K. J. D., Smith, M. E., *Multinuclear Solid-State NMR of Inorganic Materials*. R. W. Cahn, Ed., Pergamon Materials Series (Elsevier Science Ltd., ed. 1st, 2002), vol. 6, pp. 727.

55. Fukushima, E., Roeder, S. B. W. , *Experimental Pulse NMR: A Nuts and Bolts Approach*. (Addison-Wesley Publishing Company, Inc, Reading, ed. First, 1981), pp. 539.

56. Bunker, G., *Introduction to XAFS: A Practical Guide to X-ray Absorption Find Structure Spectroscopy*. (Cambridge University Press, Cambridge, 2010), pp. 268.

57. Ulery, A. L., Drees, L. R., Eds., *Methods of Soil Analysis. Part 5. Mineralogical Methods*, vol. 5 (American Society of Agronomy, Madison, 2008), vol. 5, pp. 544.

58. Bloss, F. D., *Crystallography and Crystal Chemistry: An Introduction*. (The Mineralogical Society of America, Washington, D. C., ed. 2nd, 1994).

Chapter 2

1. O'Reilly, S. E., Hochella, M. F., *Geochim. Cosmochim. Acta* **67**, 4471-4487 (2003).

2. Kuma, K., Usui, A., Paplawsky, W., Gedulin, B., Arrhenius, G., *Mineral Mag* **58**, 425-447 (1994).

3. Mckenzie, R. M., *Geochim. Cosmochim. Acta* **43**, 1855-1857 (1979).

4. Mckenzie, R. M., *Aust. J. Soil Res.* **18**, 61-73 (1980).

5. Post, J. E., Veblen, D. R., *Am. Mineral.* **75**, 477-489 (1990).

6. Drits, V. A., Silvester, E., Gorshkov, A. I., Manceau, A., *Am. Mineral.* **82**, 946-961 (1997).

7. Silvester, E., Manceau, A., Drits, V. A., *Am. Mineral.* **82**, 962-978 (1997).

8. Lanson, B., Drits, V. A., Gaillot, A. C., Silvester, E., Plancon, A., Manceau, A., *Am. Mineral.* **87**, 1631-1645 (2002).

9. Toner, B., Manceau, A., Webb, S. M., Sposito, G., *Geochim. Cosmochim. Acta* **70**, 27-43 (2006).

10. Post, J. E., *P Natl Acad Sci USA* **96**, 3447-3454 (1999).

11. McKeown, D. A., Post, J. E., *Am. Mineral.* **86**, 701-713 (2001).

12. Glasby, G. P., Ed., *Marine Manganese Deposits*, vol. 15 (Elsevier Scientific Publishing Company, Amsterdam, ed. 1, 1977), vol. 15, 1, pp. 523.

13. Yi, T. F., Zhu, Y. R., Zhu, X. D., Shu, J., Yue, C. B., Zhou, A. N., *Ionics* **15**, 779-784 (2009).

14. Whitacre, J. F., Tevar, A., Sharma, S., *Electrochem. Commun.* **12**, 463-466 (2010).

15. Qu, Q. T., Shi, Y., Tian, S., Chen, Y.H., Wu, Y.P., Holze, R. , *J. Power Sources* **194**, 1222-1225 (2009).

16. Grey, C. P., Lee, Y. J., *Solid State Sci* **5**, 883-894 (2003).

17. Grey, C. P., Dupre, N., *Chem. Rev.* **104**, 4493-4512 (2004).

18. Tevar, A. D., Whitacre, J. F., *J. Electrochem. Soc.* **157**, A870-A875 (2010).

19. Caballero, A., Hernan, L., Morales, J., Sanchez, L., Santos Pena, J., Aranda, M. A. G., *J. Mater. Chem.* **12**, 1142-1147 (2002).

20. Tsuda, M., Arai, H. Sakurai, Y., *J. Power Sources* **110**, 52-56 (2002).

21. Bach, S., Pereira-Ramos, J. P., Cachet, C., Bode, M., Tse Yu, L. , *Electrochim. Acta* **40**, 785-789 (1995).

22. Bach, S., Pereira-Ramos, J. P., Baffier, N., *J. Electrochem. Soc.* **143**, 3429-3434 (1996).

23. Mendiboure, A., Delmas, C., Hagenmuller, P. , *J. Solid State Chem.* **57**, 323-331 (1985).

24. Cheetham, A. K., Dobson, C. M., Grey, C. P., Jakeman, R. J. B., *Nature* **328**, 706-707 (1987).

25. Carlier, D., Menetrier, M., Grey, C. P., Delmas, C., Ceder, G., *Phys. Rev. B* **67**, - (2003).

26. Carlier, D., Blangero, M., Menetrier, M., Pollet, M., Doumerc, J.P., Delmas, C., *Inorg. Chem.* **48**, 7018-7052 (2009).

27. Hoppe, V. R., Brachtel, G., Jansen, M., *Z. Anorg. Allg. Chem.* **417**, 1 (1975).

28. Parant, J. P., Olazcuaga, R., Devalette, M., Fouassier, C., Hagenmuller, P., *J. Solid State Chem.* **3**, 1-11 (1971).

29. Lu, Z., Donaberger, R. A. , Dahn, J. R. , *Chem. Mater.* **12**, 3583-3590 (2000).

30. Paulsen, J. M., Dahn, J. R., *Solid State Ionics* **126**, 3-24 (1999).

31. Dolle, M., Patoux, S., Doeff, M. M., *Chem. Mater.* **17**, 1044-1054 (2005).

32. Bach, S., Henry, M., Baffier, N., Livage, J., *J. Solid State Chem.* **88**, 325-333 (1990).

33. Kim, J., Middlemiss, D. S., Chernova, N. A., Zhu, B. Y. X., Masquelier, C., Grey, C. P., *J. Am. Chem. Soc.* **132**, 16825-16840 (2010).

34. Weil, J. A., Bolton, J. R., Wertz, J. E., *Electron Paramagnetic Resonance: Elementary Theory and Practical Applications*. (John Wiley & Sons Inc., New York, ed. 1st, 1994), pp. 592.

35. Dovesi, R., Roetti, C., Freyriafava, C., Prencipe, M., Saunders, V. R., *Chem. Phys.* **156**, 11-19 (1991).

36. Lee, Y. J., Grey, C. P., *Chem. Mater.* **12**, 3871-3878 (2000).

37. Aldi, K. A., Middlemiss, D. S., Cabana, J., Sideris, P. J., Grey, C. P., (Submitted for Publication).

38. Tournadre, F., Croguennec, L., Saadoune, I., Weill, F., Shao-Horn, Y., Willmann, P., Delmas, C., *Chem. Mater.* **16**, 1411-1417 (2004).

39. Stoyanova, R., Carlier, D., Sendova-Vassileva, M., Yoncheva, M, Zhecheva, E., Nihtianova, D., Delmas, C., *J. Solid State Chem.* **183**, 1372-1279 (2010).

Chapter 3

1. O'Reilly, S. E., Hochella, M. F., *Geochim. Cosmochim. Acta* **67**, 4471-4487 (2003).

2. Pena, J., Kwon, K. D., Refson, K., Bargar, J. R., Sposito, G., *Geochim. Cosmochim. Acta* **74**, 3076-3089 (2010).

3. Mckenzie, R. M., *Aust. J. Soil Res.* **18**, 61-73 (1980).

4. Mckenzie, R. M., *Aust. J. Soil Res.* **5**, 235-& (1967).

5. Lanson, B., Drits, V. A., Gaillot, A. C., Silvester, E., Plancon, A., Manceau, A., *Am. Mineral.* **87**, 1631-1645 (2002).

6. Sherman, D. M., Peacock, C. L., *Geochem. Cosmochim. Ac.* **74**, 6721-6730 (2010).

7. Fuller, C. C., Harvey, J. W., *Environ Sci Technol* **34**, 1150-1155 (2000).

8. Harvey, J. W., Fuller, C. C., *Water Resour. Res.* **34**, 623-636 (1998).

9. Bargar, J. R., Fuller, C. C. , Marcus, M. A., Brearley, A. J., De la Rosa, M. P., Webb, S. M., Caldwell, W. A. , *Geochim. Cosmochim. Acta* **73**, 889-910 (2009).

10. Toner, B., Manceau, A., Webb, S. M., Sposito, G., *Geochim. Cosmochim. Acta* **70**, 27-43 (2006).

11. Post, J. E., *P Natl Acad Sci USA* **96**, 3447-3454 (1999).

12. Villalobos, M., Lanson, B., Manceau, A., Toner, B., Sposito, G., *Am. Mineral.* **91**, 489-502 (2006).

13. Villalobos, M., Toner, B., Bargar, J., Sposito, G., *Geochim. Cosmochim. Acta* **67**, 2649-2662 (2003).

14. Glasby, G. P., Ed., *Marine Manganese Deposits*, vol. 15 (Elsevier Scientific Publishing Company, Amsterdam, ed. 1, 1977), vol. 15, 1, pp. 523.

15. Post, J. E., Heaney, P. J., Hanson, J., *Powder Diffr.* **17**, 218-221 (2002).

16. Lanson, B., Drits, V. A., Feng, Q., Manceau, A., *Am. Mineral.* **87**, 1662-1671 (2002).

17. Kuma, K., Usui, A., Paplawsky, W., Gedulin, B., Arrhenius, G., *Mineral Mag* **58**, 425-447 (1994).

18. Feng, Q., Lui, L., Yanagisawa, K., *J. Mater. Sci. Lett.* **19**, 1567-1570 (2000).

19. Lanson, B., Drits, V. A., Silvester, E., Manceau, A., *Am. Mineral.* **85**, 826-838 (2000).

20. Drits, V. A., Silvester, E., Gorshkov, A. I., Manceau, A., *Am. Mineral.* **82**, 946-961 (1997).

21. Post, J. E., Veblen, D. R., *Am. Mineral.* **75**, 477-489 (1990).

22. Silvester, E., Manceau, A., Drits, V. A., *Am. Mineral.* **82**, 962-978 (1997).

23. Webb, S. M., Tebo, B. M., Bargar, J. R., *Am. Mineral.* **90**, 1342-1357 (2005).

24. Manceau, A., Lanson, B., Drits, V. A., *Geochim. Cosmochim. Acta* **66**, 2639-2663 (2002).

25. Gaillot, A. C., Drits, V. A., Manceau, A., Lanson, B., *Microporous Mesoporous Mater.* **98**, 267-282 (2007).

26. Rogers, D. B., Germann, R. W., Arnott, R. J., *J. Appl. Phys.* **36**, 2338-2343 (1965).

27. Lopano, C. L., Heaney, P. J., Post, J. E., Hanson, J., Komarneni, S., *Am. Mineral.* **92**, 380-387 (2007).

28. Vodyanitskii, Y. N., *Eurasian Soil Sci+* **42**, 1170-1178 (2009).

29. Duncan, M. J., Leroux, F., Corbett, J. M., Nazar, L. F., *J. Electrochem. Soc.* **145**, 3746-3757 (1998).

30. Kumagai, N., Komaba, S., Abe, K., Yashiro, H., *J. Power Sources* **146**, 310-314 (2005).

31. Song, C. H., Li, R. Q., Liu, F., Feng, X. H., Tan, W. F., Qiu, G. H., *Electrochim. Acta* **55**, 9157-9165 (2010).

32. Post, J. E., Heaney, P. J., Hanson, J., *Am. Mineral.* **88**, 142-150 (2003).

33. Post, J. E., Bish, D. L., *Am. Mineral.* **73**, 861-869 (1988).

34. Liao, S. J., Zhu, D. W., Li, Y., Liu, G. L., Liu, L. H., *React. Kinet. Mech. Catal.* **102**, 303-311 (2011).

35. Atribak, I., Bueno-Lopez, A., Garcia-Garcia, A., Navarro, P., Frias, D., Montes, M., *Appl. Catal. B-Environ.* **93**, 267-273 (2010).

36. Hu, R. R., Yan, C. F., Xie, L. Y., Cheng, Y., Wang, D. Z., *Int. J. Hydrogen Energy* **36**, 64-71 (2011).

37. Koivula, R., Pakarinen, J., Sivenius, M., Sirola, K., Harjula, R., Paatero, E., *Sep. Purif. Technol.* **70**, 53-57 (2009).

38. Post, J. E., Vondreele, R. B., Buseck, P. R., *Acta Crystallogr. Sect. B-Struct. Commun.* **38**, 1056-1065 (1982).

39. Carlier, D., Blangero, M., Menetrier, M., Pollet, M., Doumerc, J.P., Delmas, C., *Inorg. Chem.* **48**, 7018-7052 (2009).

40. Aldi, K. A., Middlemiss, D. S., Cabana, J., Sideris, P. J., Grey, C. P., (Submitted for Publication).

41. Feng, Q., Sun, E. H., Yanagisawa, K., Yamasaki, N., *J. Ceram. Soc. Jpn.* **105**, 564-568 (1997).

42. Giovanoli, R., Stahli, E., Feitknecht, W., *Helv. Chim. Acta* **53**, 209 - 220 (1970).

43. Cui, H. J., Qiu, G. H., Feng, X. H., Tan, W. F., Liu, F., *Clays Clay Miner.* **57**, 715-724 (2009).

44. Frias, D., Nousir, S., Barrio, I., Montes, M., Lopez, T., Centeno, M. A., Odriozola, J. A., *Mater. Charact.* **58**, 776-781 (2007).

45. Liu, L., Feng, Q., Yanagisawa, K., *J. Mater. Sci. Lett.* **19**, 2047 - 2050 (2000).

46. Drits, V. A., Lanson, B., Gaillot, A. C., *Am. Mineral.* **92**, 771-788 (2007).

47. Johnson, E. A., Post, J. E., *Am. Mineral.* **91**, 609-618 (2006).

48. Mackenzie, K. J. D., Smith, M. E., *Multinuclear Solid-State NMR of Inorganic Materials*. R. W. Cahn, Ed., Pergamon Materials Series (Elsevier Science Ltd., ed. 1st, 2002), vol. 6, pp. 727.

49. Potter, R. M., Rossman, G. R., *Am. Mineral.* **64**, 1199-1218 (1979).

50. Marezio, M., Plettinger, H. A., Zachariasen, W. H., *Acta Crystallogr.* **16**, 594-595 (1963).

51. Brown, I. D., Shannon, R. D., *Acta Crystallogr.* **A29**, 266-282 (1973).

52. Miletich, R., Pertlik, F., *J. Alloys Compd.* **268**, 107-111 (1998).

Chapter 4

1. Kuma, K., Usui, A., Paplawsky, W., Gedulin, B., Arrhenius, G., *Mineral Mag* **58**, 425-447 (1994).

2. Drits, V. A., Silvester, E., Gorshkov, A. I., Manceau, A., *Am. Mineral.* **82**, 946-961 (1997).

3. Post, J. E., Appleman, D. E., *Am. Mineral.* **73**, 1401-1404 (1988).

4. Giovanoli, R., Stahli, E., Feitknecht, W., *Helv. Chim. Acta* **53**, 209-220 (1970a).

5. Silvester, E., Manceau, A., Drits, V. A., *Am. Mineral.* **82**, 962-978 (1997).

6. Lanson, B., Drits, V. A., Silvester, E., Manceau, A., *Am. Mineral.* **85**, 826-838 (2000).

7. Lanson, B., Drits, V. A., Feng, Q., Manceau, A., *Am. Mineral.* **87**, 1662-1671 (2002).

8. Sherman, D. M., Peacock, C. L., *Geochem. Cosmochim. Ac.* **74**, 6721-6730 (2010).

9. Toner, B., Manceau, A., Webb, S. M., Sposito, G., *Geochim. Cosmochim. Acta* **70**, 27-43 (2006).

10. Lanson, B., Drits, V. A., Gaillot, A. C., Silvester, E., Plancon, A., Manceau, A., *Am. Mineral.* **87**, 1631-1645 (2002).

11. Mckenzie, R. M., *Geochim. Cosmochim. Acta* **43**, 1855-1857 (1979).

12. Drits, V. A., Lanson, B., Gaillot, A. C., *Am. Mineral.* **92**, 771-788 (2007).

13. Pecharsky, V. K., Zavalij, P. Y., *Fundamentals of Powder Diffraction and Structural Characterizatin of Materials*. (Springer, New York, 2005), pp. 713.

14. Webb, S. M., Tebo, B. M., Bargar, J. R., *Am. Mineral.* **90**, 1342-1357 (2005).

15. Webb, S. M., Tebo, B. M., Bargar, J. R., *Geomicrobiol. J.* **22**, 181-193 (2005).

16. Ressler, T., Brock, S. L., Wong, J., Suib, S. L., *J. Phys. Chem. B* **103**, 6407-6420 (1999).

17. Villalobos, M., Lanson, B., Manceau, A., Toner, B., Sposito, G., *Am. Mineral.* **91**, 489-502 (2007).

18. Liu, K., Ryan, D., Nakanishi, K., McDermott, A., *J. Am. Chem. Soc.* **117**, 6897-6906 (1995).

19. Feng, X. H., Zhai, L. M., Tan, W. F., Liu, F., He, J. Z., *Environ. Pollut.* **147**, 366-373 (2007).

20. Feng, X. H., Ginder-Vogel, M., Zhu, M. Q., Sparks, D., *Abstr Pap Am Chem S* **236**, 47-GEOC (2008).

21. Johnson, E. A., Post, J. E., *Am. Mineral.* **91**, 609-618 (2006).

22. Massiot, D., Fayon, F., Capron, M., King, I., Le Calve, S., Alonso, B., Durand, J. O., Bujoli, B., Gan, Z. H., Hoatson, G., *Magn. Reson. Chem.* **40**, 70-76 (2002).

23. Tian, H., He, J. H., Zhang, X. D., Zhou, L., Wang, D. H., *Microporous Mesoporous Mat.* **138**, 118-122 (2011).

24. Mckenzie, R. M., *Mineral Mag* **38**, 493-& (1971).

25. Rogers, D. B., Germann, R. W., Arnott, R. J., *J. Appl. Phys.* **36**, 2338-2343 (1965).

26. Frias, D., Nousir, S., Barrio, I., Montes, M., Lopez, T., Centeno, M. A., Odriozola, J. A., *Mater. Charact.* **58**, 776-781 (2007).

27. Paik, Y., Osegovic, J. P., Wang, F., Bowden, W., Grey, C. P., *J. Am. Chem. Soc.* **123**, 9367-9377 (2001).

28. Kim, J., Nielsen, U. G., Grey, C. P., *J. Am. Chem. Soc.* **130**, 1285-1295 (2008).

29. Hauch, A., Bildsoe, H., Jakobsen, H. J., Skibsted, J., *J. Magn. Reson.* **165**, 282-292 (2003).

30. Nielsen, U. G., Majzlan, J., Grey, C. P., *Chem. Mater.* **20**, 2234-2241 (2008).

31. Stepanov, A. G., Shegai, T. O., Luzgin, M. V., Essayem, N., Jobic, H., *J. Phys. Chem. B* **107**, 12438-12443 (2003).

32. Younger, P. L., Banwart, S. A., Hedin, R. S., *Mine Water: Hydrology, Pollution, Remediation (Environmental Pollution)*. (Kluwer Academic Publishers, Dordrecht, ed. 1st, 2002).

33. Isaacs, E. D., Shukla, A., Platzman, P. M., Hamann, D. R., Barbiellini, B., Tulk, C. A., *Phys. Rev. Lett.* **83**, 4445-4445 (1999).

34. Neuefeind, J., Benmore, C. J., Tomberli, B., Egelstaff, P. A., *J Phys-Condens Mat* **14**, L429-L433 (2002).

35. Feng, X. H., Liu, F., Tan, W. F., Liu, X. W., *Clays Clay Miner.* **52**, 240-250 (2004).

36. Feng, Q., Lui, L. , Yanagisawa, K. , *J. Mater. Sci. Lett.* **19**, 1567 - 1570 (2000).

Chapter 5

1. Aldi, K. A., Heeinmaa, I., Kim, J., Ilott, A., Zheng, D., Grey, C. P., (Submitted for Publication).

2. Villalobos, M., Toner, B., Bargar, J., Sposito, G., *Geochim. Cosmochim. Acta* **67**, 2649-2662 (2003).

3. Villalobos, M., Lanson, B., Manceau, A., Toner, B., Sposito, G., *Am. Mineral.* **91**, 489-502 (2006).

4. Drits, V. A., Lanson, B., Gorshkov, A. I., Manceau, A., *Am. Mineral.* **83**, 97-118 (1998).

5. Pecharsky, V. K., Zavalij, P. Y., *Fundamentals of Powder Diffraction and Structural Characterizatin of Materials*. (Springer, New York, 2005), pp. 713.

6. Drits, V. A., Lanson, B., Gaillot, A. C., *Am. Mineral.* **92**, 771-788 (2007).

7. Webb, S. M., Tebo, B. M., Bargar, J. R., *Am. Mineral.* **90**, 1342-1357 (2005).

8. Ressler, T., Brock, S. L., Wong, J., Suib, S. L., *J. Phys. Chem. B* **103**, 6407-6420 (1999).

9. Post, J. E., Veblen, D. R., *Am. Mineral.* **75**, 477-489 (1990).

10. Kuma, K., Usui, A., Paplawsky, W., Gedulin, B., Arrhenius, G., *Mineral Mag* **58**, 425-447 (1994).

11. Lanson, B., Drits, V. A., Silvester, E., Manceau, A., *Am. Mineral.* **85**, 826-838 (2000).

12. Webb, S. M., Tebo, B. M., Bargar, J. R., *Geomicrobiol. J.* **22**, 181-193 (2005).

13. Bruno Lanson, V. A. D., Qi Feng, Alain Manceau, *Am. Mineral.* **87**, 1662-1671 (2002).

14. Silvester, E., Manceau, A., Drits, V. A., *Am. Mineral.* **82**, 962-978 (1997).

15. Pena, J., Kwon, K. D., Refson, K., Bargar, J. R., Sposito, G., *Geochim. Cosmochim. Acta* **74**, 3076-3089 (2010).

16. Webb, S. M., *Phys. Scr.* **T115**, 1011-1014 (2005).

17. Newville, M., *J. Synchrot. Radiat.* **8**, 322-324 (2001).

18. Newville, M., *J. Synchrot. Radiat.* **8**, 96-100 (2001).

19. Ravel, B., *J. Synchrot. Radiat.* **8**, 314-316 (2001).

20. McKeown, D. A., Post, J. E., *Am. Mineral.* **86**, 701-713 (2001).

21. Kwon, K. D., Refson, K., Sposito, G., *Phys. Rev. Lett.* **100**, (2008).

22. Lopano, C. L., Heaney, P. J., Post, J. E., Hanson, J., Komarneni, S., *Geochim. Cosmochim. Acta* **68**, A86-A86 (2004).

23. Manceau, A., Lanson, B., Drits, V. A., *Geochim. Cosmochim. Acta* **66**, 2639-2663 (2002).

24. Aldi, K. A., Cabana, J., Sideris, P. J., Middlemiss, D. S., Grey, C. P., (Submitted for publication).

Chapter 6

1. Carlier, D., Cheng, J. H., Berthelot, R., Guignard, M., Yoncheva, M., Stoyanova, R., Hwang, B. J., Delmas, C., *Dalton T* **40**, 9306-9312 (2011).

2. Athouel, L., Moser, F., Dugas, R., Crosnier, O., Belanger, D., Brousse, T., *J. Phys. Chem. C* **112**, 7270-7277 (2008).

3. Kim, J., Middlemiss, D. S., Chernova, N. A., Zhu, B. Y. X., Masquelier, C., Grey, C. P., *J. Am. Chem. Soc.* **132**, 16825-16840 (2010).

4. Kim, J., Nielsen, U. G., Grey, C. P., *J. Am. Chem. Soc.* **130**, 1285-1295 (2008).

5. Li, W., Feng, J., Kwon, K. D., Kubicki, J. D., Phillips, B. L., *Langmuir* **26**, 4753-4761 (2010).

6. Webb, S. M., Tebo, B. M., Bargar, J. R., *Am. Mineral.* **90**, 1342-1357 (2005).

7. Ressler, T., Brock, S. L., Wong, J., Suib, S. L., *J. Phys. Chem. B* **103**, 6407-6420 (1999).

8. Drits, V. A., Lanson, B., Gaillot, A. C., *Am. Mineral.* **92**, 771-788 (2007).

9. Lanson, B., Drits, V. A., Silvester, E., Manceau, A., *Am. Mineral.* **85**, 826-838 (2000).